Regional Seismic Wavefield Propagation

Thesis by

Brian Savage

In Partial Fulfillment of the Requirements
for the Degree of
Doctor of Philosophy

California Institute of Technology
Pasadena, California

2004
(Defended May 26, 2004)

Acknowledgements

My stay at the Seismo Lab at Caltech has been long, strange trip. I came to Caltech expecting to work entirely on seismology, but it turns out I learned life is not just wiggles. I do not think my knowledge would have been expanded as much at another institution. For that I am deeply thankful for the structure and friendliness of the Seismo Lab. I would also especially like to thank my thesis committee. Even though the committee was formed late, each member has contributed and been supportive along the way.

I would like to thank my immediate family of Sandy, Jack, Eric and Vivian. They have always been behind me cheering me on and making fun of me while not understanding what I do. Without you I would not be in the position I am in. I want to thank my grandparents. I know you have always been there and always will be. Last but not least, I would like to thank Jim. I feel somehow you played a role through inspiration and stories about mid-ocean ridges, landslides, and slumps.

I would like to thank my research advisor, Don Helmberger. While we may not be rich and famous for looking at seismogams, at least it was fun. I will miss the days staring out the window and trying to understand complex wave propagation. You always gave me inspiration and youthful exuberance. How come you are always right?

I would like to thank my good friends from Berkeley. Karen, Sterling, Jeremy, Adam, Sheetal, Heather and Jen. Everyone of you is important and played a role in writing this thesis. I would especially like to thank Karen for always being there to hear me complain or share in my joy, thanks big sis. I would also like to thank my friends from Modesto. Kyle, Alan and Matt. I love getting together with you guys and doing nothing. You will always be brothers to me.

I would like to thank my office mates for putting up with my random working style. Zhimei, Nathan, Javier, Rowena, Martin, Leo, and Qinya. Each and everyone of you taught me something. And I think each and everyone of you has laughed at me for my dancing in

the office.

I would like to thank my roommates, Javier, Alisa and Sterling. You let me live as I pleased and for that I am grateful. I became better friends with each of you from living with you.

There are a number of friends I would like to thank from the Pasadena area. Heather for providing a needed outlet, a diversion from Caltech, and letting me be me. Jascha and Hong-Kie for being good friends and always up for a great meal not matter what country. Leo, Martin, and Javier for always being up for a beer or three. Vala and Oliver for skiing and treating me like one of the family. Vala further for church and keeping me grounded. You have always been there and for that I am blessed to have you as a friend. Alisa and Chris for dinner plans and silliness. You were both there when I needed it. And a whole gaggle of other people: Lupei, Qinya, Zhimei, Ying, Ozgun, Magali, Sidao, and Chen.

From my original Seismo Lab at Cal, I would like to thank Doug. Without you I would not have gotten interested in seismology or would not have started "staring" at seismograms. I had fun with the historic data and made many friends with the rats of Edwards. I think Caltech was the right choice. Thank you.

From the Caltech Seismo Lab. Mark for helping my through InSAR, glacial flow modeling, and so much more. Jeroen for allowing the stupid questions and letting me run on his big computer. Rob for helping me out with finite difference. Joann for sending me to one end of the earth. I had a blast and would love to do it again. Mike for being an involved academic advisor and asking me the important questions. Finally, Hiroo for always being an inspiration and being the staple that is coffee.

I would like to thank all the Seismo Lab staff, especially Evelina. Without you I know I would have been lost. You always made me smile. Salamat po.

I would also like to thank those who played on the Lovewaves, Earthquakes, and Wumprats. I had fun playing and managing. Everyone of you was great and such a pleasure to be around.

Finally, I would like to thank Les Claypool and Pete Savage.

Abstract

Through the examination of local and regional seismic waveform data the crust and upper mantle of southern California are investigated. Using local and regional seismic phases such as Pn, Sn, PL, and surface waves, seismic wave velocities of interesting tectonic structures are determined. These structures include the southern Sierra Nevada, San Bernardino Mountains, and the Salton Trough / Imperial Valley. Detailed studies of how seismic waves propagate at local and regional distances are also undertaken. Knowledge of the seismic wave propagation through these tectonic provinces provides for a robust determination of their characteristics. Further, complex source and site-related propagation are included through an investigation of the Kursk submarine explosion and basin-related site amplification.

Contents

List of Figures

List of Tables

Introduction

> Once upon a time there was a young man walking through a forest of many similar looking trees. During his walk he happened upon a pot of gold, which of course belonged to a leprechaun. He decided to take the gold for his own, but found the gold was too heavy for him to carry all by himself. So he decided to go home and get a cart to help collect his bounty. Since all the trees in the forest looked very similar he decided to tie a yellow ribbon around a tree near the gold so he would know where to find it. At this time, the little leprechaun came walking by and noticed what the young man was doing. The leprechaun not so politely inquired what the young man thought he was doing. The young man told the leprechaun that the gold had better be there when he returned or the leprechaun was going to be swimming with the fishes. Upon returning to the forest after fetching the cart from his abode, the young man noticed all the trees in the forest were wrapped in yellow ribbons.[1]

Regional waveforms tend to look very similar, especially at longer periods, much like trees in a forest. Attempts to incorporate higher frequencies will allow discrimination of different tectonic provinces. It is the coherent, but slight differences from province to province that will enable a model or map to be constructed. It is this model which will guide in future tectonic, seismological and geodynamical studies, the leprechaun's pot of gold.

Traditionally, seismologists examine individual waveforms or when using a large dataset reduce the waveforms to particular parameters, e.g., arrival times or phase velocities. In the past, due to the limited deployment of broadband instrumentation, examination of individual waveforms was practical. Further, many large data sets require reduction because

---

[1] Don Helmberger has told this story to me numerous times so I feel compelled to include it.

the majority of the recorded time signal are unusable due to the type of instrumentation, i.e., short-period seismographs.

Upon my arrival at Caltech, data from the TriNet seismic network had just become available. This network of over 140 stations is one of the first large-scale, regional broadband networks in the world. The network was designed from the groundfloor to deliver high-quality broadband data to researchers from a tectonically active and complex region. Already vasts amounts of data provided by this network has helped in hazard mitigation, early warning, and detection/location of earthquakes. In addition to gaining information on the seismic behavior of southern California, the network had already fostered new research directions in earth science.

All of the following chapters, except for one, use data from the TriNet broadband network. While the techniques presented here are rudimentary and do not use "sophisticated" algorithms or inversion techniques, they do capture specific wavefield propagation phenomena important to understanding regional recordings (Pn, Sn, and high frequency surface waves $<$ 20 seconds period). While the following chapters may seems unrelated due to the geographic separation, a consistent theme runs through them all: Wavefield Propagation.

Chapter 1, Southern Sierra Nevada. A look into the crust and upper mantle velocity structure beneath the Southern Sierra Nevada and Walker Lane. We investigate and explain an anomalous arrival as a reflection of a refracted arrival due to a discontinuity in the mantle at 75 to 100 km depth [*Savage et al.*, 2003].

Chapter 2, San Bernardino Mountains. Examination of the crust and mantle underneath the San Bernardino Mountains. Refracted arrivals traversing the mountains show a pronounced delay and advance with distance, in addition to slight changes in frequency. We determine a thickness and shape of the crustal root of from these data.

Chapter 3, Pn Amplification. A theoretical explanation of the amplification of seismic arrivals at a site. Further, we quantify the effect of slow velocities on amplification and provide a simple means of calibrating soft-sediment sites against those of hard-rock [*Savage and Helmberger*, 2004a].

Chapter 4, Complex Rayleigh Wave. Using abnormal observations from a pair of earthquakes which occurred in a substantial basin, we explain the overarching features of the basin and the propagation which created the observations [*Savage and Herlmberger*, 2004b].

Chapter 5, Kursk Explosion. Utilizing data of up to 1000 km away from the Kursk submarine explosion, we explain the details of the recorded waveforms and determine the size of the explosion [*Savage and Helmberger*, 2001].

Chapter 1

Velocity Variations in the Uppermost Mantle Beneath the Southern Sierra Nevada and Walker Lane

1.1 Introduction

The Basin and Range province in western North America is bounded on the west by north-south trending deep valleys and mountain ranges consisting of California's Central Valley, the Sierra Nevada, and Walker Lane (Figure 1.1). Walker Lane includes Death Valley and Owens Valley, and trends parallel to the Sierra Nevada from the Garlock fault in the south to central Oregon. The Sierra Nevada transitions from sloping foothills in the west to over 4 km of abrupt relief in the east.

This dramatic topography in the Sierra Nevada and Walker Lane is a result of the complex tectonic evolution during the Cenozoic (65 Ma to present) [*Bateman and Eaton*, 1967; *Dumitru et al.*, 1991; *Wernicke*, 1992; *Burchfiel et al.*, 1992a, b]. *Wernicke and Snow* [1998] use geologic reconstructions to suggest that prior to 8 Ma, the Sierra Nevada and California's Central Valley were moving west at >20 mm/yr relative to the Colorado Plateau. Kinematic models [*Wernicke and Snow*, 1998; *Snow and Wernicke*, 2000] suggest that from 8 Ma to present the Sierra Nevada began moving at 15 mm/yr to the northwest to north-northwest. At the same time, (∼20 Ma) Sierra Nevada uplift began and the slab window due to the passing Farallon Plate formed [*Atwater and Stock*, 1998]. The mechanism of Sierra Nevada uplift is still under debate and the kinematics of the surrounding region

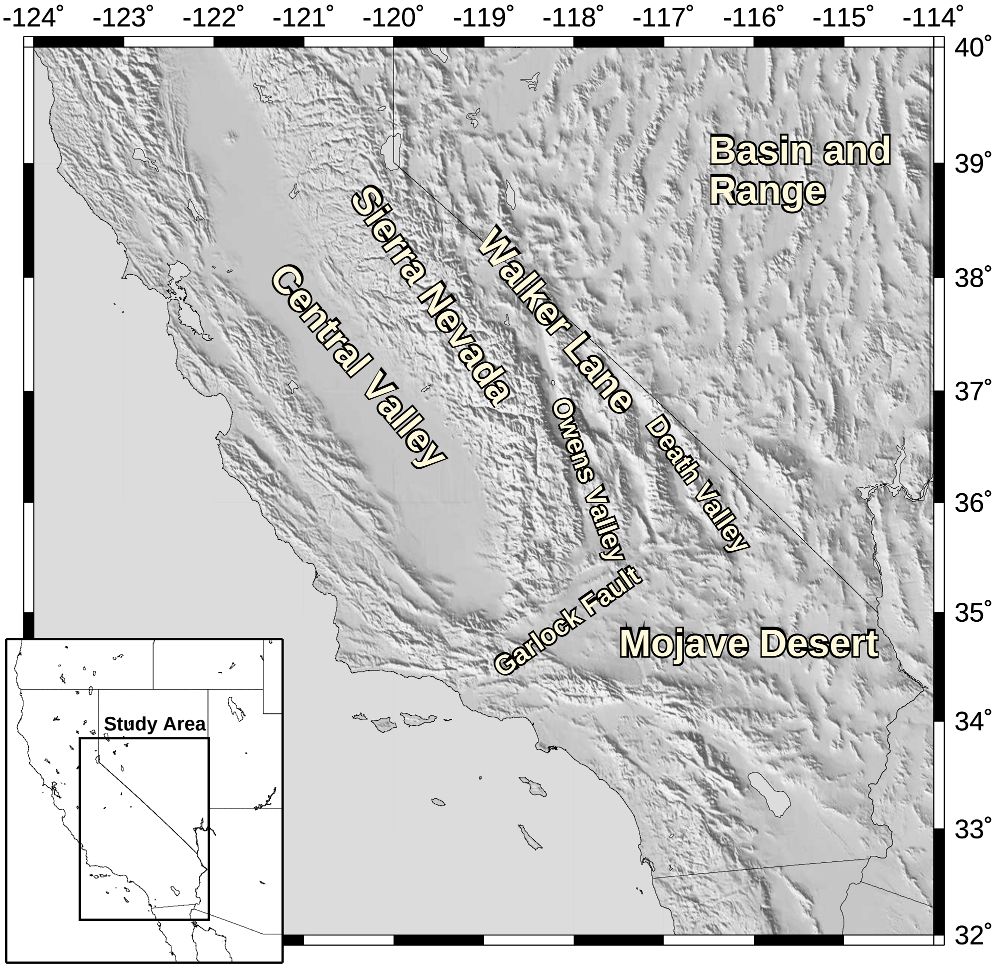

Figure 1.1: Map of California and Nevada within western North America showing relevant provinces and their locale relative to one another. A complex, yet poorly understood, series of tectonic events occurred to produce the topography across the region. The area within the Sierra Nevada and Walker Lane south of 38deg N is the focus of this study.

are still poorly understood.

Geophysical and geochemical studies provide important data which constrains the structural properties of the Sierra Nevada and allows us to assess models of their uplift. Reduced heat flow in the Sierra Nevada [*Saltus and Lachenbruch*, 1991] suggest a lateral increase in heat flux at the base of the crust and large thermal gradients in the lithosphere beneath the eastern slope of the Sierra Nevada towards the Basin and Range. Geochemical data from *Ducea and Saleeby* [1996, 1998a, b, c] show a corresponding rapid structural change in the lithosphere and upper mantle. Examination of xenoliths [*Ducea and Saleeby*, 1998c] shows that prior to 6 Ma, the Sierra Nevada was underlain by an ultra-mafic, eclogitic root or mantle lithosphere. At ∼6 Ma the deep (∼75 km), eclogitic lithosphere is replaced by hot asthenosphere. Gravity modeling by *Fliedner and Ruppert* [1996] suggests lateral density variations in the upper mantle. This agrees with heat flow and xenolith data which implies that a hotter, less dense, asthenospheric mantle on the eastern edge of the Sierra Nevada extends into the Basin and Range.

Dynamic models of western North American which include subduction, uplift of the Sierra Nevada, and extension of the Basin and Range do not exist at present. However, smaller-scale investigations of the relative effects of plate-boundary forces, lithosphere basal forces, and buoyancy forces (see Table 1 of *Sonder and Jones* [1999] and *Chase and Wallace* [1988], *Zandt and Carrigan* [1993], and *Liu and Zandt* [1996]) may guide broader scale studies in the future. In this study we do not attempt to discern which forces are dominant in the system, but aim to place constraints on the structural properties of the upper mantle and lower crust with high quality seismic waveform data.

1.2 Geophysical Observations

While an investigation of the entire Sierra Nevada range and Walker Lane from north to south would be desirable, the lack of available waveform data in the north limits our study area to the southern region. However, teleseismic P, S, and ScS waves [*Ding and Helmberger*, 1997; *Melbourne and Helmberger*, 2001] from earthquakes in South America propagate faster when they travel through the Sierra Nevada north of 38°N than those that propagate through the southern Sierra Nevada, indicating a contrast from north to south.

Lawson [1936] and *Byerly* [1937], using a small set of gravity data and seismic travel times, suggest that the Sierra Nevada is in isostatic equilibrium with a thick crustal root. Deployment of seismic refraction lines parallel and perpendicular to the Sierra Nevada axis have been used to estimate the vertical extent of the crustal root. Figure 1.2 shows the location of different active source refraction experiments in and around the Sierra Nevada.

Each refraction experiment reports delayed Pn arrivals along paths crossing the Sierra Nevada mountains which were interpreted as either a thick crustal root or a low velocity mantle. However, the reported velocity structure is dependent on orientation of the refraction profile across the Sierra Nevada.

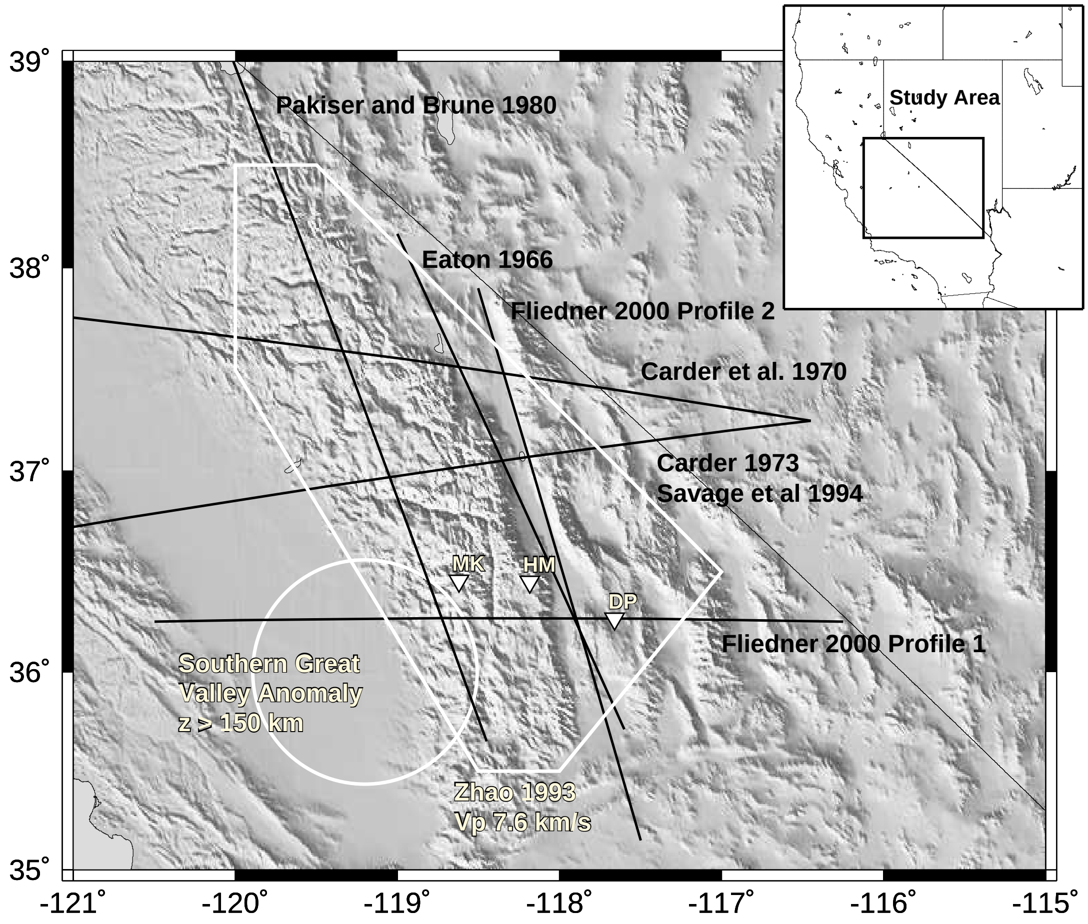

Figure 1.2: Regional map of the southern Sierra Nevada and Walker Lane showing previous passive and active experiments. All black lines and labels refer to active source studies with the lines representing the refraction profiles. Each line-label pair is unique except for *Carder* [1973] and *Savage et al.* [1994], which share the same profile. White features show passive experiments. The southern Great Valley Anomaly (circle) [*Biasi and Humphreys*, 1992] is a region of high velocity at a depth of approximately 150 km. The inverted triangles [*Jones and Phinney*, 1998] are temporary seismic stations used to compute receiver functions, and the large white area which encloses the entire southern Sierra Nevada is a region of 7.6 km/s Pn velocity from the tomography of *Zhao* [1993].

Refraction lines parallel to the Sierra Nevada [*Eaton*, 1966; *Pakiser and Brune*, 1980] relate the delayed Pn travel times to a crustal root, in agreement with previous gravity studies [*Lawson*, 1936]. Models invoking crustal roots exceeding 50 km and velocities in the lower crust of 6.9 km/s explain the travel times of both studies [*Eaton*, 1966; *Pakiser and Brune*, 1980]. Rayleigh wave phase velocities measured by *Crough and Thompson* [1977] along a similar profile show a low velocity mantle beneath a thick Sierra Nevada crust and the Basin and Range. Their results are also based upon previous work by *Eaton* [1966]. In contrast, perpendicular profiles [*Carder et al.*, 1970; *Carder*, 1973; *Savage et al.*, 1994] interpret the late Pn travel times as a result of a low V_p mantle and a crustal thickness of ∼35km thickness. *Savage et al.* [1994] suggest a V_p anomaly of 7.2 km/s in the west to 7.7 km/s in the east.

Recent seismic reflections and refractions both parallel and perpendicular to the Sierra Nevada, in conjunction with gravity modeling, receiver functions, and teleseismic arrival times [*Wernicke et al.*, 1996; *Jones et al.*, 1994; *Jones and Phinney*, 1998; *Fliedner et al.*, 2000] argue against the existence of a thick crustal root. In particular, *Jones and Phinney* [1998] use a suite of receiver functions to identify a low velocity zone within the crust and the presence of a low velocity mantle below the Sierra Nevada, shown as inverted triangles in Figure 1.2. Upper mantle tomographic studies of the area [*York and Helmberger*, 1973; *Biasi and Humphreys*, 1992; *Zhao*, 1993; *Pollitz*, 1999] also support a lower velocity mantle beneath much of the southern Sierra Nevada and Walker Lane (white outline in Figure 1.2). To complement recent studies in tomography, gravity, and receiver functions the advent of dense, large-scale broadband seismic arrays provides travel times and waveform data particularly suited to image the crust and upper mantle.

1.3 Data

We use two types of data to illuminate the crust/mantle interface beneath the southern Sierra Nevada and Walker Lane. First, using a small set of travel time data from an event in Northern California, we infer a dramatic velocity structure within the study region. Second, we model waveform data from earthquakes in Mammoth Lakes and near the California-Nevada border to constrain the velocity structure of the crust/mantle interface within the study area.

Both data sets feature Pn arrivals, including pPn and sPn. To illustrate how the Pn arrivals sample the crust-mantle interface, synthetics for a simple model of a layer over a half-space are shown in Figure 1.3. Pn is a refracted phase which propagates in the mantle just below the crust. The shaded region in Figure 1.3 indicates the sampling region of Pn. Generally, the greater the epicentral distance, the greater the penetration of Pn below the

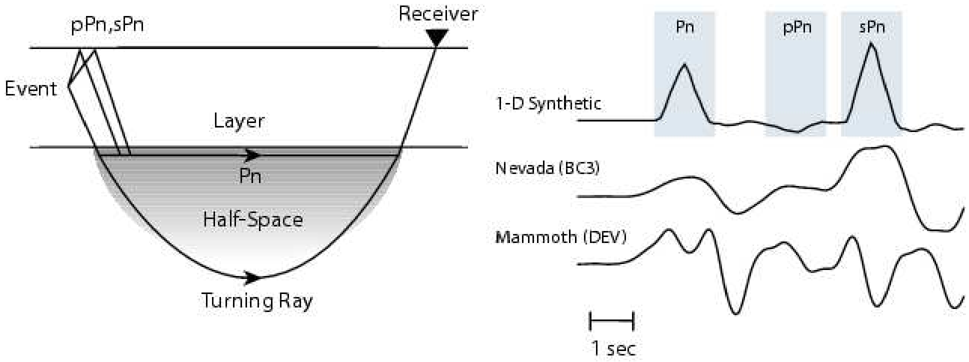

Figure 1.3: Left panel indicates the raypaths for Pn, pPn for a model of a layer over a half-space (simplification of the crust over the mantle), and sPn. Pn is normally thought of as an arrival whose path is directly along the interface between the layer and half-space. However, the energy which creates the Pn arrival is distributed across a large depth range within the half-space, as indicated by the gray shading. Eventually, at large epicentral distance, Pn merges with the turning ray in a half-space. The right panel, top, shows vertical velocity waveforms including Pn, pPn, and sPn for the layer over a half-space velocity model on the left (450 km). Notice how the typical data (BC3) is similar to to the simple model at the top, in contrast to the complicated, abnormal waveform (DEV).

Moho. The depth phases, pPn and sPn, arrive later than Pn as they first travel to the surface as either up-going P or S waves before traversing the same path as Pn below the Moho. The relative arrival time of Pn, pPn, and sPn is controlled by the depth of the event. The wave shape of Pn, as in Figure 1.3, is an integration of the far-field ground motion, $S(t)$. If we assume the shape of $S(t)$ is a triangle in displacement, then Pn signals are shaped like ramps:

$$P_n(t)_{Displacement} \cong \int S(t)dt \tag{1.1}$$

After differentiating, the ramp in displacement changes into a triangular function in velocity.

$$P_n(t)_{Velocity} \cong \frac{d}{dt}\int S(t)dt = S(t) \tag{1.2}$$

In contrast, ground motion velocities from post-critical reflections such as PmP (not shown) will appear “double-sided”, that is, has a positive triangular pulse followed by a negative one. Also included in Figure 1.3 is the portion of the synthetics used for comparison with the data. Comparing the simple 1-D model and the “typical” waveform shows both are comprised of simple, triangular shaped Pn and sPn arrivals. The “atypical” trace is complex because the existence of a second pulse followed is by a large downswing occurring near the Pn arrival.

1.4 Data - Travel Times

We show Pn travel time data from an earthquake in Santa Rosa, northern California in Figure 1.4a, while selected waveform data from the same earthquake are displayed in Figure 1.4b with a 8.0 km/s reduction velocity. Both data types highlight interesting features around the Sierra Nevada. In Figure 1.4a blue to white stations record relatively short Pn travel times corresponding to a Pn velocity of ∼7.8 - 8.0 km/s, while white to red stations record larger delays and slower Pn velocities (∼7.6 - 7.8 km/s). Pn waves that travel parallel to the San Andreas Fault and do not traverse the Sierra Nevada or Walker Lane regions have similar, short travel times, as shown by the cluster of blue circles near Los Angeles. Pn recorded in the Sierra Nevada and Walker Lane, have longer travel times (white to red circles) with a maximum at station MLAC (Mammoth Lakes, California). Great circle paths for these slower arrivals are shown in Figure 1.4a as solid lines. About 1 second of the delay at MLAC is probably the result of a large magma chamber beneath the area [*Bailey et al.*, 1976; *Weiland et al.*, 1995]. Stations further to the southeast also indicate late first arrivals.

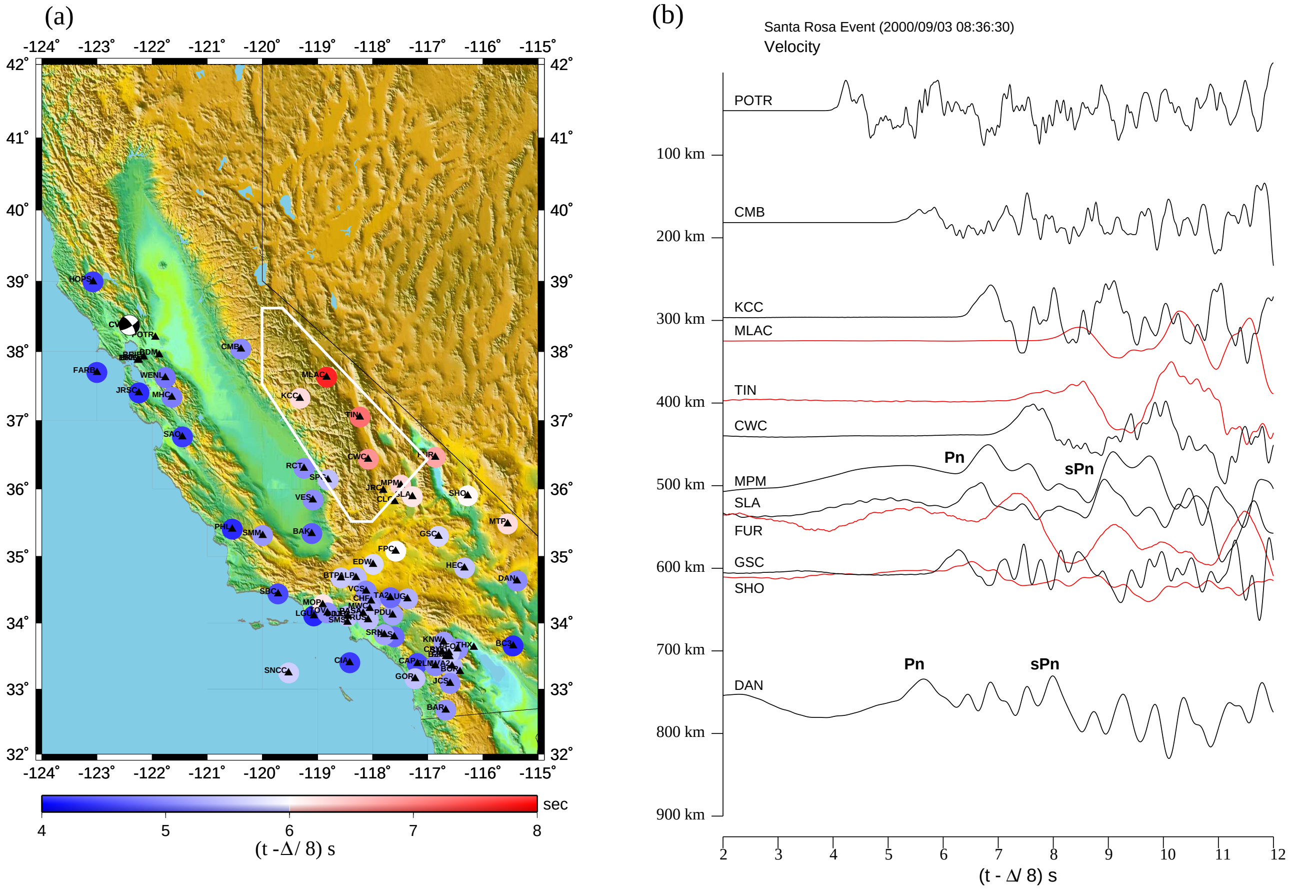

Figure 1.4: a) Pn arrival times with the color indicating the delay with respect to an arrival of 8.0 km/s. The earthquake, location indicated by the source mechanism, is located in Santa Rosa in northern California. Ray paths are shown for selected stations and part b) shows the corresponding waveforms. b) Vertical velocity data from the same earthquake as in a). Notice the clustering of late Pn times, white to red, for paths which cross the Sierra Nevada. Stations further to the east show a much more pronounced slowing compared with those to the west. Those stations to the northeast, marked in red, are also longer period than those just slightly to the southwest, black. The white outline was determined by [*Zhao*, 1993] to be slower than average mantle, 7.6km/s, using regional Pn travel-times.

The seismic waveform data (Figure 1.4b) with station labels show Pn recorded to the north (red waveforms) arrive later and have longer period waveforms than the impulsive, earlier arrivals recorded to the south (black waveforms). The waveform data and travel time differences suggests complex structure within the Southern Sierra Nevada and Walker Lane. This data supports a very sharp transition from KCC to MLAC (apparent mantle V_p less than 6 km/sec) and then a gradual increase in velocity, up to 8.0 km/s, towards the southeast. We did not attempt to explain these data in detail as it would require 3-D modeling as the raypaths sample distinctly different regions. Similar data were collected for two other events in northern California and their data is presented in Appendix A.

1.5 Data - Waveforms

Pn waveforms from two mid-1999 earthquakes that occurred in Mammoth Lakes and Western Nevada (Figure 1.5) provide extensive coverage that can help map out the crust-mantle interface beneath the southern Sierra Nevada and Walker Lane. These waveforms data were recorded by broadband instruments of TriNet. Instrument responses were deconvolved from the data to obtain ground motion velocity. The data is low-pass filtered at 1.5 Hz and plotted as a velocity time series, except where noted. Since we are modeling Pn and depth phases of Pn, which only arrive on the vertical and radial components, and the vertical component of Pn is nearly identical to the radial component of Pn, we only consider the vertical component of the data.

Tables 1.1 and 1.2 contain several estimates of source parameters for each earthquake. For each event, multiple methods for determining source parameters were used and provide consistent results. We use the Time Domain Moment Tensor [*Pasyanos et al.*, 1996] solution for the earthquake in Mammoth Lakes and our independently determined solution for the earthquake near the California-Nevada border. The range of faulting parameters given for our independently determined solution represents a set of parameters in which no appreciable change is seen between the waveform data and synthetics. Source time functions are determined from the widths of direct P waves at short distances for each event. Triangles with a half-width of 1 sec are convolved with the point source synthetics to facilitate comparison with data.

After defining the source parameters for both earthquakes, we group similar waveform

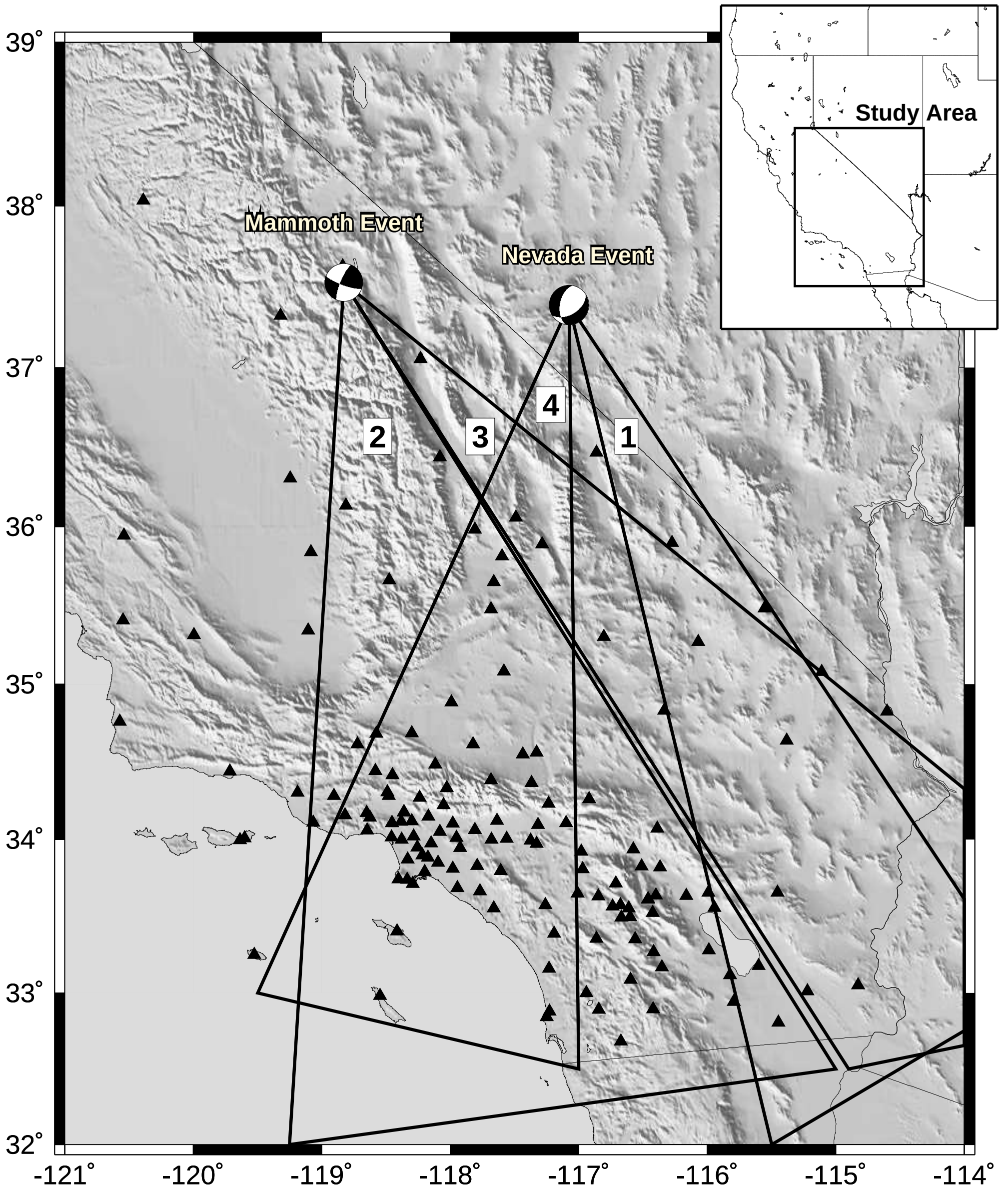

Figure 1.5: Map of California and Nevada, showing TriNet and Berkeley Digital Seismic Network (BDSN) stations as triangles, the source mechanisms used for this study, and the triangular swaths modeled using Pn waveforms. Studied triangular swaths are marked 1 through 4. Swaths 1 and 2 are used in waveform modeling, while swaths 3 and 4 are used only in model validation.

data into swaths, numbered 1-4 in Figure 1.5. We define "similar data" as data without dramatic changes in relative amplitude and without polarity reversals within the swath. Swaths 1 and 2 provide the primary waveform data used in deriving the velocity model. Swaths 3 and 4 will only provide confirmation of the model as both intersect a nodal plane,

Table 1.1: Mammoth, CA (37.5298, -118.8172) 15/05/1999(135) 13:22:19.066

Moment [dyne-cm]	Depth [km]	Strike [deg]	Dip [deg]	Rake [deg]	Source
4.30e24 (5.7Mw)	8	203/110	79/77	13/169	SWPA$^{\alpha}$
2.31e24 (5.5Mw)	8	203/294	85/80	-11/-174	TDMT $^{\beta}$

$^{\alpha}$ Surface Wave Phase Analysis, U.C. Berkeley
$^{\beta}$ Time Domain Moment Tensor, U.C. Berkeley

Table 1.2: CA-NV Border (37.3887, -117.0768) 01/08/1999(213) 16:06:22.005

Moment [dyne-cm]	Depth [km]	Strike [deg]	Dip [deg]	Rake [deg]	Source
7.00e24 (5.9Mw)	8	216/39	45/45	-92/-88	SWPA$^{\alpha}$
3.60e24 (5.7Mw)	8	226/39	64/26	-87/-96	TDMT$^{\beta}$
1.82e24 (5.44Mw)	8	194/71	64/42	-124/-41	GS$^{\gamma}$
3.60e24 (5.7Mw)	8	190	52 to 45	-120 to -125	This study$^{\delta}$

$^{\alpha}$ Surface Wave Phase Analysis, U.C. Berkeley
$^{\beta}$ Time Domain Moment Tensor, U.C. Berkeley
$^{\gamma}$ Grid Search, Caltech
$^{\delta}$ Fault parameters represent a range of values

making their source parameter estimates unstable and modeling results less meaningful. Representative vertical velocity waveforms from swaths 1 and 2 are plotted in Figure 1.3b and compared to a synthetic from a 1-D model. Recordings from swath 1, labeled "typical" in Figure 1.3b, with corresponding path along the eastern edge of Death Valley, are similar to the 1-D waveforms and will be discussed first. Recordings from swath 2, "atypical" in Figure 1.3b, which traverse the Southern Sierra Nevada are complex and will be discussed later.

1.5.1 Swath 1

Displacement and velocity waveform data for swath 1 from the earthquake near the California-Nevada border are plotted in Figure 1.6. In the displacement data, two clear arrivals are present, Pn and sPn. On some records pPn arrives between Pn and sPn, but is much smaller in amplitude. A strong reflected arrival off the Moho, PmP, is also present and its onset is indicated by a line. All Pn phases travel along and beneath the Moho and appear step-like in displacement (upper profiles of Figure 1.6). The radial component Pn, not shown, has a similar waveshape indicating that the velocity structure near the receiver is simple. It is difficult to describe the full range of models which can explain the data due to the non-uniqueness of waveform modeling. However, specific features of the waveforms, such as Pn width and PmP arrival times, are sensitive to small perturbations in the velocity model and can be used to highlight which portions of the velocity model are believable.

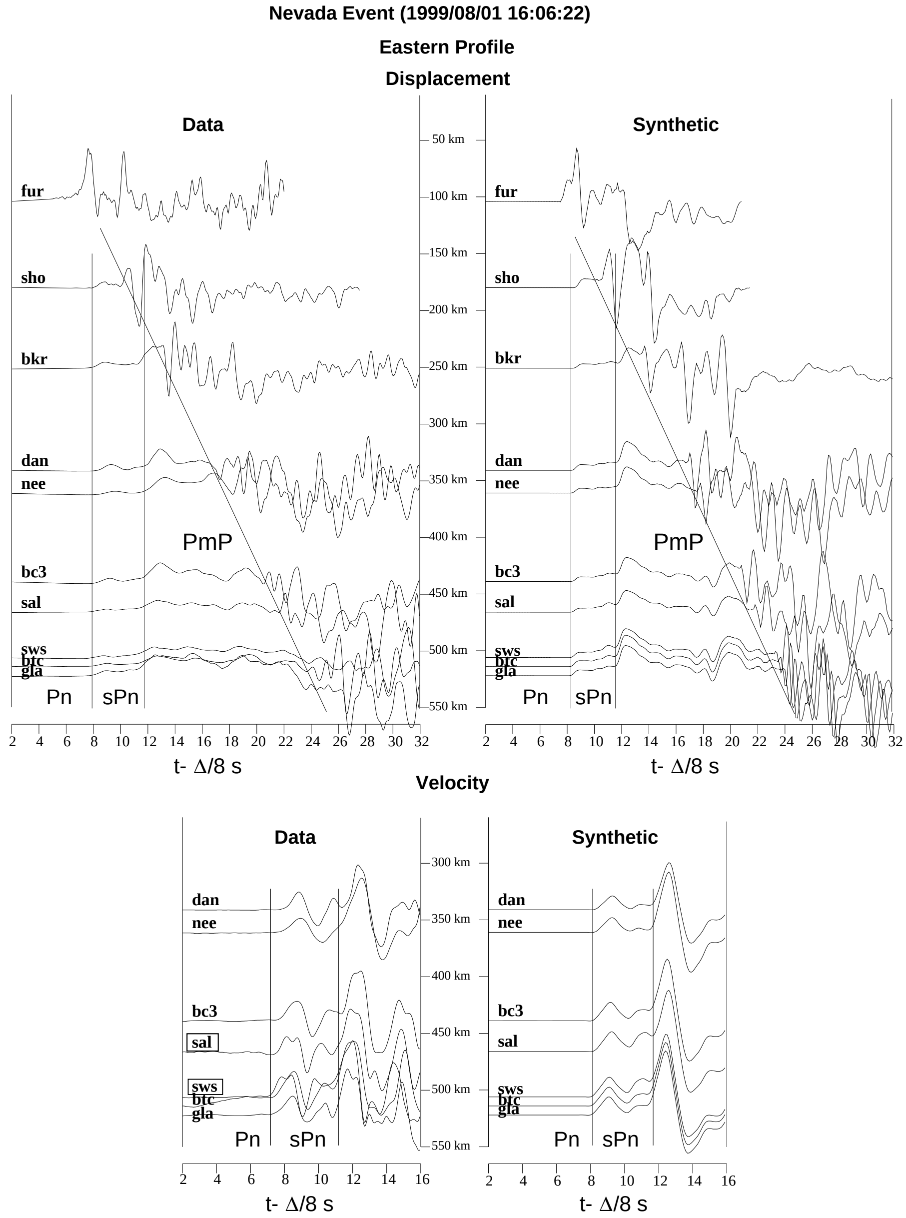

Figure 1.6: Comparison between data (displacement and velocity) and associated synthetics for swath 1 in Figure 1.5. Arrivals Pn and sPn are highlighted in gray boxes and the approximate arrival time for PmP is indicated by a line. The velocity model which produced the synthetics is displayed in Table 1.3. A vast majority of the data is explained by this simple flat-layered model.

We model these data in a forward sense with a simple layered model, Eastern Mojave (Table 1.3). This model is derived from the Mojave model [*Jones and Helmberger*, 1998]. Synthetic waveforms, shown to the right of the data, are computed by frequency-wavenumber (FK) integration [*Saikia*, 1994] convolved with a triangle source (half-width of 1 sec). The velocity and thicknesses of the top layers were changed to achieve a better fit to the timing and amplitude of Pn and PmP at less than 200 km distance. Similar to the Mojave model, the mid-crust of the Eastern Mojave model is a single velocity layer. The data in Figure 1.6 do not show arrivals resulting from a reflector in the mid-crust so a Conrad or mid-crustal discontinuity is not included in the 1-D model. The velocity transition from the lower crust to the mantle is gradual in the Eastern Mojave model. A sharp transition from the lower crust to the mantle would producean impulsive Pn, which is not desired. A smooth lower crust to mantle transition renders the Pn to be dispersed so that its waveforms are relatively broad, desirable for both Pn and PmP. A velocity gradient structure in the mantle similar to the tectonic North America (TNA) model [*Grand and Helmberger*, 1984], had no effect on the waveforms and can therefore be constrained. The travel times of Pn and sPn increase linearly with distance, implying that we do not need to invoke complex velocity structure, such as discontinuities.

Table 1.3: Eastern Mojave Velocity Model

Thickness [km]	V_p [km/s]	V_s [km/s]	Density [kg/m^3]
4	5.0	2.9	2400
19	6.1	3.5	2800
5	6.8	3.8	2800
2	7.0	4.0	2900
2	7.5	4.2	3000
half-space	8.05	4.42	3200

Next, we compare velocity data with synthetics to demonstrate that the velocity model does not explain higher frequency signals in Pn and sPn. A much larger time window for the displacement waveforms is used which includes the impulsive arrival PmP. The smaller time window for the velocity data only shows Pn and sPn, and not PmP. Velocity data allows us to resolve fine scale structure, < 5 km vertically, whereas displacement data resolves only larger scale features. The velocity waveforms show more complexity than found in the synthetics. The Pn waveform is either wider or is comprised of two arrivals at stations SAL and BC3, while larger than expected arrivals between Pn and sPn are recorded at stations DAN, SWS, and BTC. Pn arrivals recorded at these stations might be near the boundary between a simple 1-D type structure and a 2-D velocity structure to the west.

1.5.2 Swath 2

A record section of vertical velocity waveforms from the Mammoth Lakes earthquake, for a swath that traverses the southern Sierra Nevada, is shown in Figure 1.7 (swath 2 in Figure 1.5). The radial (not shown) and vertical components are similar in appearance, indicating that the velocity structure near the receiver is simple. The consistency of the Pn waveshape across the entire swath also suggests a simple crustal velocity structure near the receivers. Pn propagating through the southern Sierra Nevada upper mantle include an anomalous arrival, which we label as Pn′, that follows the initial Pn. Pn is the first positive pulse while Pn′ is a combination of the next positive and negative pulse. We assign the arrival a name Pn′ as it arrives coincident with Pn and is also derived from the Pn wavefield, discussed later. Pn′ arrives 0.75 - 1.0 seconds after Pn but with a similar slowness so that it propagates a similar path. We examine models of crustal and mantle roots that have been proposed by previous investigators in an attempt to explain the origin of Pn′.

In the next two sections, we will focus on the Pn waveforms and only show PmP at smaller distances. By analyzing only the Pn arrivals we constrain only the crust-mantle interface and the mantle below. We use a simple layered model for the mid to upper crust which is unconstrained by the Pn waveforms. Synthetics are computed using a 2-D finite difference technique from *Helmberger and Vidale* [1988] with a source depth of 8 km and a triangular half width of 1 second. As with swath 1, we use a forward modeling approach to explain the data. We cannot adequately assess the full family of models which might describe the data, but by addressing features in the data which are reproducible through synthetics we can specify which parts of the model the data is sensitive to. The technique used here is not sensitive to fine scale (< 10 km) structure because the sources we use are earthquakes with source lengths close to 1 sec. A comparison of synthetics from the next two sections is included later to highlight the major differences between a thick crustal root and a slow velocity mantle.

1.5.2.1 a) Crustal Root

In this section we analyze how a crustal root affects Pn as they travel along the Sierra Nevada. We use three models with crustal thicknesses that vary from 40, 50, and 60 km, according to the north-south profile in *Pakiser and Brune* [1980] (Figure 1.8 a, b, and c).

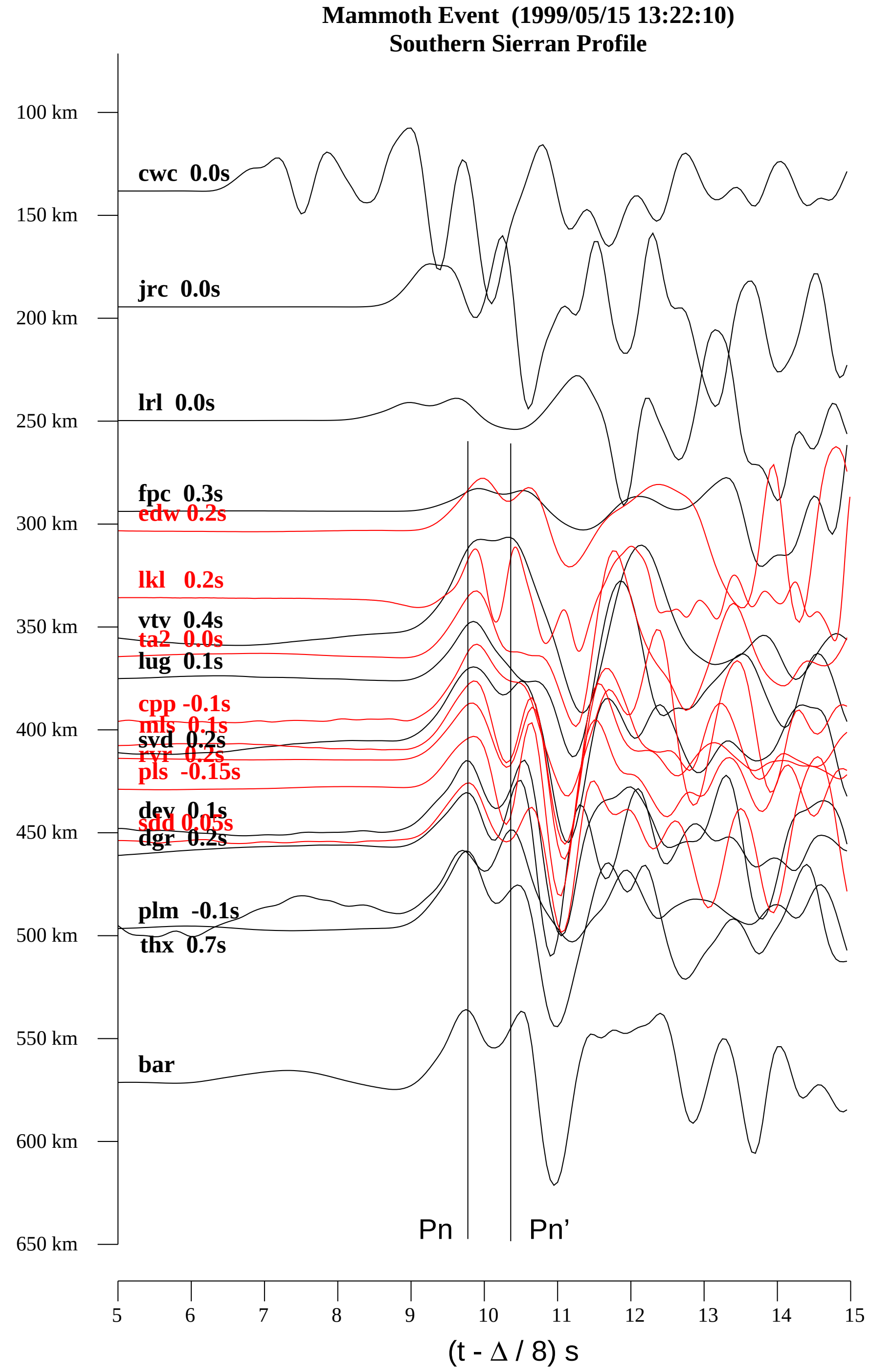

Figure 1.7: Record section from swath 2 showing waveform data traversing the southern Sierra Nevada (Figure 1.5). Notice two arrivals Pn and Pn’, indicated by gray boxes, arriving less than 1 second apart and the large downswing associated with the later Pn’ arrival. The data is reduced using a velocity of 8.0 km/s. Time shift required to align Pn is shown after the station name, a positive shift moves the trace to the right. Synthetics for crustal and mantle anomalies are computed to explain the shape and timing of the Pn arrivals.

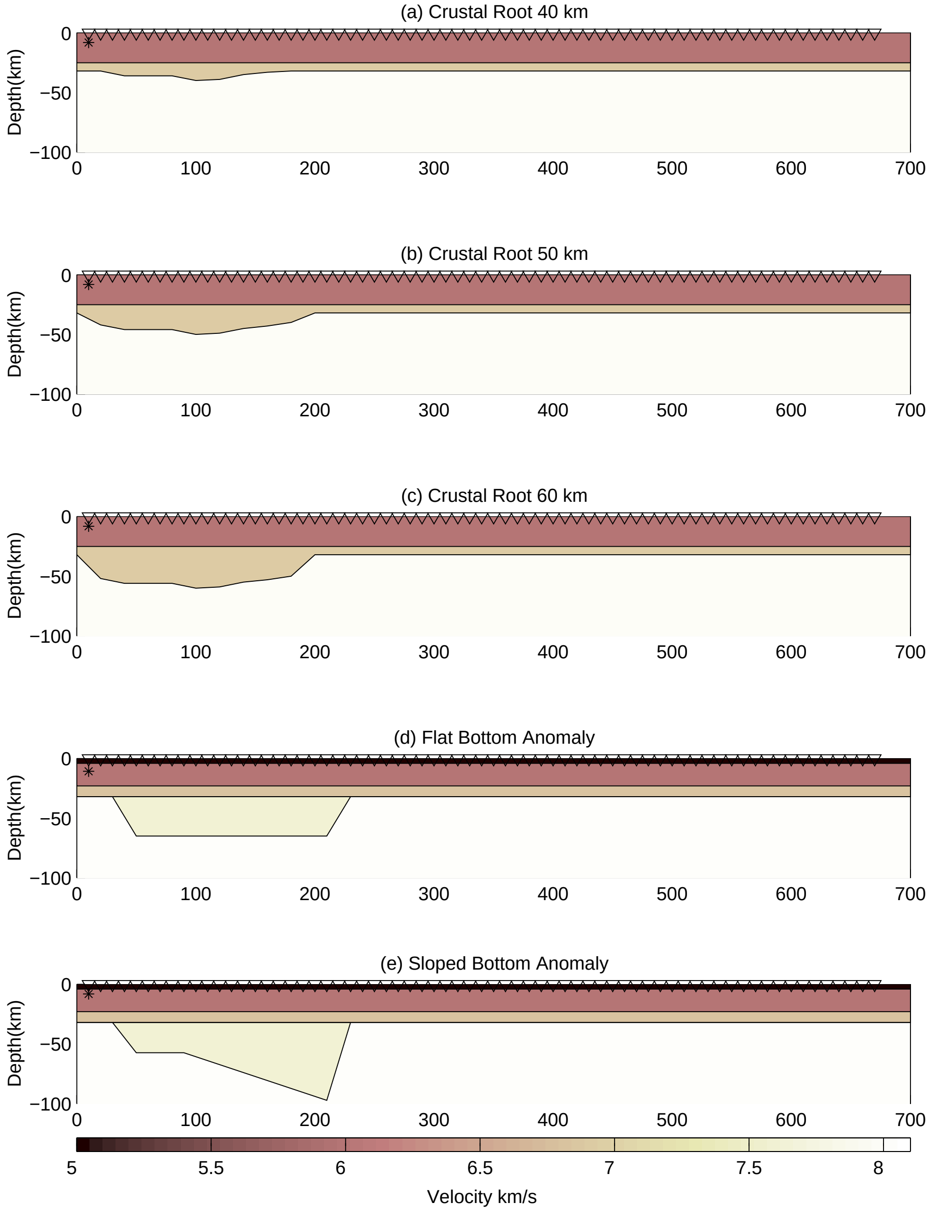

Figure 1.8: a,b,c) Three models of crustal roots derived from *Pakiser and Brune* [1980] to explain the arrival times from the 1966 Truckee Earthquake. The maximum crustal thicknesses are 40 (a), 50 (b) and 60 km (c), while the crustal thickness at near the reciever is 32 km. A discontinuity at 25 km separates the 6.1 km/s upper crust from the 6.9 km/s lower crust and root. d) Velocity model with a flat bottomed anomaly, 7.6 km/s, just below the crust extending down to 75 km. e) Refinement of the model in d) by addition of a sloped bottom to align Pn and Pn'. This refinement puts the maximum depth at 100 km. Lighter shades are faster velocities. All models have sources, stars, in the north, left edge, and the waves propagate to the south, right edge.

The north-south profile from *Pakiser and Brune* [1980] was scaled to create crustal roots of differing depths and to assess how well a crustal root model explains the data in swath 2. Each crustal root model produces two distinct arrivals, Pn and sPn (gray boxes), for a given crustal thickness (Figure 1.9). The crustal thickness only affects the absolute timing of Pn and sPn, with thicker crustal roots producing a larger travel time delay in the arrival of each Pn phase. The main flaw of all of these model synthetics is that they do not include the large arrival, Pn′, seen in the data with its associated negative pulse. For a crustal thickness of 50 km, the Pn arrival appears trapezoidal, not triangular as for crustal thicknesses of 40 and 60 km. The trapezoidal shape results from Pn interfering with reverberations in the crust. However, this second arrival from the 50 km crustal root does not contain a downswing, as in the data.

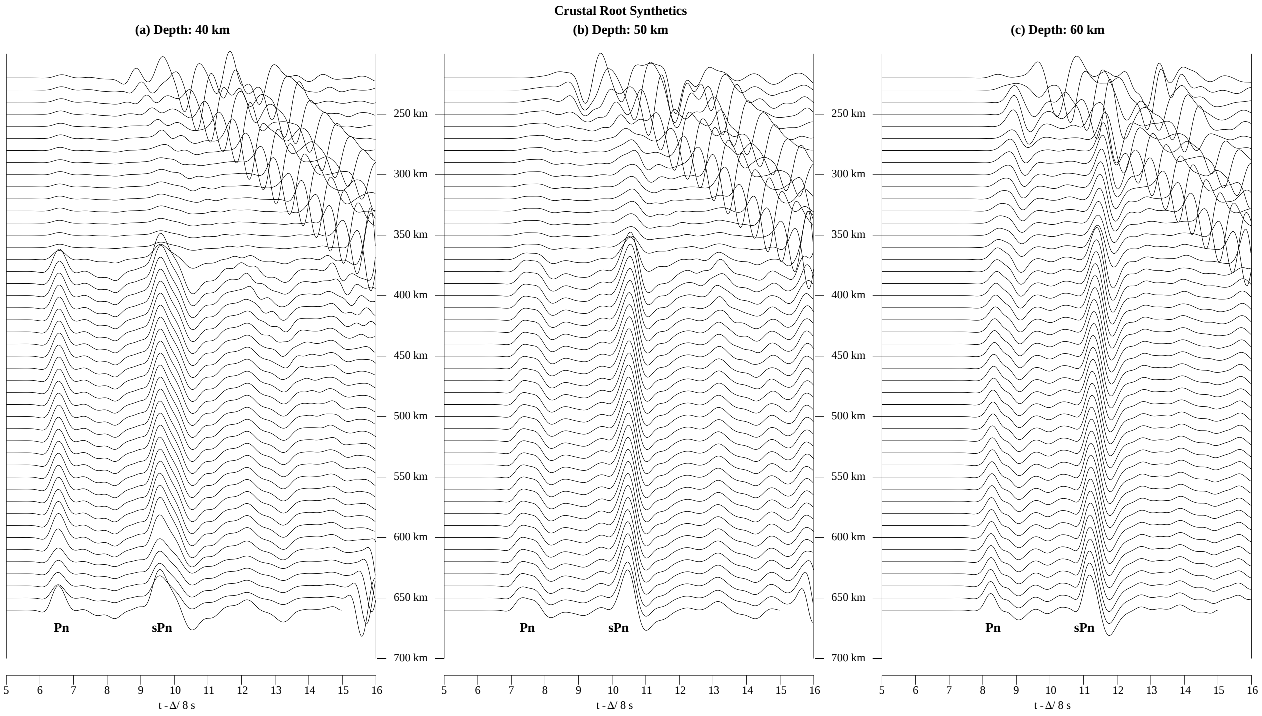

Figure 1.9: Synthetics for the three crustal root models derived from *Pakiser and Brune* [1980] and shown in Figure 1.8 a,b,and c. Note that only the 50 km crustal root model shows two arrivals for Pn, forming a trapezoidal shape, but it lacks the large downswing associated with second arrival, Pn', which is present in the data, Figure 1.7. Pn and sPn are highlighted in the gray boxes.

1.5.2.2 b) Low Velocity Mantle

As an alternative to the crustal root models, we examine the effects on regional waveforms using models with a lower velocity mantle structure. As shown before in Figure 1.3, a simple 1-D crustal model over a half-space mantle will produce simple arrivals. We can predict the Pn travel time variation by splitting the mantle into slow and fast regions, but we cannot reproduce the second arrival, Pn′. The second arrival, Pn′, appears to be a reflection not a refraction. Refraction arrivals, like Pn, appear triangular-like in velocity, while post-critical reflections are double-sided, a positive triangular pulse followed by a negative triangular pulse, like Pn′. If we add a slow velocity near the source (left side of Figure 1.8d) with a discontinuity at its base we can reproduce the second arrival, Pn′. Since the discontinuity is deep it does not affect Pn. A wave with a slightly different raypath will reflect off this boundary, and subsequently follow a path similar to Pn. Figure 1.8d and e show two models producing a second arrival, Pn′. The arrival times of Pn and Pn′ in Figure 1.10 are controlled by the velocity and the depth of the anomaly. The model in Figure 1.8d has a velocity of 7.6 km/s and a base at a depth of 75 km. A velocity of 7.6 km/s is similar to that reported by *Carder* [1973] and *Zhao* [1993]. The second arrival, Pn′, is the reflection off the discontinuity, but still a part of the Pn wavefield. An anomaly with a flat bottom (Figure 1.8d) produces arrivals Pn and Pn′ which intersect each other at ∼400 km epicentral distance (Figure 1.10a). The waveforms in Figure 1.10a shows how Pn intersects with Pn′ to produce one arrival. At distances less than 350 km Pn′ travels much slower than Pn, as it must travel to the discontinuity and back entirely within the anomaly. At distances greater than 350 km the reflection travels in the mantle just below the Moho, similar to a refraction in speed but arrives double-sided in shape. By dipping the discontinuity away from the source (Figure 1.8e), the arrival of Pn′ at larger distances does not interfere with Pn (Figure 1.10b) instead producing two distinct arrivals. Based on these observations Figure 1.8e is our preferred model. The low velocity, 7.6 km/s, explains the travel times of Pn and a 10°-15° south dipping discontinuity with the depth in the north at ∼75 km and ∼100 km in the south produces two arrivals 0.75 - 1.0 sec apart for over 300 km in distance.

The low velocity zone in our preferred model is well resolved except on the source side. The low velocity zone in the mantle is immediately below the crust, constrained by

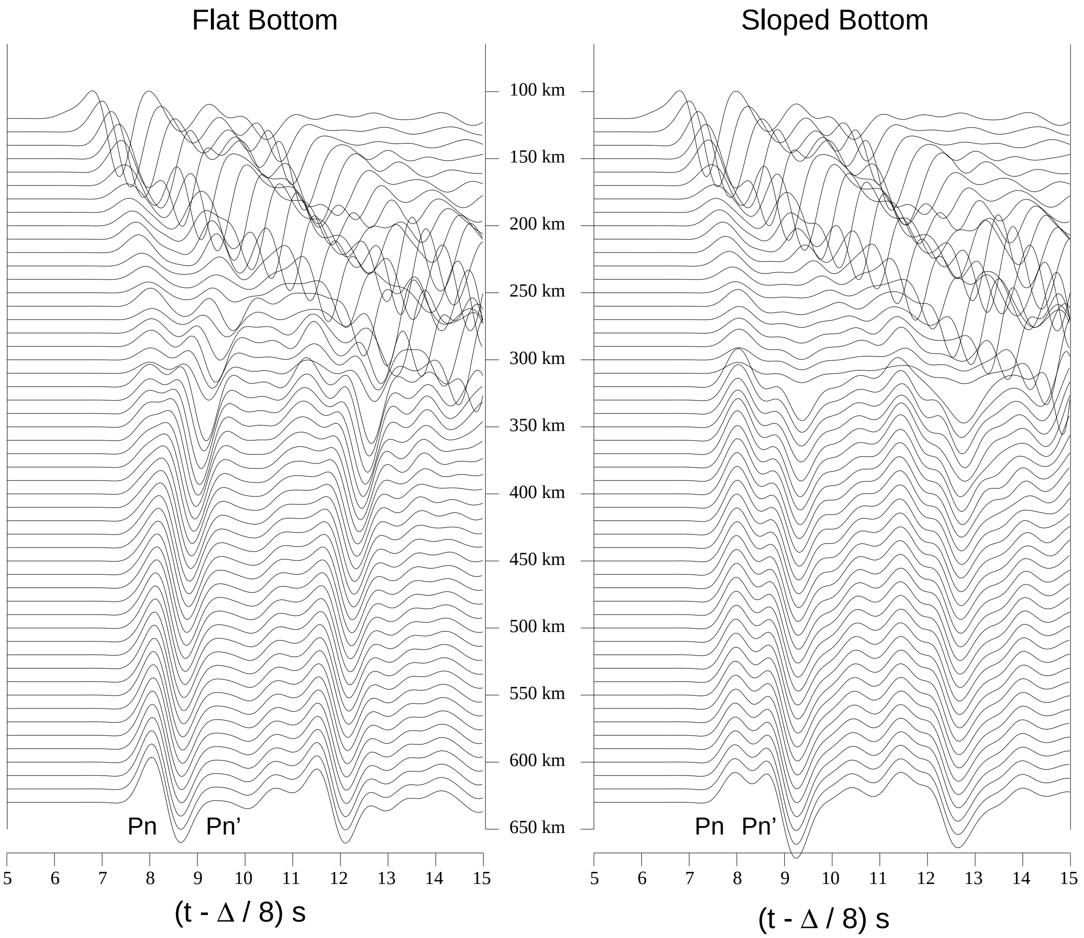

Figure 1.10: Synthetics for the two mantle velocity anomalies shown in Figure 1.8 d and e. The flat bottomed anomaly, left, produces two arrivals, a single-sided Pn (dark-gray box) and a double-sided Pn’ (light-gray box), similar to the data in Figure 1.7, but at large distances the arrivals converge (intermediate-gray area). However, if the bottom of the anomaly is sloped away from the source, as shown in Figure 1.8e and right record section, then Pn and Pn’ do not intersect but matain a consistent travel time difference, in accordance with the data (two independent gray boxes).

waveform modeling. The depth of the discontinuity is proportional to the relative travel time of Pn$'$ with respect to Pn. A deeper discontinuity produces larger time delays between Pn and Pn$'$, while a shallow discontinuity reduces the relative travel time between Pn and Pn$'$. However, the depth of the discontinuity does trade off with V_p in the low velocity zone. If the discontinuity is replaced with a gradient, the Pn$'$ arrival becomes longer period and lower in amplitude. The Pn$'$ arrival is impulsive with a large amplitude, from this we conclude the boundary is nearly a discontinuity. The same discontinuity at greater than

150 km depth does not produce the Pn$'$ arrival. By using the relative amplitude and timing of these phases we can constrain the southern boundary of the low velocity zone. However, dramatic changes in the Pn wavefield do occur between stations VTV and TA2 indicating this structure we explain with a simple 2-D model is more complicated than modeled here. Shifting the entire low velocity zone to the left, or north, by 10 km increases the relative amplitude of Pn with respect to Pn$'$ and the time separation between Pn and Pn$'$ also increases. As the low velocity zone is shifted south, the relative amplitude of Pn decreases as does the relative travel time between Pn and Pn$'$. The same effect occurs by only shifting the southern boundary. In contrast, by only shifting the left or northern boundary, the waveform shapes and travel times do not change appreciably. This indicates that we are not sensitive to the northern extent of the slow velocity region, but can constrain the southern boundary to within $\sim$10 km. The poor sensitivity in the north results from Pn entering the low velocity zone from the top and never sampling the northernmost portion of our study area. The southern boundary, coincident with the surface trace of the Garlock Fault, is well sampled by the Pn waveforms studied in swath 2.

1.5.2.3 c) Model Comparison

Velocity waveform data from station PLM at a distance of 500 km is plotted (Figure 1.11) against synthetics from a layer over a half-space (1-D), a 50 km crustal thickness model (Figure 1.8b) and our preferred model (Figure 1.8e). The 1-D model fails to explain the anomalous second arrival, Pn$'$. The 50 km crustal thickness model produces complex Pn behavior. The thicker crust produces a second arrival which makes Pn appear trapezoidal in shape. The second arrival, while consistently trailing Pn by 0.5-1.0 sec is not double-sided as seen in the data. Our preferred model with a discontinuity at 75-100 km beneath a low velocity mantle, produces an second arrival, Pn$'$, similar to the double-sided arrival in the data. The reflection creates a double-sided arrival in velocity, thus producing a large downswing.

1.5.3 Swath 3

Vertical velocity data from swath 3 (Figure 1.5) is plotted in Figure 1.13. This swath begins in Mammoth and trends toward the Mojave desert. The two arrivals, marked as Pn and Pn$'$, are less than a second apart and there are no additional signals until the arrival of the

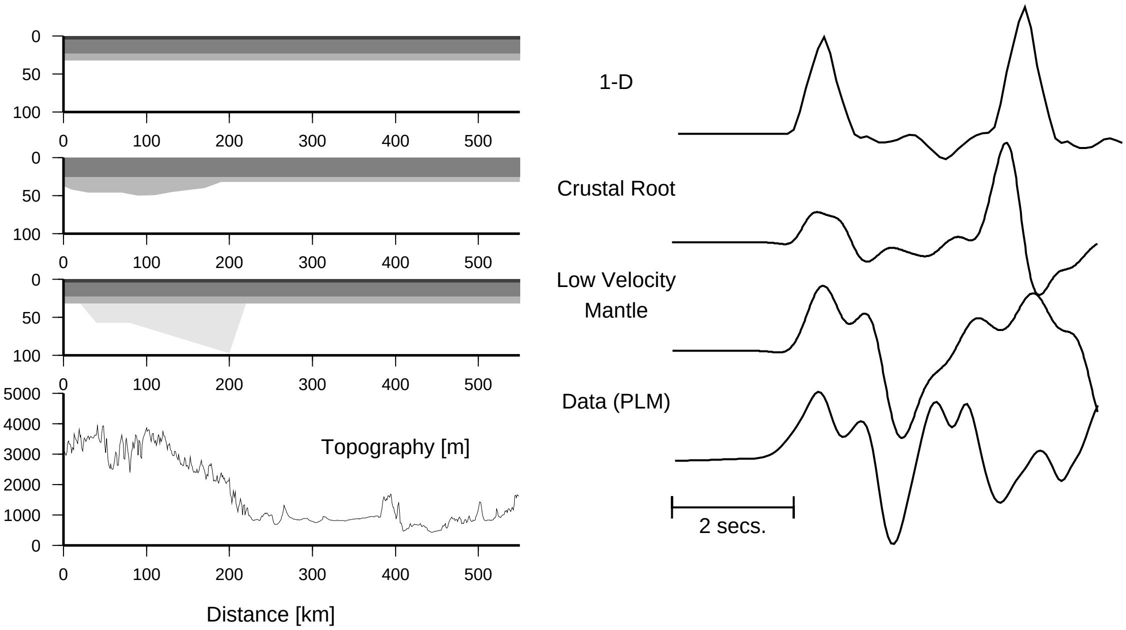

Figure 1.11: Comparison of three velocity models and associated Pn waveforms with data recorded at station PLM (Palomar, CA, $\Delta = 500km$) from swath 2. The first row shows the model of a layer over a half-space similar to Figure 1.3 and synthetic Pn waveform. The second row shows the 50 km thick crustal model of Figure 1.8 b, and third is the preferred model of Figure 1.8 e. All waveforms are vertical velocity data at 500 km epicentral distance. Notice the large downswing of Pn' in the data and mantle velocity anomaly synthetic, which is absent in the crustal model and layer over a half-space. A topographic profile is provided for reference at the base of the model panel. The suface expression of the profile is shown as a dashed line in Figure 1.12

reflection from the Moho, PmP. The relative timing between Pn and Pn′ is similar to that seen on the southern Sierra Nevada profile. Modeling this swath with the preferred model (Figure 1.8e) produces the arrivals Pn and Pn′ with relative timing and amplitude similar to that found in the data. The depth phase, sPn, exhibits amplitude differences between the data and synthetics due to the source mechanism as sPn approaches a node at this azimuth. However, trying to predict amplitudes near a source mechanism node is difficult because small changes in the source mechanism can create large changes in amplitudes. Waveforms data from this swath shows that the preferred model also explains the double-sided pulse, Pn′, for paths which traverse the southern Walker Lane extending out to Death Valley.

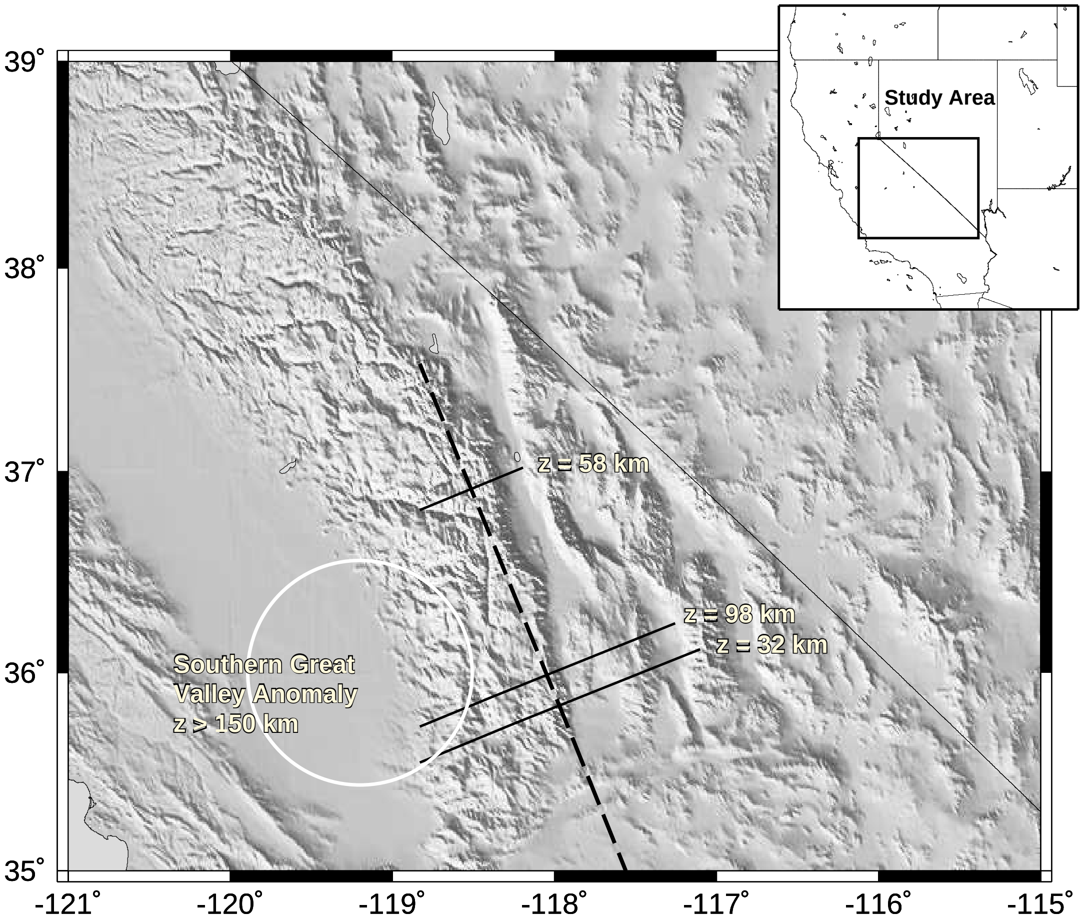

Figure 1.12: Regional map of the southern Sierra Nevada and Walker Lane showing the Southern Great Valley Anomaly and "kink" points in our preferred model. The southern Great Valley Anomaly (circle) [*Biasi and Humphreys*, 1992] is a region of high velocity at a depth of approximately 150 km. The solid lines indicate the "kinks" in the base of the low velocity zone of our preferred model (Figure 1.11). A dashed line trending at an azimuth 157.5° from Mammoth, CA (Table 1.1) displays the location of the topographic profile in Figure 1.11 which is close to the median of swath 2.

1.5.4 Swath 4

Swath 4 (Figure 1.5) contains the complementary crossing swath from the Nevada earthquake and we plot its record section in Figure 1.14. This swath occurs near a amplitude node for Pn and exhibits small amplitudes in comparison to the swaths discussed previously. Perturbations in the source mechanism of 20° in rake dramatically change the amplitudes of the arrivals at this azimuth (∼190°). With a nodal Pn, the first arrival is Pn′ and the

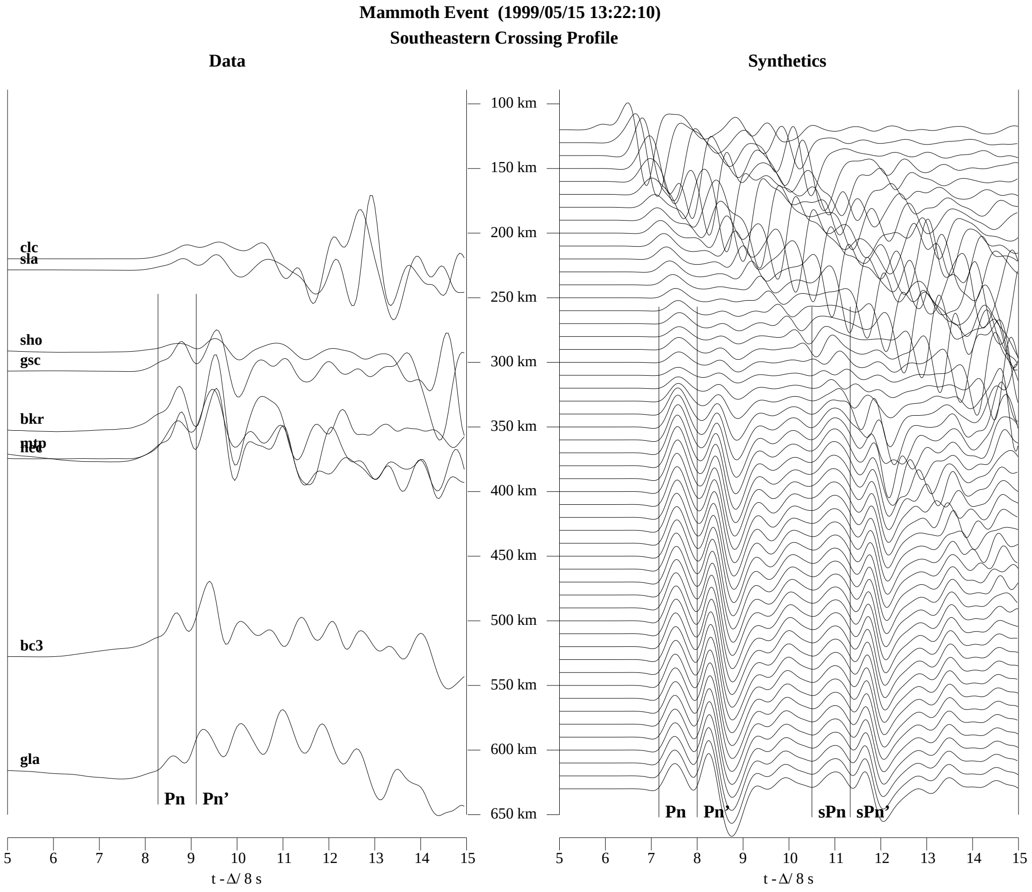

Mammoth Event (1999/05/15 13:22:10)
Southeastern Crossing Profile

Figure 1.13: Velocity data and synthetics for the southeastern crossing swath for the Mammoth event, swath 3 in Figure 1.5. The low amplitude of sPn relative to Pn in the data and synthetics is due to sPn being near nodal for this azimuth. Notice the large downswing associated with Pn’ at stations near 350 km. This is similar to data seen in swath 2 and synthetics computed for Figure 1.8e.

second and third are pPn and sPn (marked in Figure 1.14). A simple 1-D model, as used for data further to the east, only produces 3 isolated pulses, which do not match the complex waveforms for this swath of data. However, use of the velocity structure of our preferred model produces the extra arrivals needed to match the data, marked as Pn′, pPn′, and sPn′ in Figure 1.14. Again, near nodal arrivals complicate the resulting waveforms. Energy arriving near a node is weakly coherent and could appear shifted in time due to velocity perturbations. Nevertheless, coherent arrivals at distances >325 km are apparent and marked in gray boxes in Figure 1.14. Our preferred velocity model explains seismic wave propagation through the southern Sierra Nevada and Walker Lane.

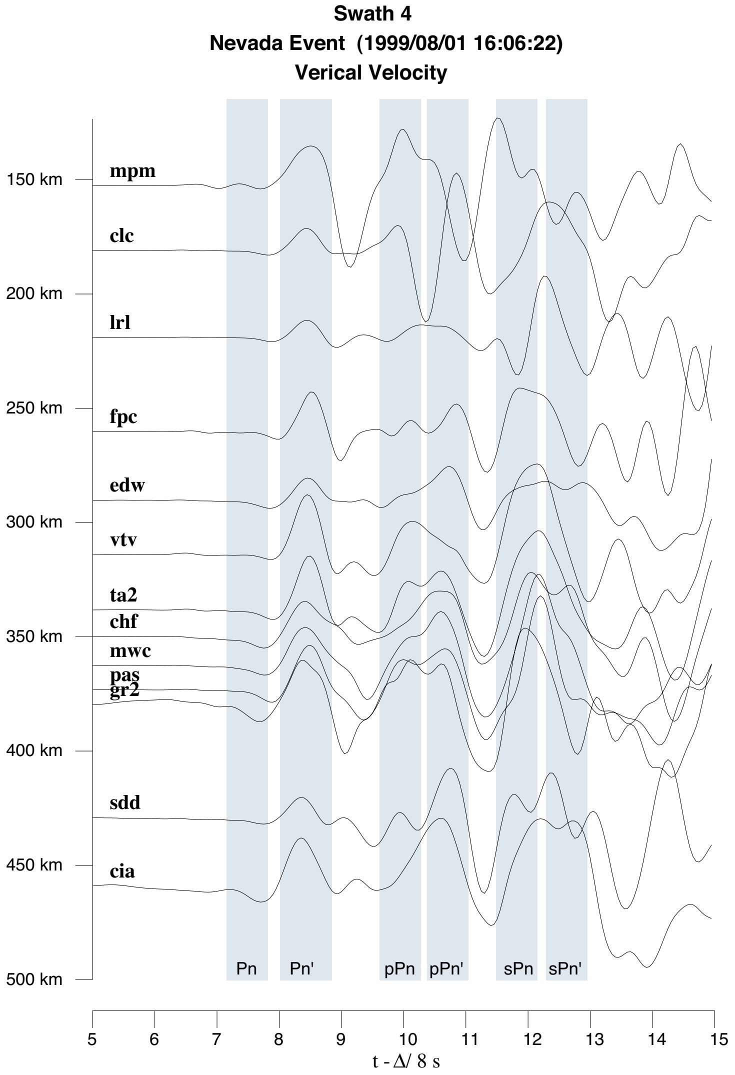

Figure 1.14: Data from the Nevada event which propagates southwest, swath 4 in Figure 1.5. This data is explained by the preferred model, Figure 1.8 e, but, full waveform modeling becomes difficult as the data is near nodal. However, double arrivals are present for Pn, pPn and sPn, as for swaths 2 and 3, especially at larger distances, > 325km. Gray boxes are used to identify approximate arrival times of Pn, pPn and sPn as the wave shape may appear to perturb arrival times near a node.

1.6 Gravity

The densities in the preferred model can be reconciled with gravity observations. Modeling of gravity data in a east-west profile across the Sierra Nevada and Basin and Range by *Fliedner and Ruppert* [1996] places density variations within the upper mantle rather than the crust. While the same gravity data can also be explained by using only crustal density variations, *Fliedner and Ruppert* [1996] state that the overall crustal density would then deviate from a reasonable crustal average. Converting the low mantle velocities of the preferred model (Figure 1.8e) into densities, as accomplished by *Schmitz et al.* [1997], renders variations of ~60 - 140 kg/m^3 [*Fliedner and Ruppert*, 1996] between the surrounding mantle and the low velocity region. Using a density variation of 80 kg/m^3 at depths from 35 - 75 (or 100) km produces an Bouguer gravity anomaly of ~-100 (or -140) mgals. An anomaly of -100 mgals in Walker Lane is therefore explained by either the modeling of *Fliedner and Ruppert* [1996] or our preferred model. While our preferred model may overestimate the gravity anomaly, partial melt in small percentages reduces the Bouguer gravity magnitude [*Schmitz et al.*, 1997] to less than -100 mgals. Our preferred model agrees with the Bouguer gravity if we assume a velocity-density relation with a possibility of partial melt in the upper mantle.

1.7 Conclusions

A low velocity V_p 7.6km/s anomaly is present underneath the Sierra Nevada and Walker Lane. There is also a large velocity discontinuity at approximately 75-100 km depth, dipping southward at 10-15°. A thick crustal root does not explain the Mammoth Lake earthquake waveform data along the Sierra Nevada axis (Swath 2) due to the lack of an double-sided arrival following Pn (Figure 1.11). The western edge of the low velocity zone is beneath the Sierra Nevada and extends to the east beneath Death Valley. The southern extent does not cross the Garlock fault but becomes deeper while approaching this boundary. The eastern edge of this anomaly does not extend past Death Valley. From the modeling of recordings from swath 1, a simple flat-layered velocity structure (Table 1.3) is suggested for the eastern Mojave and east of Death Valley. Data from swath 2 shows similar behavior as swaths 3-4, with a prominent secondary arrival, Pn′. Our results compare well with those of *Carder et al.* [1970],*Carder* [1973],*Savage et al.* [1994], and *Fliedner et al.* [2000]. The absence of a high velocity lower lithosphere in our model compares well with the tomography studies from *York and Helmberger* [1973], *Biasi and Humphreys* [1992], *Zhao* [1993], and *Pollitz* [1999] that indicate a low velocity mantle beneath the southern Sierra Nevada. The structural components above are compatible with models from *Wernicke et al.* [1996] and *Jones and Phinney* [1998], but the large velocity discontinuity at 75-100 km is a new model feature.

Integrating our inference of a large-scale discontinuity at depth (75-100 km) and previously reported low velocity mantle below the southern Sierra Nevada and Walker Lane [*Carder et al.*, 1970; *Carder*, 1973; *Biasi and Humphreys*, 1992; *Zhao*, 1993; *Savage et al.*, 1994; *Fliedner et al.*, 2000] in a tectonic framework is complex. Development of the Sierra Nevada and its underlying mantle lithosphere initially occurred during subduction between the North American and Farallon plates. Subduction along the western North American border continued with varying degrees of slab dip until 28-19 Ma. At that point in time, a slab-window, or slab-gap, marking the end of subduction began to form. As the slab-window grew larger and migrated northward, the oceanic lithosphere sank and left hot asthenosphere in contact with the upper crust to the west of the Sierra Nevada [*Atwater and Stock*, 1998]. Development of a slab window and cooling asthenosphere produces convective instabilities which form drip-like structures in the upper mantle [*Zandt and Carrigan*, 1993; *Houseman et al.*, 2000]. At 6 - 8 Ma the lithosphere of the Sierra Nevadas disappears [*Ducea and Saleeby*, 1998c], leaving hot asthenosphere below the Sierra Nevada. At approximately the same time, ∼8 Ma, the relative motion of the Pacific plate to North America rotated to a more northern direction.

Verifying the existence and location of the subducted slab (Farallon plate), a possible drip-like structure, and location of a missing mantle lithosphere is useful in constraining tectonic and dynamic convection models. Firstly, the subducted slab is likely underlying the northern Sierra due to a component of northern velocity during subduction. Secondly, the drip-like structure is reportedly seen tomographically [*Biasi and Humphreys*, 1992] as a cylindrical high velocity structure at 150 - 200 km depth called the Southern Great Valley Anomaly. Several mechanisms could be responsible for the disappearance of the Sierra Nevada mantle lithosphere. Either the lithosphere detached from the upper crust above it and sunk into the surrounding mantle or the lithosphere was chemically incorporated into the mantle. Our results show a discontinuity at depth and thus support the sinking lithosphere hypothesis. We hypothesize the discontinuity as the old contact between the Sierra Nevada lithosphere and crust. Moreover, mantle flow resulting from a sinking lithosphere will fill the area left by the sinking lithosphere from the neighboring sides and below. If the flow originates from the hotter asthenosphere below then it could be the mechanism that places lower velocity, hotter mantle at the base of the crust. Dynamic models with realistic density and viscosity variations are necessary to accurately test if these structures are viable.

Acknowlegdements

We would like to thank Jascha Polet, Hiroo Kanamori, Egill Hauksson, Matt Pritchard, Jeroen Ritsema, and Mark Simons as well as two anonymous reviewers for their reviews. We would also like to thank Alisa Miller, Pete Savage, Nathan Niemi, Rowena Lohman, and Jason Saleeby for their helpful discussions, and TriNet and Berkeley Digital Seismological Network (BDSN) for seismic waveform data. This research was supported by the Defense Threat Reduction Agency under contract DSWA01-98-1-0010. Contribution No. 8827, Division of Geological and Planetary Sciences, California Institute of Technology, Pasadena, California.

Chapter 2

Velocity Structure of the San Bernardino Mountain Crust and Mantle

2.1 Introduction

The southern California bend in the San Andreas fault has resulted in convergence producing the Transverse Ranges. Tomographic studies have shown a higher velocity mantle beneath the Transverse Ranges and thought to be due to a downwelling of material from the upper mantle[*Kohler*, 1999]. Receiver function studies [*Zhu and Kanamori*, 2000] and analysis of Moho reflections [*Richards-Dinger and Shearer*, 1997] show a thickening of the Transverse Ranges crust towards the east and the San Bernardino Mountains. This work adds to the preexisting data for the Transverse Ranges particularly the San Bernardino Mountains.

2.2 Method

Through the use of the regional earthquake wavefield we will determine the seismic structure of the crust and upper mantle of the San Bernardino Mountains and adjacent provinces. In particular, we use the Pn arrival which samples the lower crust and uppermost mantle. Figure 2.1 displays a regional map of southern California including two Mexican earthquakes and TriNet broadband stations used in this study. Black triangles indicate those stations which provide pertinent seismic waveform data. The station spacing of TriNet allows for a swath of data to be examined and modeled using arrival times. In addition, the broadband instrumentation allows for modeling of the shape and amplitude of the seismic waveforms.

Using a forward modeling approach implementing 2-D finite difference[*Helmberger and Vidale*, 1988], various models of the San Bernardino Mountains can be tested and appraised.

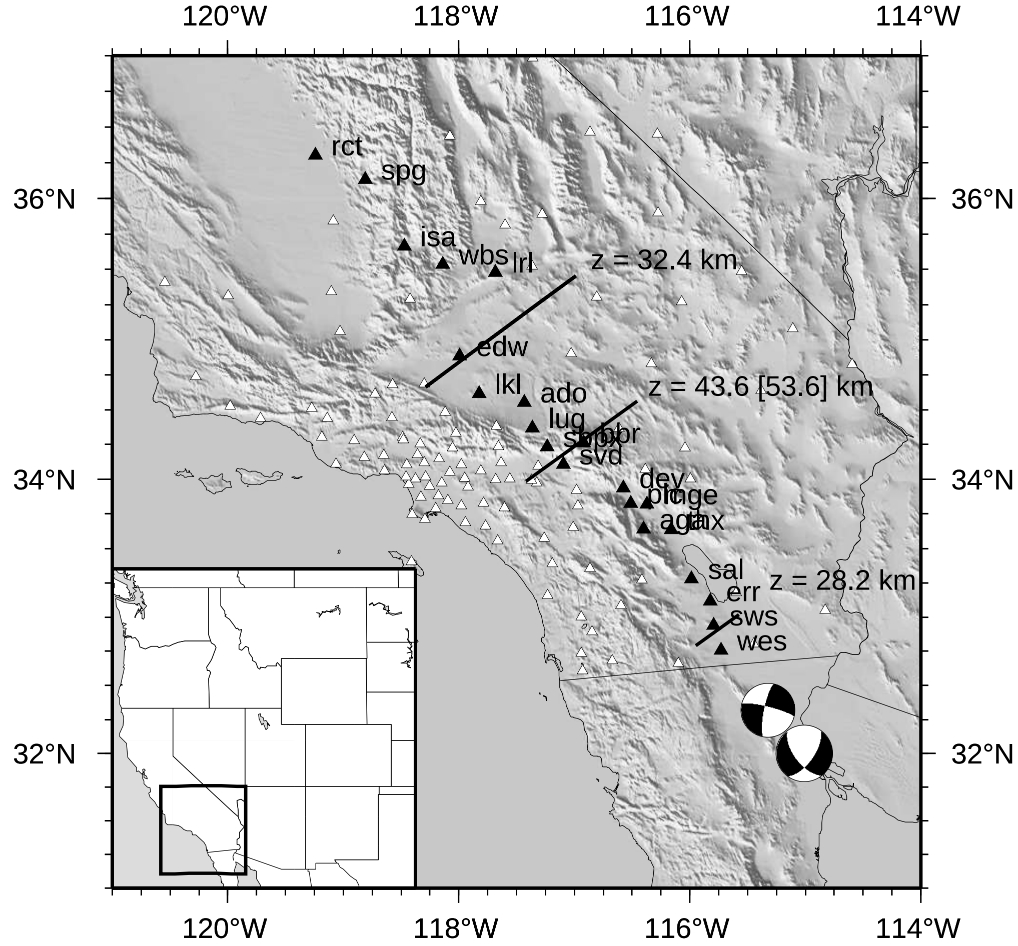

Figure 2.1: Map of southern California and northern Mexico displaying two earthquakes and the TriNet broadband network used in this study. The white triangles are all the TriNet stations and the black triangles are those used to investigate the crust mantle interface beneath the San Bernardino mountains. The roughly east-west lines are "kink" points of the Moho in our preferred model, discussed later.

2.3 Data

Figure 2.2 shows seismic waveform data from two earthquakes (12/08/2002 5.8 M_w USGS and 02/22/2002 5.5 M_w USGS). Plotting these data as a reduced record section with a velocity of 4.3 (SH) or 7.8 (Pn) km/sec, aligns the first arrival. In this section of data the Pn wavefield, including the depth phases pPn and sPn, is complex. The same is true for the SH arrivals. Throughout the entire array, all Pn arrivals exhibit the same complex behavior, however the remainder of the seismogram is not as consistent throughout the entire array [*Savage and Herlmberger*, 2004b]. We attribute this overall complexity to near source structure. Arrival times of the depth phases pPn and sPn show a similar pattern to Pn, therefore we only use the Pn arrival times. By identifying SH or Pn and plotting its arrival time in Figure 2.2, a dramatic decrease in arrival time is apparent. Time picks are plotted as small circles and connected by straight lines, only for Pn. We compute and plot expected SH arrival times from the Pn times multiplied by 1.8 (Poission's Ratio $\nu = 0.276$). The agreement between the actual and expected SH arrival times is dramatic. Due to the complex Pn behavior, the initial break and maximum amplitude of Pn are both picked. Dramatic differences between all four Pn arrival time sets are not apparent. The maximum delay for both types of arrivals occurs near station ADO and approaches 1.5 seconds for Pn and 2.5 seconds of SH. Tangential SH arrivals only provide further confirmation that the delay along this profile exists and are not modeled in a similar fashion as the Pn data.

The apparent Pn velocity seen in Figure 2.2 from THX (211 km) to ADO (362 km) is 7.2 km/sec. A velocity slower than 7.5 km/sec for the uppermost mantle and not crustal material would indicate the presence of melt and very high temperatures at the base of the crust. By extending slower crustal velocities, < 7.2 km/s, into the mantle produces the arrival time delays in the data. Further, from ADO (362 km) to LRL (459 km) the apparent velocity is 8.85 km/s. Compressional wave velocities of this magnitude are found deeper than 200 km, not near the base of the crust.

To model the Pn travel time data, we start with the previously published results of *Zhu and Kanamori* [2000]; *Richards-Dinger and Shearer* [1997]. In particular the results of *Zhu and Kanamori* [2000] were incorporated into the Southern California Velocity Model Version 2 (SCECV2) [*Magistrale et al.*, 2000] along with upper crust velocity variations. A simplified cross section of the *Zhu and Kanamori* [2000] model from the northern most earthquake through station ADO in the southern Mojave desert is shown in the center panel of Figure 2.3. We simplify the cross section by removing crustal heterogenities to resolve where the delays arise. At approximately 315 km along this profile the Moho deepens by 15 to 20 km then returns back to a standard 35 km thickness.

Travel times from finite-difference models are displayed as black lines in the left panel of Figure 2.3. From 225 km to 375 km, the simplified *Zhu and Kanamori* [2000] model shows

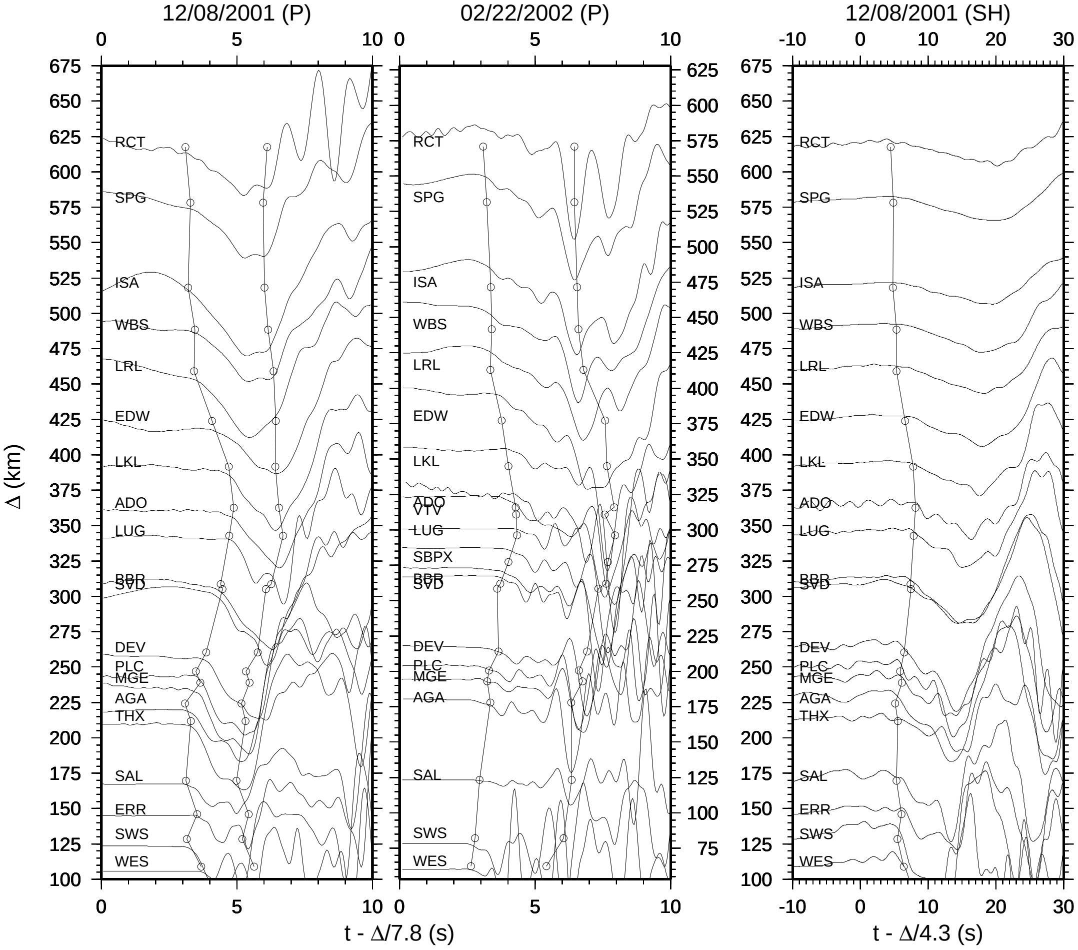

Figure 2.2: Pn data from two earthquakes in northern Mexico are displayed here as a record section. The SH and Pn portions of the seismogram are shown. Reduction velocities of 4.3 (SH) and 7.8 (Pn) km/s are used to align each arrival. The earthquake record section are aligned geographically so stations appear at the same places. Small circles on Pn times denote time picks of the initial break of and maximum absolute amplitude of Pn. These circles are connected by straight lines to guide the eye. A maximum delay of 1.5 seconds is apparent for both earthquakes at stations ADO, LUG and VTV (only 02/22/2002). Time delays for SH and Pn are apparent between stations DEV and WBS. The time picks on the SH records are derived from the Pn times multiplied by 1.8 (equivalent to a Poission's ratio of 0.276).

a similar time delay as in the data, red line with circles in the left panel of Figure 2.3. While the arrival time delay is present, its magnitude and position are incorrect. To increase the delay time we increase the thickness of the crust by 10 km, and plot the arrival times again as a black line. This increased crustal thickness adds slower velocities into the Pn path, increasing the magnitude of the delay. A thicker crust produces a magnitude delay similar

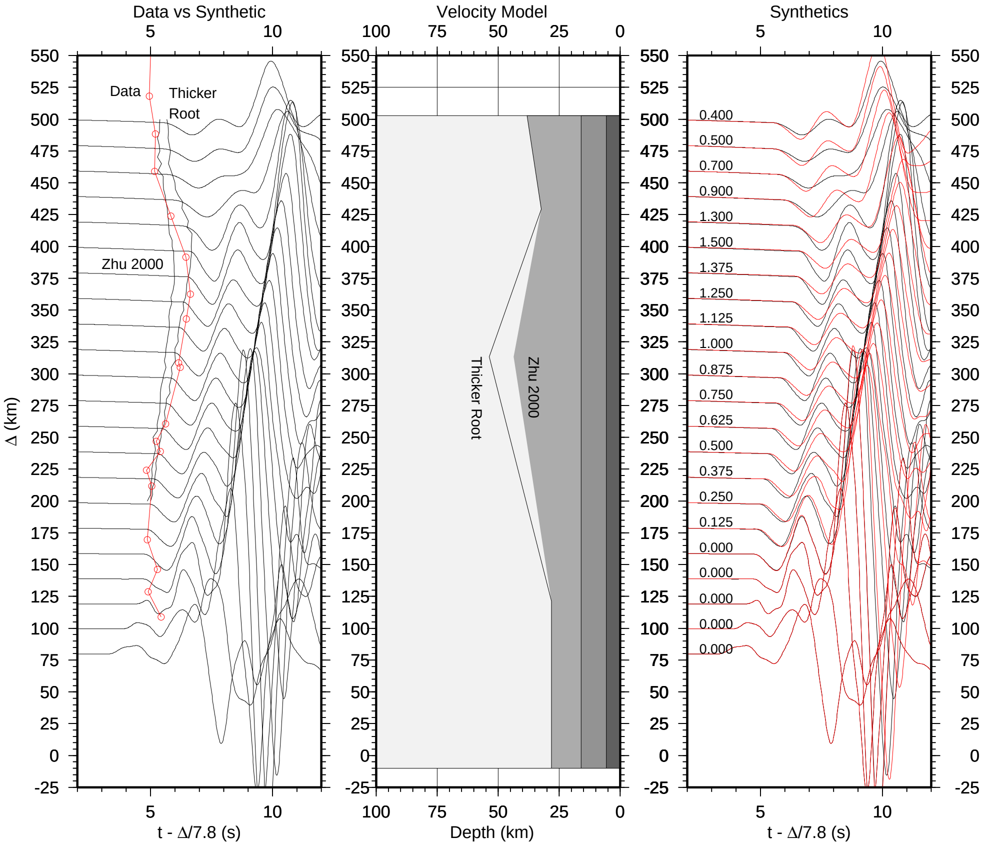

Figure 2.3: Left panel. Travel times from event 12/08/2001 (initial break) are plotted with circles, similar to Figure 2.2. The two other black lines displays the finite difference synthetic time picks from the simple SCECV2 model and the same model but with a thicker crust. Synthetic waveforms for only the deeper model are plotted. Center panel. Finite difference model of the simplified SCECV2 velocity model and the same model but with a deeper crust. The simple SCECV2 is plotted with shading and the deeper model is only displayed with solid black lines. The darker the shade the slower the velocity. Right panel. Synthetics from the deeper crustal model (black) and a model with no crustal root (red). Time shifts, required to align the onset time of the no crustal root synthetics with the deeper crustal root synthetics, are displayed on the left hand side of the panel. Notice the change in amplitude and frequency content when Pn encounters the deeper root.

to the data, but the position of this maximum delay is still incorrect.

2.4 Analysis

Figure 2.3, right panel, displays the differences in the synthetics between the deep Moho model and the flat layered model. Flat Moho synthetics are shifted to match the onset time of the deep Moho synthetics with the time indicated on the left. The higher frequency content of arrivals diminishes as the delay times grow. This is seen in a comparison of the amplitude of the first arrival. Following the maximum time delay, the first arrival for the deep Moho model becomes much longer period and smaller in amplitude than for the flat layered model. At this distance, Pn is within the middle of a shadow zone created by deep crustal root. Within the Pn wavefield any diffracted wave, the highest frequencies are nearest to the generating interface. Addition of the crustal root creates a barrier for these high frequencies but allows the longer periods to pass below. Therefore the crustal root effectively becomes a low pass filter.

To determine where the position (x) of the receiver for an arrival from the Moho of depth (z_m) we need the velocity contrast between the crust (V_c) and the mantle (V_m). The contrast defines the angle, $i = \sin^{-1}(V_c/V_m)$, at which the Pn arrival emerges from the mantle. Using simple geometry the distance becomes

$$x = z_m \tan\left(\sin^{-1}\left(V_c/V_m\right)\right) \tag{2.1}$$

The maximum depth in the simple *Zhu and Kanamori* [2000] model is 43 km and the velocity contrast at the Moho is 6.7 to 7.8 km/sec, which gives a horizontal offset of over 70 km. By increasing the crustal thickness by 10 km this offset increases to over 90 km.

Sensitivity tests were carried out regarding the crustal root position, Appendix B. These indicate that by shifting the crustal velocities forward and backwards within the profile only results in shifting the relative position of the delays but not their overall character. From this, we are able to shift the crustal root along the profile guided by the delay times, 40 km towards from the source. Sensitivity tests were also conducted on the crustal velocities. A change of crustal velocity by 5% over 20 km only results in a delay less than 0.20 s of travel time. This suggests the majority of the delay originates from the difference of the crust and mantle velocities. Including reduced crustal velocities would result in a thinner crust. A comparison of our simple model and SCECV2 shows our model as faster, thus our estimate is an upper bound of crustal thickness in the region.

2.5 Conclusions

From identification of Pn arrivals and simple 2-D modeling we are able to place constraints upon the crustal and mantle structure beneath the San Bernardino Mountains. The waveforms across the San Bernardino Mountains show SH and Pn delays from up to 2.5 seconds (SH). Our modeling suggests the crust of the San Bernardino Mountains is near 50 km thick with the maximum beneath the greatest topography. The crust of the *Zhu and Kanamori* [2000] model and consequently the SCECV2 model have the correct Moho shape but they are offset by 40 km to the northwest and require 10 km more of crustal material.

Acknowledgements

This research was funded by United States Geological Survey under Grant 02HQGR0063. This is Contribuition No. 8953, Division of Geological and Planetary Sciences, California Institute of Technology.

Chapter 3

Site Response from Incident *Pnl* Waves

3.1 Introduction

Characterization of how a seismic station responds to incident seismic waves, or site response, is important to many aspects of earthquake research. First, it describes which areas are prone to violent shaking during large earthquakes, or hazard assessment [*Field*, 2000]. Second, knowledge of the velocity structure beneath a seismic station assists in station corrections used in tomography, waveform modeling studies, and earthquake location problems. Third, the velocity structure may be translated into tectonic structures at shallow to intermediate depths.

Site response is normally determined in one of two ways. Using either receiver function analysis of teleseismic P-waves ($\Delta >30°$) or short period, local ($\Delta <150$ km) S waves, Figure 3.1. Both methods sample distinctly different portions of the crustal velocity structure. Teleseismic arrivals are relatively long-period P-waves, > 1 sec, and utilized in receiver function studies to determine crustal velocity profiles and thickness. At sharp interfaces teleseismic P waves convert a portion of their energy into S waves, which appears on the radial component. These P to S conversion are well-suited to crustal thickness studies, or determining Moho depths [*Langston*, 1977]. In contrast, teleseismic P waves do not perform well at determining shallow structure unless large velocity contrasts exist. Shallow velocity structures are well determined by local S waves. S waves cause the majority of damage during local earthquakes, and it is therefore appropriate to use local S waves to determine site response. Local S waves have frequencies from > 0.5 Hz to in excess of 7 Hz. Frequencies of

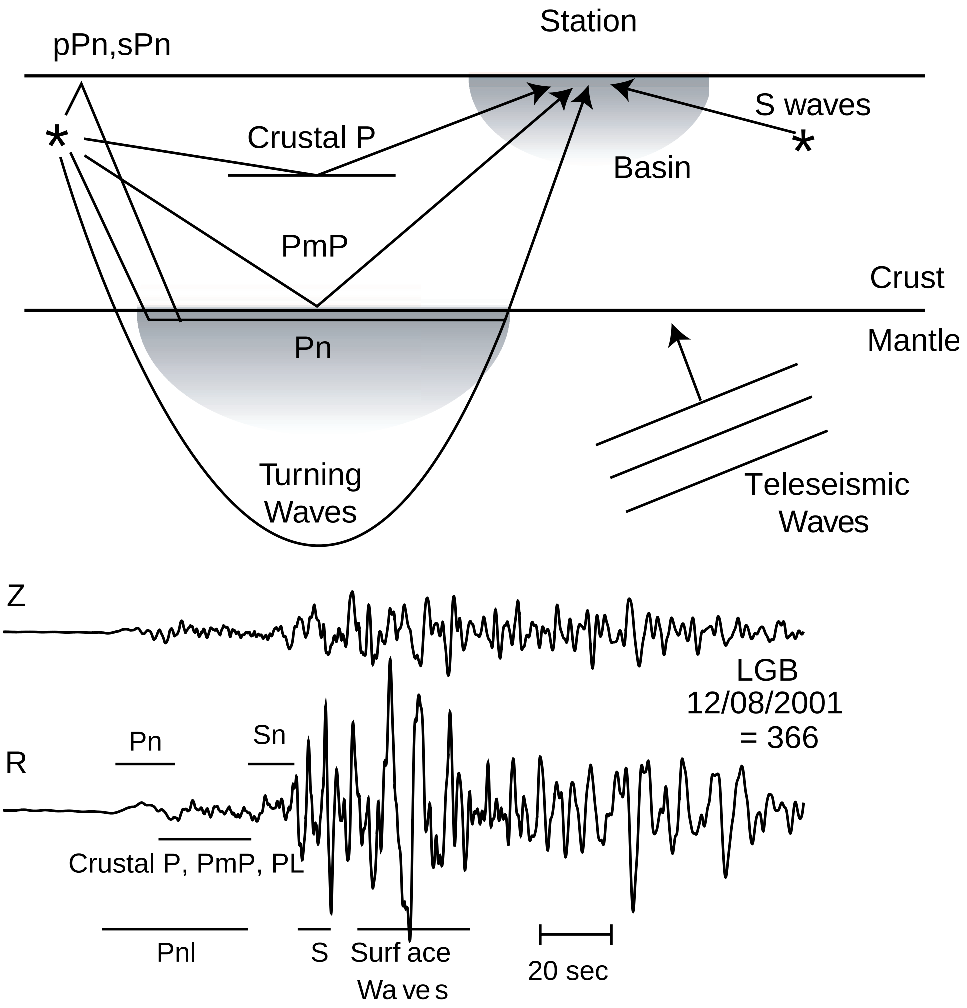

Figure 3.1: Cartoon of sampling and ray paths of many arrivals present in local and regional recordings of earthquakes, $\Delta < 14^o$. A teleseismic wavefield is also included. The inverted triangle is a seismic station located on top of a basin, shaded in gray near the surface. The stars are earthquake sources. The shaded region directly below the crust mantle interface indicates the sampling region of the Pn wavefield in the mantle. Below the cartoon are vertical and radial displacement data from an earthquake in southern California on 12/08/2001 recorded at station LGB (Laguna Bell). Portions of the waveform are highlighted for reference. The data are displayed on the same vertical scale.

this range limits the sampling to the top few kilometers, Figure 3.1. At very short distances the window used to compute the site-response contains the beginning portion of the surface wave. Surface waves are not solely representative of the local site response. Thus the velocity structure between source and receiver becomes increasingly important. This effect is overcome by a sufficient number of events and stations within a region [*Hough et al.*, 2003]. Another complication with using local S waves is the need of a nearby reference station of known site-response to calibrate the new response. This becomes important in the presence of basins or other complicated crustal structures [*Hartzell et al.*, 1998].

To compliment the use of teleseismic and local arrivals we suggest the use of regional P waves ($150 < \Delta < 1400 km$). These arrivals are refractions along the crust-mantle interface, Pn, and the crustal P arrivals and PmP along with various S segments. For convenience we identify this set of arrivals as Pnl[*Helmberger and Engen*, 1980]. Figure 3.1 shows the sampling region of Pn, Pg, and PmP from ray path and waveform perspectives. Pnl arrivals vary in frequency content from the longer-period Pn (0.33 Hz) to the shorter period Pg and PmP arrivals (0.5-2 Hz). This frequency range allows Pnl to be used to determine larger scale local structures that are not easily accessible to local S or teleseismic arrivals. Figure 3.1 displays vertical and radial component displacement records from an earthquake in 12/08/2001 recorded by station LGB, which is situated within the Los Angeles basin. Arrivals discussed previously are highlighted on the radial component as an example of their shape and timing from a waveform perspective.

3.2 Method

The angle of the wavefront, i, is affected only by the velocity of the medium, α, as the ray parameter, p, is constant in a simple layered structure.

$$p = \frac{\sin i}{\alpha} \tag{3.1}$$

As a wavefront encounters slower velocities its direction becomes increasingly vertical when arriving at a station. Figure 3.2 shows the waveforms differences between two velocity models. The first model emulates a “Hard Rock” station (V_p $5km/s$; 2 km deep) while the second is similar to a “Soft Rock” station (V_p $2km/s$; 2 km deep). The crust-mantle interface for both models is set at 35 km, the source receiver distance is 175 km, and the source depth is set at 17 km. This geometry makes Pn the first arrival at slightly further than critical distance. All waveforms on each row are plotted on the same amplitude scale. Moreover, the top three rows are on the same amplitude scale. Displacement generalized ray responses [*Helmberger*, 1983] were computed for Pn+PmP arrivals and the P to S conversion response near the surface, shown in the first two rows. These responses are then summed and filtered to produce the waveforms in the fourth row. When the ray paths becomes vertical, an increasingly larger proportion of energy will appear on vertical component, as P is polarized along the propagation direction. This effect is opposite for S waves where the polarization is perpendicular to the propagation direction. As the S wave encounters slower velocities, it turns vertical and the energy appears on the radial component. This effect is shown in the waveforms and in the polarization angle graphs between rows two and three. Recent studies use the polarization of S waves as a theoretical basis to do single station estimates of site amplification *Nakamura* [1989]; *Lermo and Chavezgarcia* [1993]; *Siddiqqi and Atkinson* [2002].

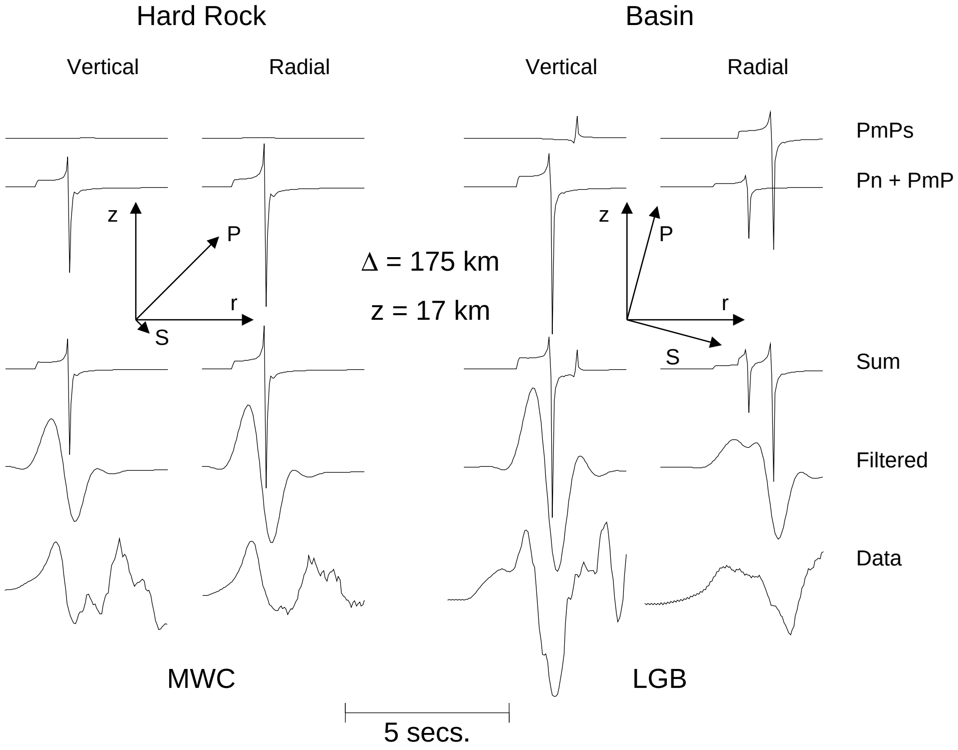

Figure 3.2: Comparison of seismograms from two different types of upper crustal velocity models. The left two columns are created from a "Hard Rock" type model and show the vertical and radial component. The right two columns are the vertical and radial components for a "Soft Rock" type model. The individual generalized ray responses in the top two rows are summed in the third row, then filtered in the fourth row. Each seismogram is made up of a single Moho reflection plus the P to S conversion at a 2 km deep boundary. "Hard Rock" seismograms look similar on the vertical and radial components. In contrast, "Soft Rock" seismograms have different shapes due to the increased vertical ray paths and the P to S wave conversion at depth. The P to S wave conversion widens the arrival on the radial component. The crust-mantle interface is set a 35 km depth, the source, z, is at 17 km, and the source receiver distance is 175 km.

Similar to teleseismic arrivals, *Pnl* arrivals convert P energy to S energy at interfaces. Larger contrasts amplify the conversion resulting in larger S arrivals. Synthetics for the "Soft Rock" model in Figure 3.2 show this. Converted P to S energy, as with local S waves, appears on the horizontal component. The combination of arriving P and S energy on the radial component results in an apparent longer period arrival when compared to the same arrivals on the vertical component. The radial appears longer period as the S wave has opposite polarities on the vertical and radial component in addition to the substantial S wave amplification occurring from large velocity contrasts. When these arrivals are filtered, either by a low pass filter or source effect, the apparent period of the radial increases relative to the vertical component.

The bottom row of seismograms in Figure 3.2 displays data from a "Hard Rock" and a "Soft Rock" stations. The amplitude and shape of the "Hard Rock" vertical and radial components are similar, indicating the *Pnl* arrival is arriving as a coherent wave packet. In contrast, the "Soft Rock" components show differences between the radial and vertical components. The radial component decreases in amplitude and becomes longer period while the vertical component is larger in amplitude and shorter period. This waveform behavior will be exploited to determine the amplification at a specific site.

Using the propagation effects highlighted in Figure 3.2 as a basis, we employ a vertical to radial energy ratio to determine the amplification of incident, extended P-waves at a broadband station. We use a record duration around the *Pn* arrival of 10 seconds before, t_0, and about 35 seconds after, t_1. We assume the initial portion of the *Pnl* arrival travels with a velocity of 7.8 km/s, which is average for southern California [*Hadley and Kanamori*, 1977] and many parts of the world. From this velocity and the source-receiver distance a *Pnl* onset time is calculated and used as the reference time. Use of this time window limits the arriving energy to be compressional (P) and associated S conversions near the receiver, rather the heavily S dominated energy later in the *Pnl* arrival. This relative high phas-velocity We then take a ratio of the vertical to radial energy to determine the amplification.

$$A = E^{1/2} = \left(\left[\frac{\int_{t_0}^{t_1} [v_z^2]_{\omega_1}}{\int_{t_0}^{t_1} [v_z^2]_{\omega_2}} \right] \Big/ \left[\frac{\int_{t_0}^{t_1} [v_r^2]_{\omega_1}}{\int_{t_0}^{t_1} [v_r^2]_{\omega_2}} \right] \right)^{1/2} \tag{3.2}$$

The vertical and radial velocity components are v_z and v_r, respectively. We square each waveform within the window specified above then integrate to obtain the energy for each record. This procedure is carried out for a variety of different frequencies. We use a low-pass, a-causal, butterworth filter at a range of various frequencies. By dividing the higher frequency energy, ω_1, by one at a lower frequency, ω_2 we obtain the amount of energy arriving within a specific period band. Division of the vertical component by the radial component removes any source and propagation effects. Amplification of *Pnl* arrivals occur on the vertical component as the ray direction turns more vertical upon encountering slower velocities near the station. We do not use a reference station, but rather assume that the reference amplification is around 1. This is shown later to be a safe assumption as the minimum value obtained from full waveform synthetics and data waveforms is approximately 1 for "Hard Rock" models.

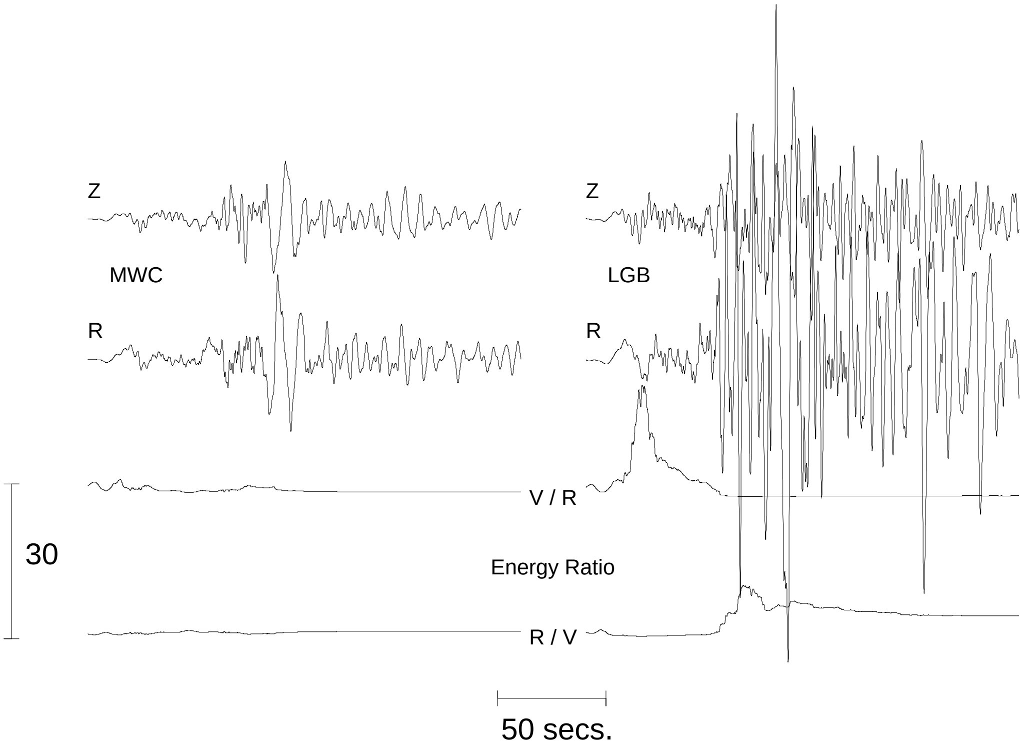

Figure 3.3: Effect of window duration, t_0 to t_1, on energy ratio. The top two rows are vertical and radial displacement records for stations MWC (Mount Wilson) and LGB (Laguna Bell). All records are on the same vertical scale. The bottom two rows show the energy ratio (V/R) and its inverse (R/V). As the measure leaves the Pnl regime and enters the S and Surface wave regime the first ratio descends towards 1 while the second increases due to the large amount of arriving horizontal energy. The lower frequency employed here is 0.1 Hz and the higher frequency is 3.0 Hz. These energy ratios assume an initial starting time of t_0 before the first arrival and the value of the energy ratio for any particular t_1 is the value shown at that particular time, i.e., no integration is necessary.

Figure 3.3 displays displacement data and two energy ratios versus time (V/R and R/V). We have set the lower frequency to be 0.1 Hz and the higher frequency to be 3 Hz. Concerning the first ratio (V/R) at station MWC, a “Hard Rock” site, the energy ratio stays near 1. This is in contrast to station LGB, a “Soft Rock” site, whose energy ratio becomes almost 30. As the time enters the *Pnl* regime the energy ratio grows governed by the phenomena highlighted in Figure 3.2. Leaving the *Pnl* regime and encountering the S wave and surface wave the energy ratio drops. This decrease is due to large amounts of arriving horizontal energy. Therefore the energy ratio measure is sensitive to the choice of integral duration, t_0 to t_1. We suggest taking the maximum value of the measure constrained within the *Pnl* regime, however using a set window length will only affect results if the duration is too long. The opposite effect is apparent for the second energy ratio (R/V). The ratio is nearly one through the arrival of *Pnl* . When the S waves begin to arrive the ratio of radial to vertical, as proposed by *Nakamura* [1989], increases until reaching a stable value during the surface waves. Moreover, a comparison of this ratio at MWC and LGB shows a pronounced amplification at the Soft Rock station LGB.

To test this, we calculated frequency wavenumber (FK) synthetics for a range of velocities, ±15% and layer thicknesses, $\pm 3km$, of the top layer. These synthetics are computed from a flat-layered model with the same velocity structure at the source and receiver. Taking a ratio of energies allows the removal of source side effects negating the one-dimensionality of our model. Our synthetic model is equivalent to the amplification at the middle of a large basin with flat, homogeneous layers. The synthetic model setup places both source and receiver within the slow velocities, similar to the middle of a very large basin. We expect increased amplification near basin edges due to a focusing effect [*Scrivner and Helmberger*, 1994]. As the velocities of the layer becomes slower the amplification of *Pnl* increases. The maximum amplification we see for the window length defined in Equation 3.2) is 3.9 with the minimum near 1. The correlation of amplification with layer thickness is not as strong as with velocity, especially at higher frequencies.

3.3 Data and Analysis

To compute amplification factors for southern California we employed broadband velocity records recorded by TriNet. These records have flat and stable instrument responses in the frequency range of interest. The instrument responses are removed as not to bias one station to another. Using only the regional records greater than 175 km allows us to capture only the *Pnl* arrival. Amplitude ratios, or the square root of the energy ratios, are computed for an event (12/08/2001 Northern Mexico M_w 5.8) and plotted in Figure 3.4 for all of southern California (top panel) and centered on the Los Angeles basin region (lower panels). The left lower panel of Figure 3.4 displays the topography and the measured amplitude ratios at individual broadband stations. On the lower right of Figure 3.4 is the interpolation of the amplitude ratio data. The results for this event agree well with other amplification studies *Hartzell et al.* [1998]; *Hough et al.* [2003]. Note the largest amplification appear in the regions with the deepest basins. However, larger than expected amplification factors are seen to the northwest and southeast of the deepest portion of the basin, below stations USC, OLI, and BRE. These areas are influenced by the basin edge. While this is not a true representation of amplification from a 1-D velocity structure, it does show the variability which may occur from regional earthquakes. This effect is similar to to surface wave contamination of local S wave estimates of amplification. However, computation of finite difference synthetics also show increased amplification near the edges of basins, i.e. *Scrivner and Helmberger* [1994].

We have not calibrated our amplification factors against those derived from local S-waves, due to the large number of source receiver pairs required. It does appear, however, that amplifications from this study do agree well in spatial pattern and reasonably in absolute magnitude. It is further encouraging that our minimum is near one and our maximum amplification is near the local S-wave maximum, both similar to our synthetic model mentioned previously.

3.4 Conclusions

Through the use of a *Pnl* ratio of vertical to radial energy we are able to quantify the effects of site response. An amplification factor is computed which is similar to local, high frequency S waves. In contrast to S waves, the *Pnl* ratio senses deeper into the crust. This method is particularly suited for discriminating the edges of large basins which can be hazardous during medium to large earthquakes. Further work is necessary to determine if basin structures can be mapped through these methods. This method can be used in conjunction with local S waves and teleseismic P waves to further constrain site response.

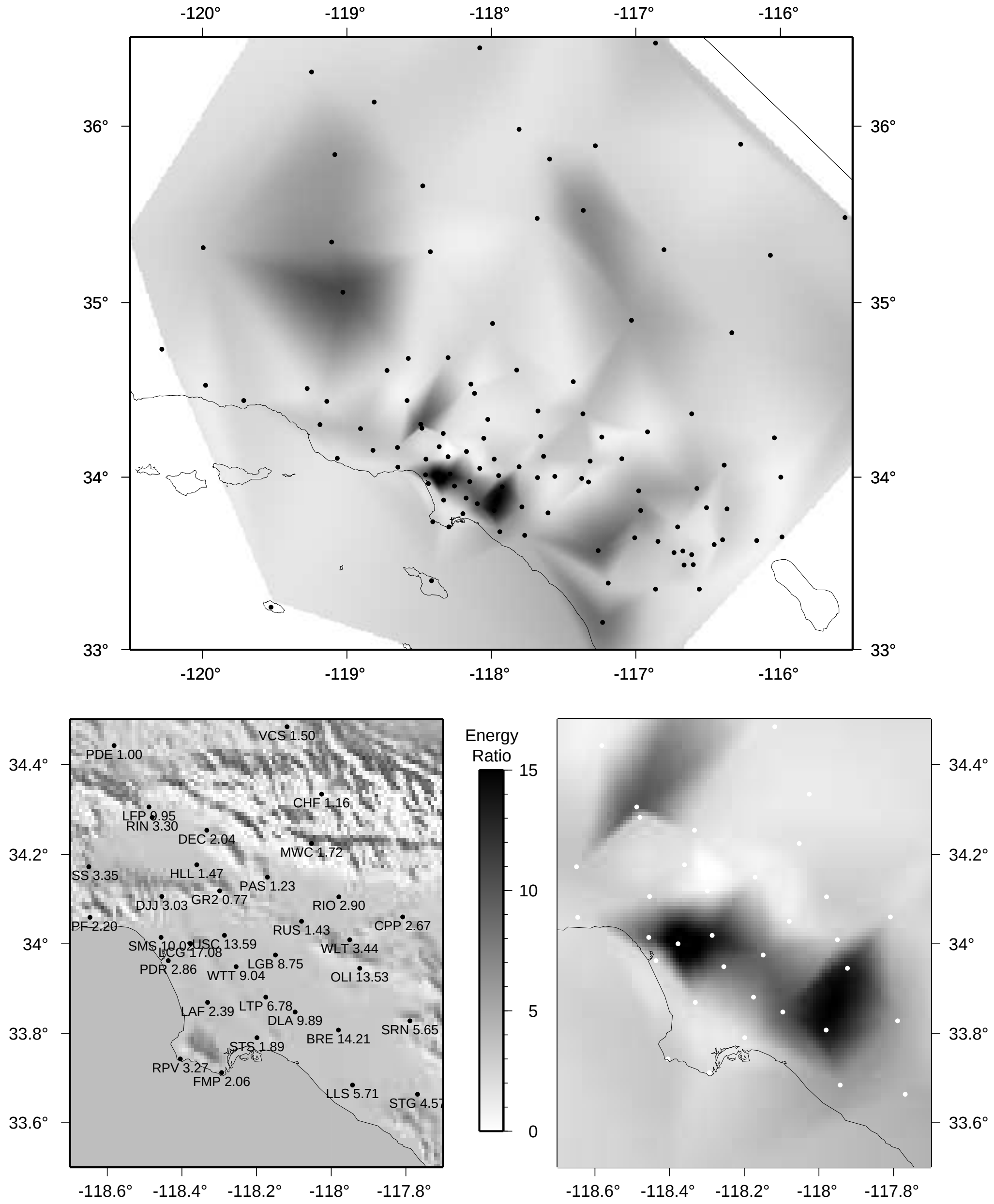

Figure 3.4: Map of amplification factors for southern California and the Los Angeles basin region using a low frequency of 0.1 Hz, a high frequency of 3.0 Hz, a t_0 of 10 seconds before *Pnl* (7.8 km/s), and a t_1 of 35 seconds following. Left panel shows topography and amplification factors. Right panel shows the interpolated grid using the data in the left panel. Areas to the northwest and southeast show increased amplification than to the center of the Los Angeles basin due to basin edge effects [*Scrivner and Helmberger*, 1994]. Points represent broadband seismic stations with names and amplifications following. The darker the shading the larger the amplification.

Acknowledgements

This research was supported by by United States Geological Survey under Grant 02HQGR0063. The authors would like to thank Hiroo Kanamori for helpful discussions. This is Contribution No. 8954, Division of Geological and Planetary Sciences, California Institute of Technology.

Chapter 4

Complex Rayleigh Waves in Deep Sedimentary Basins

4.1 Introduction

The Salton Trough crosses the border between Baja California, Mexico, and California, USA, and forms a transition zone between extension and strike-slip motion on the Pacific-North America plate boundary (see Figure 4.1). This zone trends northwest-southeast and is bound by faults to the east and west. In the trough a deep sedimentary basin *Fuis et al.* [1984] overlies a shallow Moho discontinuity [*Zhu and Kanamori*, 2000; *Fuis et al.*, 1984; *Lewis et al.*, 2000, 2001; *Ichinose et al.*, 1996]. It is believed that in this area a combination of strike-slip and extensional motion has thinned the crust from above and below. A lack of local instrumentation has left questions about recent tectonics in northern Baja California and the gulf of California. Earthquakes originating in this region will produce complex waveform data illuminating some of the tectonic structures. In late 2001 and early 2002, two separate earthquakes in this region produced double surface waves, previously unreported. We will attempt to identify the type of velocity structure required to produce these complex surface waves.

4.2 Data

Two earthquakes in northern Baja California were recorded by TriNet stations in southern California. Figure 4.1 displays the location of these earthquakes and their double-couple solutions (Table 4.1) with seismic stations plotted as triangles. Both earthquakes occurred near the western edge of the Salton Trough, on or near the Cerro Prieto fault. Near the

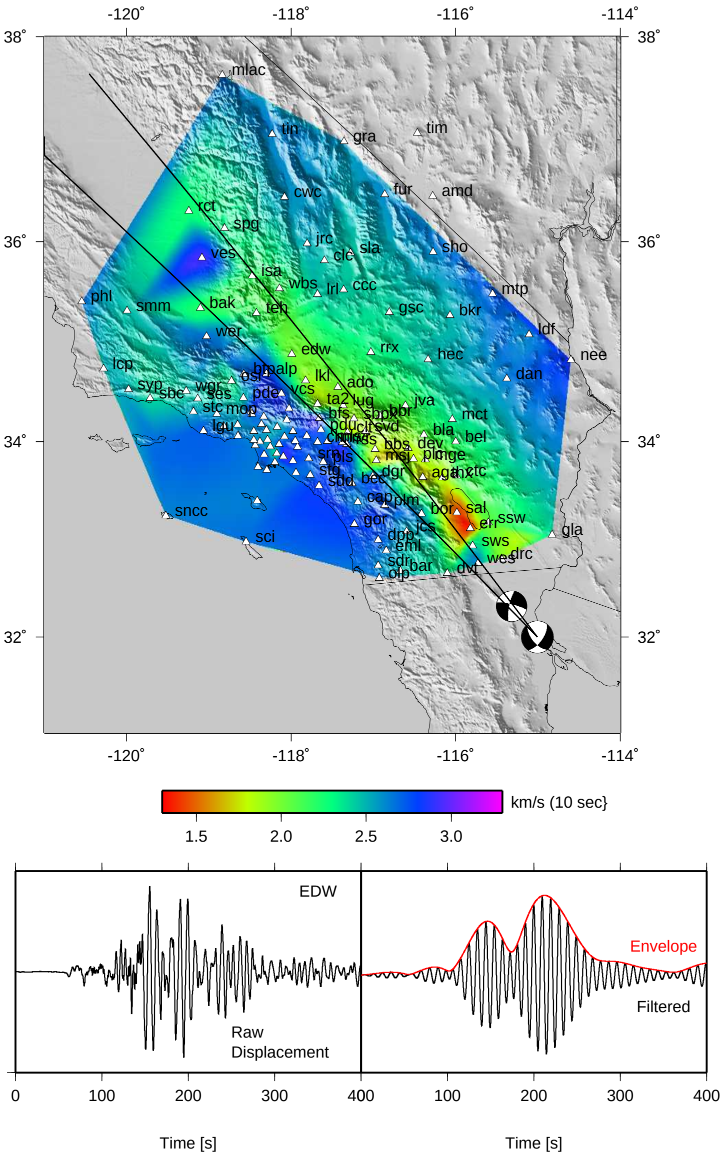

Figure 4.1: Map of southern California with TriNet stations plotted as triangles and the two studied earthquakes in northern Mexico. The top panel displays an interpolated velocity image for a surface wave, Rayleigh wave, of 10 seconds period for the southern-most event. The lower panels detail how this measurement was made. The raw data, left lower panel, is narrowly bandpassed to produce the lower right panel. An envelope of the filtered signal is then taken and the maximum amplitude of the envelope is used for a velocity measurement. Two pulses appear on the lower right figure. This second arrival results in the low velocity swath of data emanating from the Salton Trough, upper panel. Two lines from the southern most source are azimuths of 316 and 323 degrees, used in later discussions.

Mexican-U.S. border, the western boundary of the Salton Trough is know to be an abrupt transition between a very deep sedimentary basin on the east and a shallow to almost non-existent basin on the west *Fuis et al.* [1984]. Limited seismic recordings and lack of a high-quality velocity structure in the area places the reported hypocenters into question, most notably the depth. We will first describe the recorded Love and Rayleigh waves and follow with an explanation of the characteristics of the crustal velocity model required to produce the recorded features in the data.

Table 4.1: Earthquake Source Parameters

Date Time	Longitude Latitude	Moment [dyne-cm]	Depth [km]	Strike [deg]	Dip [deg]	Rake [deg]	Source
2001/12/08	-115.002	6.68e24	8	142/35	59/64	-149/324	Harvard[α]
23:36:10.11	31.9977	5.79 M_w					
2002/02/22	-115.322	2.73e24	8	204/113	78/87	3/167	USGS[β]
19:32:41.75	39.3188	5.54 M_w					

[α] Harvard Centoid Moment Tensor
[β] USGS Rapid Moment Tensor Solution

Figure 4.1 highlights the difficultly of using data from this region. The top panel displays the velocity of a surface wave of 10 seconds period from the southern-most event. Measurements were made by narrowly bandpassing the raw data, taking the envelope, and using the timing of the maximum amplitude to determine a velocity, as shown in the lower panels of Figure 4.1. In a narrow swath, a much slower velocity arrival dominates the waveform data at 10 seconds period. The arrival results in an much slower than expected velocity determination thus contaminating a swath of data emanating from the Salton Trough.

Figure 4.2a displays a record section of raw, broadband displacement data recorded from the southern most event, 2001/12/08. Figure 4.2b shows the same data but filtered with a low pass butterworth filter at $0.15Hz$. The event of 2002/02/22 shows similar features. The data is plotted with a reduction velocity of 3.2 km/sec to align the Rayleigh and Love waves. The first two columns show tangential displacement waveform data for azimuths less than 323^o (column 1), along the western edge of the Salton Trough, and azimuths between 323^o and 316^o (column 2). The right two columns are vertical displacement waveform data for the same azimuths as columns 1 and 2.

4.2.1 Love Wave

The tangential displacements in column 1 of Figure 4.2 show an initial large amplitude, long period arrival, $\Delta < 300km$. This arrival, consisting of lower crustal S waves based on generalized ray modeling [*Helmberger*, 1983], in the absence of extended coda suggests the S

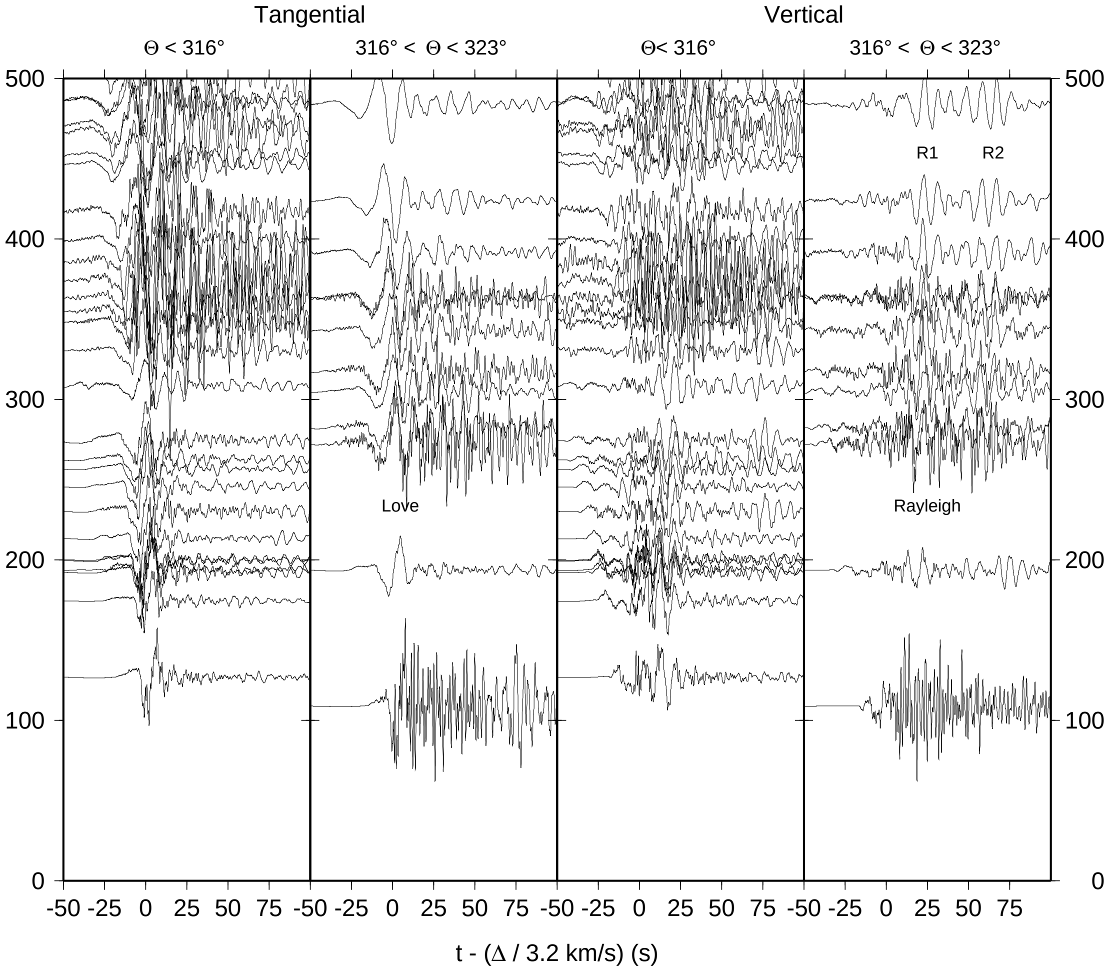

Figure 4.2: Four record sections of data recorded from the event on 2001/12/08. The left two columns are record sections of tangential displacement data recorded at stations with azimuths less than 323^o and between 316^o and 323^o, respectively. The right two columns display vertical displacement data for the same azimuthal swaths. The reduction velocity is 3.2 km/sec. Part a) is displayed without a filter and part b) is the same data low-passed at $0.15 Hz$.

waves propagated through relatively basin free crust. Moreover, long period Love waves are difficult to identify on these records. Tangential displacements in column 1, $\Delta > 300km$, encounter the Los Angeles basin. The large long period pulse is still present but is now trailed by higher frequency coda. These higher frequency arrivals are a result of the seismic waves interacting with the basin edge and the slow Los Angeles basin velocities [*Scrivner and Helmberger*, 1994].

Tangential displacements in column 2 show similar as well as dissimilar features when compared to column 1. Again, the large amplitude, long period, S waves are the first signals to arrive. S waves at distances less than $150km$ in column 2 have propagated entirely within the Salton Trough. This path contains a very deep sedimentary basin [*Fuis et al.*, 1984]. The deep, slow velocities near the surface trap energy, creating extended coda of both low and high frequencies. The S wave arrival is equal in amplitude to, or in some cases slightly smaller than, later arriving coda. As the S waves leave the Salton Trough at the northern edge the extended coda, dominated by the higher frequencies, disappears. The removal of higher frequencies can be seen by comparing the waveform at $110km$ with one at $190km$ or past $400km$. Those waveforms near $250km$ are interacting with the edge of the basin near the northern extent of the Salton Trough.

4.2.2 Rayleigh Wave

The Rayleigh waves in columns 3 and 4 of Figure 4.2 are distinctly different than the Love waves. Those west of azimuth 316^o, shown in column 3, show a single Rayleigh wave. Column 4, azimuths 323^o - 316^o, shows a long period, large amplitude signal, R1, similar to those seen in column 3, followed by another long period signal 20 to 40 seconds later, R2. The appearance of R2 is abrupt when crossing an azimuth of 316^o. There are some exceptions. In column 3, arrivals at 75 seconds are visible, but do not have the same amplitude or station to station coherence when compared to those in column 4. Further to the east, azimuths $> 323^o$, R2 is not present or is much smaller in amplitude than R1 (not shown). Between azimuths 323^o - 316^o the amplitude of R2 is from 50 to 100% of that of R1 at all stations within this corridor. Plotting the particle motion in the vertical-radial plane for R1 and R2, Figure 4.3, shows both are retrograde circular and therefore we conclude both to be Rayleigh waves. The data and synthetics in Figure 4.3 are low passed at $0.3Hz$. Later, we will perform the same analysis on synthetic waveforms to confirm that these are Rayleigh waves. The first Rayleigh wave, R1, contains slightly longer periods ($>$ 12 seconds) than the second, R2. At distances greater than 200 km, where R1 and R2 are easily identified, the arrival time difference of the maximum amplitude of envelopes from R1 to R2 does not change. The extended coda of Salton Trough stations at $\Delta < 200km$ makes it difficult to identify the R2-R1 separation. The identification of multiple surface waves was previously reported by *Ho-Liu and Helmberger* [1989] for Love waves with earthquake sources in the same region.

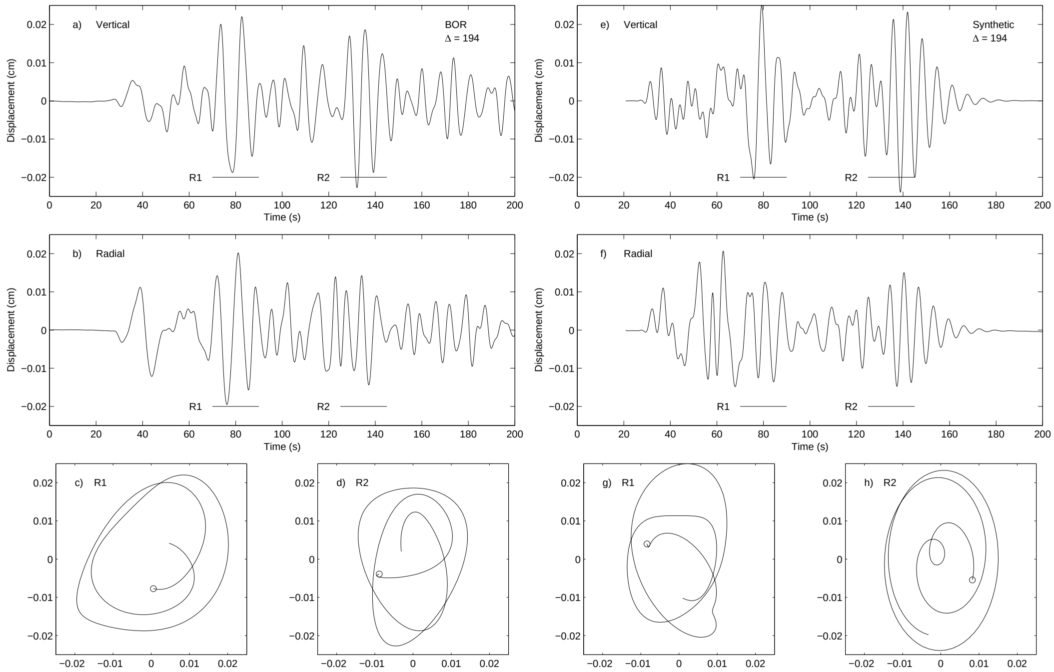

Figure 4.3: Data and synthetic displacement seismograms at station BOR, $\Delta = 194km$. Panels a) and b) are the vertical and radial displacement for station BOR. Panels c) and d) are vertical-radial particle motion plots for R1 and R2, for the sections of the underlined waveforms in a) and b). The circle in c) and d) denotes the start time in the panel. Panels e) and f) display the synthetics corresponding to those in panels a) and b) computed using a frequency wavenumber integration scheme [*Saikia*, 1994]. Panels g) and h) show the vertical-radial particle motions for the synthetics. Data and synthetics are filtered with a low pass butterworth filter at $0.3Hz$.

4.3 Modeling

Using the clear absence of a Love wave arrival at all stations, we can first determine a minimum earthquake depth. Using either the standard Southern California model [*Hadley and Kanamori*, 1977], SSC, or a Salton Trough model, ST, *Ho-Liu and Helmberger* [1989] and *Fuis et al.* [1984] (Tables 4.2 and 4.3) we can constrain the earthquake source depth to be greater than 6 km. Both models produce rapidly decaying Love wave amplitudes as the earthquake source depth increases past 6 km, synthetics not shown.

Table 4.2: Salton Trough Velocity Model

Z $[km]$	V_p $[km/s]$	V_s $[km/s]$	$[g/cm^3]$
5.6	3.46	2.00	2.10
10.4	6.30	3.64	2.67
19.0	6.70	3.87	2.80
Half Space	7.80	4.50	3.00

Table 4.3: Standard Southern California Velocity Model

Z $[km]$	V_p $[km/s]$	V_s $[km/s]$	Density $[g/cm^3]$
5.5	5.50	3.18	2.40
10.5	6.30	3.64	2.67
19.0	6.70	3.87	2.80
Half Space	7.80	4.50	3.30

Figure 4.4, the left column, displays the variation in synthetic vertical displacement as the source depth is varied and the velocity model is held fixed. The synthetics shown here are broadband. Placing the source depth at 8 km and using the ST model we are able to produce the same characteristics of R1 and R2 as seen in the data. Synthetic displacement seismograms were created using a frequency wavenumber integration technique [*Saikia*, 1994]. We are not attempting to explain all arrivals but want to isolate which features of the model are most sensitive to the production of separate Rayleigh waves, R1 and R2. Both synthetic R1 and R2 arrivals are identified as Rayleigh waves from the particle motions in Figure 4.3. Like the data, the synthetic displacement also show circular to elliptical particle motion.

The sensitivity of source depth on R1 and R2 production is examined in Figure 4.4, left column. At shallower depths, the isolation of R1 and R2 becomes more pronounced, especially when the source is contained within the slow velocity basin, 3 and 5 km. As the source position deepens, R1 and R2 persist as isolated phases until approximately a source depth of 10 km. At 10 km source depth, long period energy appears between R1 and R2. As the source deepens further, the amplitude of R1 and R2 decreases, with R2 having a more rapid decrease. R2, for the ST model, is indistinguishable from the long period coda of R1 at depths of 14 km and greater. The Rayleigh wave data in Figure 4.2 shows isolated R1 and R2 pulses, thus we can constrain the source depth to be between the basin bottom, 6 km, and a depth of 10 km.

With the depth constrained we can address which portions of the model are most sensitive to the production of R1 and R2. These sensitivity tests will also provide insight into the origin of R1 and R2. Modifications to the mantle half-space and lower crust in velocity and layer thickness had no effect upon the Rayleigh and Love waves. These modifications do shift the arrivals of Pn, Sn and crustal P arrivals which spend most of the propagation time in these deeper layers.

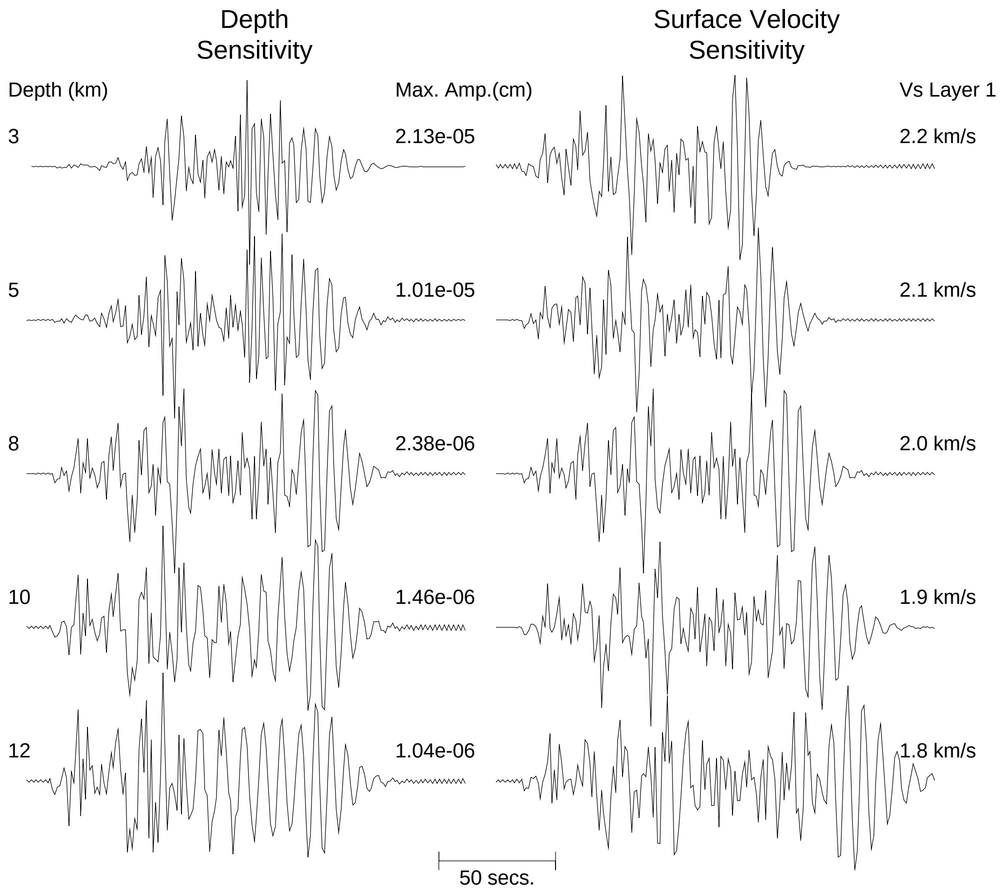

Figure 4.4: Sensitivity of vertical synthetic displacement to source depth, left column, and top layer velocity, right column. The source receiver distance is $200km$. The source depth is held fixed at 8 km when varying the top layer velocity. No filtering is done to the synthetics.

Changes to the upper crustal layers produce dramatic effects on all portions of the waveform, see Figure 4.4 column 2. An increase in velocity (5%) of either the source layer or basin layer advanced R1 in time, while a similar decrease in velocity had the opposite effect. This change in velocity had little effect on the shape of R1 except for the addition of a few more oscillations at the end of R1. The effect on R2 is more substantial, as can be seen in column 2 Figure 4.4. Increasing or decreasing the basin layer velocity shifted the arrival of R2 in the same direction as R1 but 3 times larger for the same percent change. The duration of R2 is very sensitive to the top layer velocity. The slower the velocity the more numerous the oscillations, even at long periods ($> 10s$). In contrast, an increase of velocity in the source layer delayed the R2 arrival and increased the duration of R2. The opposite occurred for a decrease in velocity. It appears the source layer is controlling the timing of R1 while the basin layer determines the shape of R1. Moreover, the top basin layer is controlling the arrival time and shape of R2.

Modifications of the layer thicknesses also affect the timing and shape of the R1 and R2. Again, the lower crust and mantle half-space do not play a significant role. The thickness of the source layer only affects the waveform shape and amplitude of the very beginning of the long period surface wave. The basin thickness is the only parameter which produces significant modifications to the surface waves. As the basin is thickened, R2 becomes more isolated and longer periods are added. As the basin is thinned, R2 loses longer period signals and eventually disappears. This effect is due to the long period arrivals sampling a large vertical section of crust and being directly influenced by the velocity profile. If we place slower velocities at deeper depths we will delay the longer periods. The opposite effect is achieved by placing higher velocities at these depths resulting in the longer period arrivals being much faster. Gradients and higher velocities near the bottom of the basin have a similar effect to decreasing the basin depth, only muted.

4.4 Discussion

From these sensitivity tests, three main factors are controlling the production of a secondary Rayleigh wave, R2; 1) the depth of the basin, 2) the velocity profile of the basin, and 3) the contrast of the basin velocities with those of the upper crust. To produce R2, a significantly deep basin with slow velocities extending to a depth greater than $5km$ is necessary. Attempts to add gradational structure to the basin bottom only degraded the isolation of R2. An increase of the thickness of the basin layer by a few kilometers is not inconceivable for this region. With a much thicker basin the velocity profile could contain gradients at the basin bottom while still allowing very slow velocities at great depths. In general, what is most important in the generation of R1 and R2 is the crustal velocity gradient with depth. The generation of R1 and R2 does not appear to be due to 2-D structure along the propagation path or 3-D structure perpendicular to the propagation path.

The data presented in Figure 4.2 shows two Rayleigh waves at constant time separation, $\Delta > 200km$. The 1-D model used above can create two isolated Rayleigh wave pulses but cannot keep the pulses at constant time separation. Using two distinct 1-D models connected at $200km$ creates the isolated Rayleigh wave pulses , and then keeps them at constant time separation. The second 1-D model, is only used to maintain constant time separation between R1 and R2, not in the generation of R1 and R2. The two models are the *Ho-Liu and Helmberger* [1989] ST basin model for $\Delta < 200km$ and the SSC model [*Hadley and Kanamori*, 1977] greater than 200 km. Vertical displacement synthetics and the velocity model from which they were generated are plotted in Figure 4.5. Synthetics displayed in Figure 4.5 are low passed at $0.3Hz$. The white star in Figure 4.5 is the earthquake source and the synthetics were created using the spectral element method [*Komatitsch and Tromp*, 1999]. All synthetics are plotted on the same amplitude which has been corrected for geometrical spreading by diving by the distance. Two Rayleigh wave are created at $\Delta < 200km$ in the deep, slow ST basin. Longer propagation times within the basin create a longer separation time between the Rayleigh wave pulses. As the isolated pulses pass the basin edge at 200 km they continue to propagate but now at a constant time separation. Each pulse acts as a new source at the basin edge and propagates according to the new velocity profile.

After leaving the slow velocities of the basin, R1 and R2 continue to propagate. The frequency dependence of R1 and R2 is similar to synthetic waveforms in the basin but much more pronounced. R1 is dominated by long periods with higher frequency non-Rayleigh waves superimposed. These higher frequency non-Rayleigh waves are created from the higher mode Rayleigh waves in the basin which lose their coherency after leaving the basin. R2 is more coherent outside of the basin but is constructed of shorter periods than R1.

The presence of multiple Rayleigh and/or Love waves may be further used as a depth discriminate. We have shown through observations and synthetic examples that two Rayleigh waves may be present at the same time as a solitary Love wave. This occurs when a source is deeper than the basin bottom but close to this boundary. If two Rayleigh waves are present with two Love waves, we may assume the source is contained within the basin sediments. These features used in conjunction with a comparison of surface wave and Pnl amplitudes will aide in constraining source depths, especially for events with limited observations, i.e. older events in the Salton Trough region.

Returning to Figure 4.2, many features in the data are not explained by our simple 2-D model. In column 3 of Figure 4.2 long period energy is arrives at 75 seconds but is inconsistent from waveform to waveform. Further, a similar feature is also seen in column 4 at 190 km. More differences between the synthetics and the data at 100 km in column 4.

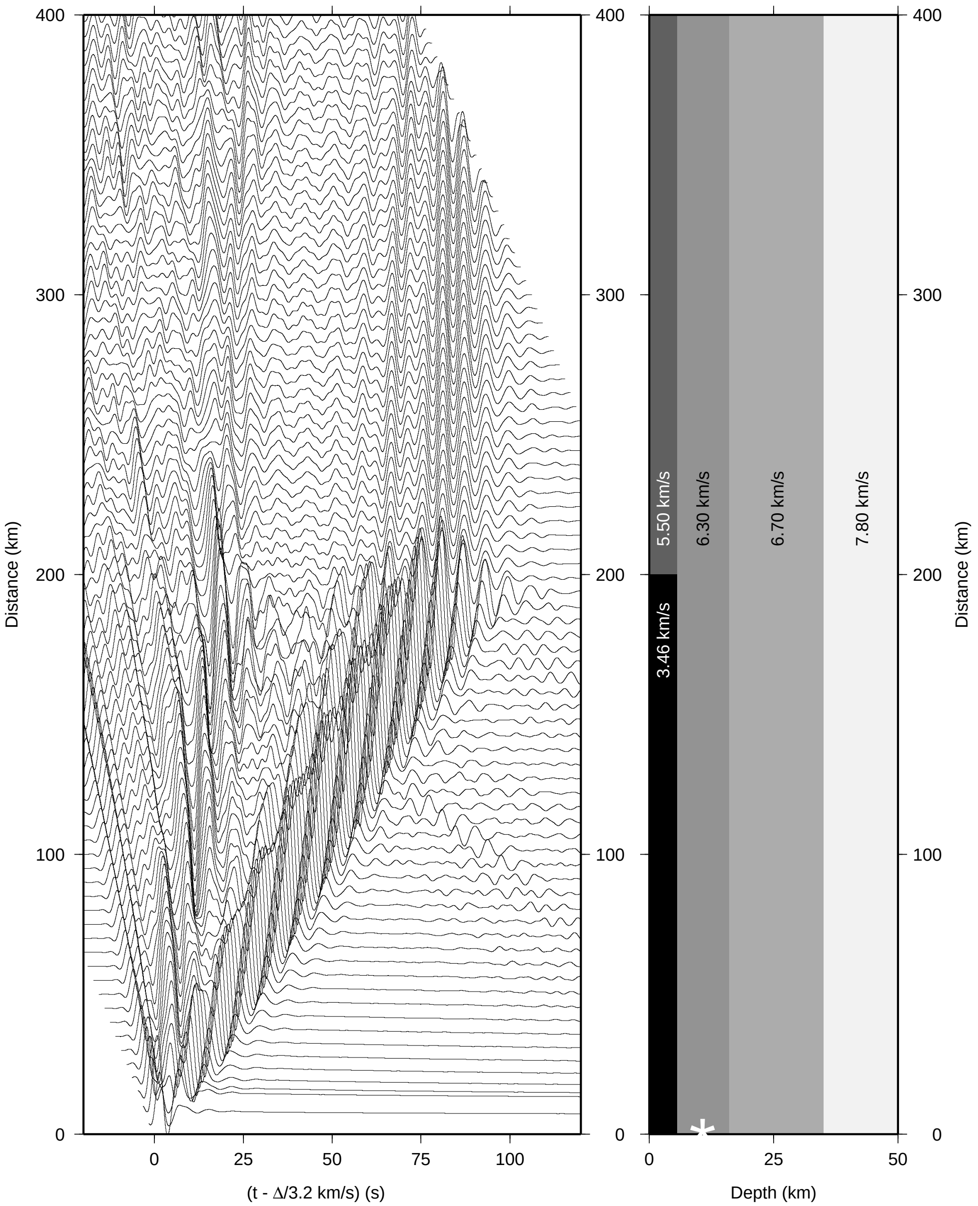

Figure 4.5: Simple 2-D velocity model and vertical displacement synthetic seismograms determined using that model by the spectral element method [*Komatitsch and Tromp*, 1999]. The waveforms are displayed as a record section. The reduction velocity is 3.2 km/sec. Notice that the time separation grows between R1 and R2 as the distance approaches $200km$ then is constant past $200km$. Synthetics are filtered with a low pass butterworth filter at $0.3Hz$.

Figure 4.5 shows a distinct separation between R1 and R2 at 100 km, but the data shows a solitary pulse. These unexplained features are likely due to velocity and basin shape differences when compared to our 2-D synthetic model. *Fuis et al.* [1984] showed the Salton

Trough to vary from east to west in basin depth and velocity, features not accounted for in our model.

The scale-lengths involved in this study are long enough to easily see the separated Rayleigh wave, and secondly, only one basin is apparently responsible. As the scale-lengths shift to short period, $> 1s$, we encounter "Lg" phases and increased coda levels in basins. The concept of "mini" basins then becomes an important source of duration enhancement, where each basin splits the Rayleigh waves and the combined response can last for several hundred oscillations at the higher frequencies, [*Kawase and Aki*, 1989; *Saikia et al.*, 1994]. In this case the particle motion is too complex to definitively label a scattered Rayleigh wave (R2).

4.5 Conclusions

To create a separation of the Rayleigh wave and produce R1 and R2 we need not embed the earthquake source within the slow velocity sedimentary basin, as reported for the Love wave [*Ho-Liu and Helmberger*, 1989]. We do need a significantly deep, low velocity basin to slow the propagation of long period energy, thus creating a separation of the two Rayleigh waves. The crust needs a substantial increase in velocity between the basin and underlying rock. After propagation within the basin, to keep the separation of R1 and R2 constant, the crustal velocity structure requires the removal of low velocities at greater depths in the crust. We did not need sophisticated 2-D, along path, or 3-D, path perpendicular, models to produce the separated Rayleigh waves, R1 and R2. We did implement a simple 2-D model to force the time separation of R1 and R2 to be constant.

The recognition of multiple Rayleigh wave is very important for seismic hazards and strong ground shaking. The extended wavetrain effectively increasing the duration of the shaking at long and short periods. This strong ground motion may occur in other large basins other than the Salton Trough. Examining waveforms from recent events shows similar features in the Los Angeles and San Fernando basins. While the same phenomena does exist at shorter periods, $> 1s$, it appears muted in long period expression. The time separation is smaller due to the size and velocities of the two major basins in Southern California.

Acknowledgements

The authors would like to thank Hiroo Kanamori and Vala Hjörleifsdóttir for their helpful discussions, Jascha Polet for a helpful review and Jeroen Tromp and the Theoretical Seismology Group at the California Institute of Technology for the use of the Spectral Element Code (SPECFEM3D) on their Beowulf cluster. We would also like to thank Vernon Cormier and two anonymous reviewers for their helpful comments. This research was supported by the United State Geological Survey Grant No. 02HQGR0062. Contribution 8952, Division of Geological and Planetary Science, California Institute of Technology, Pasadena, California.

Chapter 5

Sinking of the Kursk

5.1 Introduction

On August 12, 2000, two events were located in a seismically inactive region, less than 10 degrees from Novaya Zemlya, where a large number of nuclear tests were conducted over the decades. These events were located close together in the Barents Sea region at shallow depths, the latter measuring $m_b = 3.5$. Figure 5.1 shows the location of the larger event and stations used in the analysis. A few days after the events occurred, news agencies reported that a Russian submarine, the Kursk, had been damaged during exercises in the Barents Sea. The seismic events were located in the same region and at the same time as when the Kursk reportedly sunk.

The Kursk is a Russian nuclear submarine, Oscar II class, with the ability to carry 24 anti-ship cruise missiles. While the missiles can be nuclear in nature, 500 kilotons, it is more likely that those carried on the Kursk were a conventional explosive size of 750 kg (3/4 ton) *Bellona Foundation* [2000], as the nuclear warheads have been placed into storage. A single missile of this size, exploded underwater, is easily capable of generating seismic waves that can travel local distances. Given low attenuation, the same missiles can be detected regionally. While multiple missile explosions can generate energy which has the ability to travel much further. Being that the time and spatial extent of the events match those of the damaged Kursk, and that there was an explosive capability most likely present at the time of the events, leads us to the conclusion that the two events recorded seismically and the damage to the Kursk are related.

Our purpose is to get a better understanding of what happened on board the Kursk, in terms of the size of the explosions. A few techniques have been utilized to determine the size

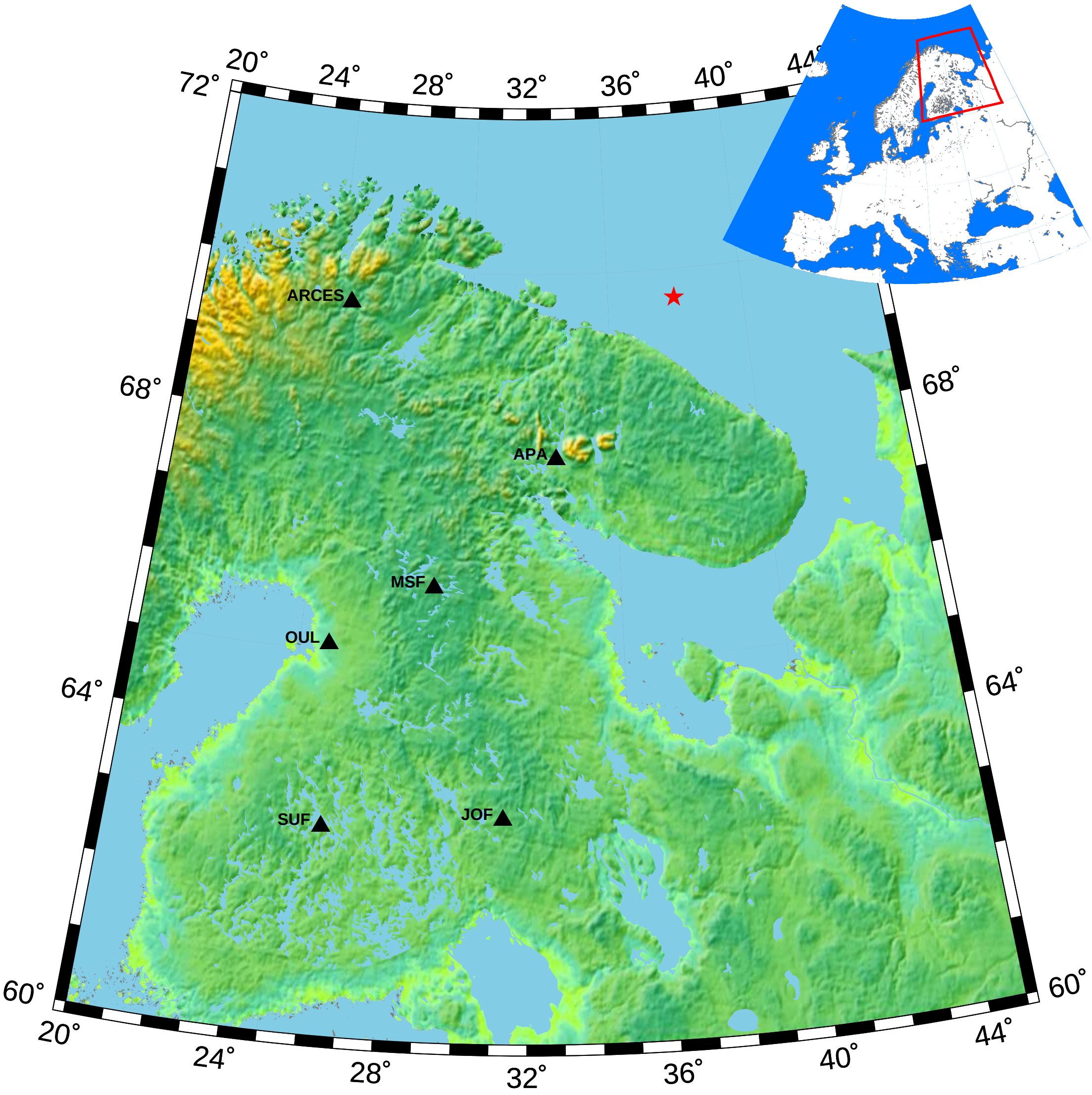

Figure 5.1: Map of the region surrounding the Kursk explosion, star, and stations, triangles, used in determining the explosion size.

of underwater explosions, which include using various magnitude scales or characteristics in the amplitude spectra [*Baumgardt and Der*, 1998] *Gitterman* [1994] *Gitterman et al.* [1998] *Koper et al.* [2001]. However, the approach taken here will be to use synthetic waveforms to understand more about the seismic signatures in the time domain. The observations (short-period, 0.2 - 20 Hz, vertical field) are displayed in Figure 5.2, plotted as a reduced section which aligns the Pn. We have included some reference lines to aid in the phase

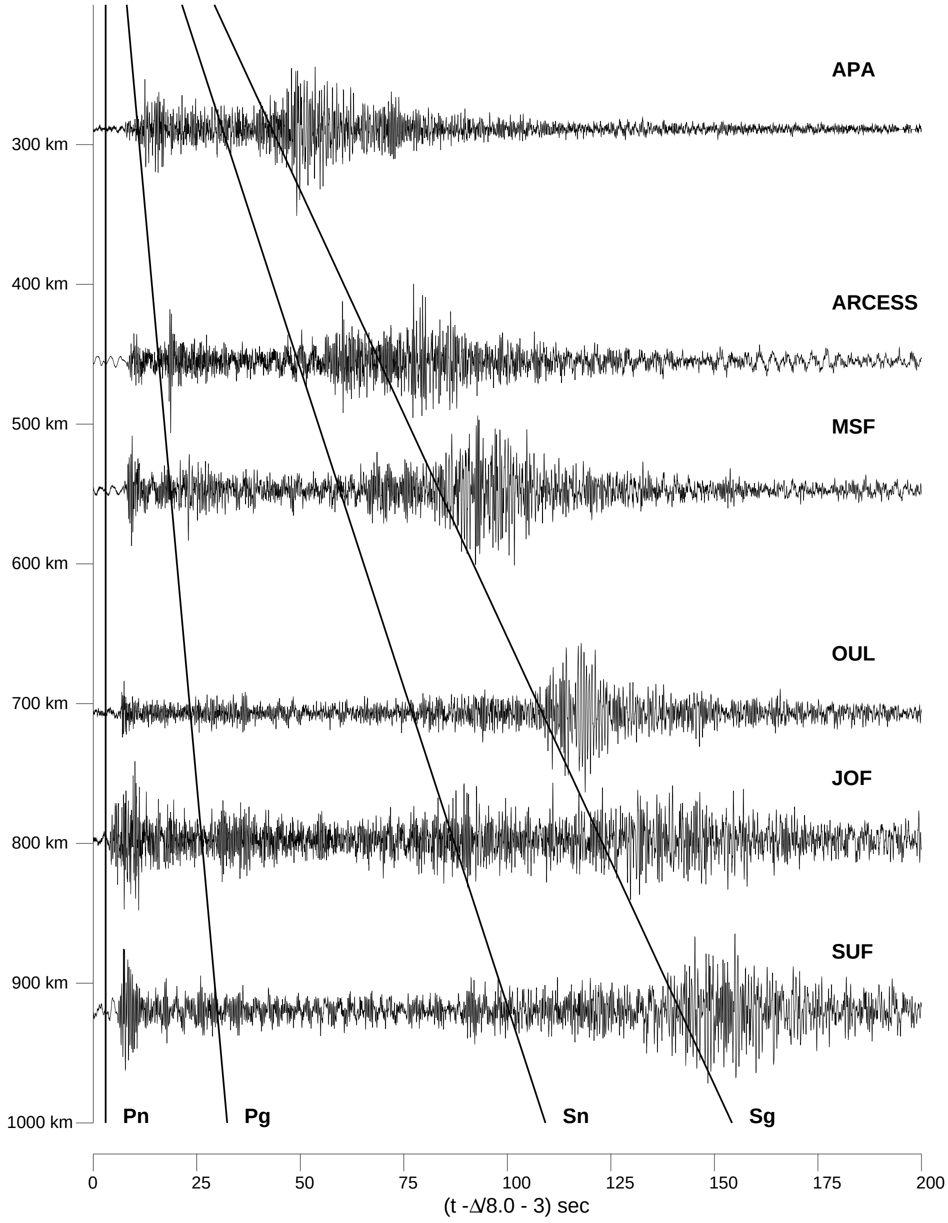

Figure 5.2: Short period, 0.2- 20 Hz, vertical data from stations shown in Figure 1. Note the relative similar amplitudes between P and S arrivals. Lines for theoretical arrival times of Pn(8.0 km/sec), Pg(6.7(km/sec), Sn(4.7 km/sec) and Sg(4.0 km/sec) are also shown for reference.

identification. Since we see frequencies at 3 Hz distances out over 900km, it is most likely the case that attenuation does not play a very important factor. Additionally, there is little to no apparent frequency shift as we proceed out in distance, reinforcing this point. Moreover, no large amplitude variation with azimuth is seen, as is characteristic of an explosion.

In this study, we will address the extended P-wave motions because most of our knowledge about crustal structure is for P-waves. A discussion of the relationship between P and S waves in our data will be reserved until later, as they are intimately related to the water in which they are produced. In order to compute synthetics for an underwater explosion, we will first characterize an underwater explosive source, and then describe seismic wave propagation within a water layer. Finally, we will compare the synthetics to the waveform data in an attempt to estimate explosion size.

5.2 Underwater Explosive Sources

Following the description in [*Weston*, 1960; *Arons*, 1954; *Cole*, 1948], the time dependence of pressure of an underwater explosion can be formulated. Note that a single explosion in water is comprised of a series of over-pressures and under-pressures caused by the pulsation of the gas volume in the water. Examples of the gas volume pulsation can bee seen in *Helmberger* [1968]. These over-pressures, or bubble pulses, essentially act as new sources and their relative amplitude is dependent on detonation depth and explosive yield. The relation between the peak pressure and the explosive yield for the first pulse is shown in *Weston* [1960] as

$$P_0 = 2.16 * 10^4 \left[\frac{Y_0^{1/3}}{r} \right]^{1.13}$$

where P_0 is in $dyne/cm^2$, Y_0 the yield is in pounds of T.N.T, and r, the distance from the source to the receiver, is in feet. The over-pressures decay as an exponential where the relaxation time of the initial pulse is defined by

$$t_0 = 1/\alpha = 58 Y_0^{1/3} \left[\frac{Y_0^{1/3}}{r} \right]^{0.22}$$

The under-pressures occur over a much greater time period and return the pressure of the region back to a hydrostatic level. As will be shown later, as the yield increases the effect of the later pulses on the final waveforms decreases dramatically. To simplify the calculation, only the first pulse will be used in the characterization of the source. Later, we will add the bubble pulses as secondary effects. The underwater source description, classically defined in units of pressure, needs to be redefined in units of displacement potential for synthetics to be computed.

Following the formulation of a simple source with no radiation pattern*Helmberger* [1983], we define the the pressure of the initial pulse by

$$P(t) = \frac{R_0}{R} P_0 e^{-\alpha(t-\frac{R}{c})} H(t - \frac{R}{c})$$

where P_0 and is the maximum pressure of the initial pulse, α is the half-width of the initial pulse in inverse seconds, R and R_0 are distances where R_0 is set to a reference distance of 1 km, and c the the fluid velocity We then define the displacement potential ϕ in terms of the pressure as

$$P(t) = \frac{R_0}{R} P_0 e^{-\alpha(t-\frac{R}{c})} = \rho \frac{\partial^2 \phi(t)}{\partial t^2}$$

where ρ is the density and ϕ has units of $length^2$. Solving for the displacement potential is a simple double integration with the initial and final conditions of

$$\begin{aligned} \phi\left(t - \frac{R}{c} = 0\right) &= 0 \\ \int P(t) dt &= 0 \end{aligned}$$

The first condition constrains there to be no motions before the arrival of the initial pulse, while the second allows for the pressure at long times to return to the hydrostatic level.

Therefore the final relation for the displacement potential is

$$\phi(t) = \frac{P_0}{\rho\alpha^2} \frac{R_0}{R} \left(e^{-\alpha t} - 1\right)$$

with the reduced displacement potential, ψ, defined as

$$\psi(t) = -R\phi(t) = -\frac{P_0}{\rho\alpha^2} R_0 \left(e^{-\alpha t} - 1\right)$$

5.3 Waveform Modeling

After some mathematical manipulation of the underwater explosive displacement potential, ϕ, and the greens functions, $S(t)$, we can create synthetic displacement waveforms for underwater explosions. To obtain displacement from the explosion displacement potential, a derivative with respect to distance, R, of ϕ must be taken, as

$$D(R,t) = \frac{d\phi(t)}{dR} = \frac{1}{R^2}\psi(t) + \frac{1}{cR}\frac{d\psi(t)}{dt}$$

The first term in the relation for displacement describes displacement in the near-field and acts as a ramp function. While the second term describes the displacement in the far-field which is similar to a delta-function.

Keeping only the far-field term, following the derivation discussed in *Helmberger* [1983] and *Helmberger and Hadley* [1981], and keeping in mind $r \neq R$, we obtain

$$D(r,z,t) = \left(\frac{d\psi(t)}{dt} * \frac{dS(t)}{dt}\right)$$

where

$$S(t) = \sqrt{\frac{2}{r}}\frac{1}{\pi}\left[\frac{1}{\sqrt{t}} * \sum rays\right]$$

To treat the problem here we need to begin in a thin water layer with a relatively thin crust and ending at the surface of a continental crust. To proceed we use a modification of generalized ray theory similar to that discussed in *Ni et al.* [2000] that allows different source and receiver structure. Thus, we can easily include reverberations in a water layer. Inclusion of the 100m water layer is done solely on the source side by specifying the water as an actual, but small, layer with compressional and shear velocities of 1.5 and $0.0km/sec$ and a density of $1.0g/cm^3$

We used two velocity models, specified in Table 5.1, to create synthetics. The Baltic model [*Bondar and Ryaboy*, 1997] is a model based on travel times for the Baltic shield region, while the K8 model [*Given and Helmberger*, 1980] is derived from WWSSN waveform modeling of explosions. Most likely the Moho is not flat for paths we are considering, and not knowing the crustal thicknesses under the source and receiver we used simple, flat-layered

Table 5.1: Upper Mantle P Velocity Models

Depth $[km]^{\alpha}$	K8	Baltic
0	6.200	6.2000
10	6.700	6.7000
25	8.170	8.0000
40	8.170	8.0000
50	8.178	8.0000
55	8.178	8.1500
60	8.205	8.1570
70	8.222	8.2570
80	8.239	8.3286
90	8.256	8.4000
100	8.274	8.0000
110	8.291	8.0000
115	8.291	8.4200
120	8.308	8.4262
130	8.325	8.4262
135	8.325	8.4446
140	8.343	8.4446
150	8.250	8.4631
155	8.180	8.4631
160	8.050	8.4631
165	8.050	8.4815
170	8.040	8.4815
180	8.150	8.5000

[1] Depths are at the top of the layer
[2] P wave velocity in km/sec

crust of 25 km, rather than a more complex one. Using this simple model and a mapping technique from *Zhao* [1993], the amplitudes and travel times are preserved for differing crustal thicknesses beneath the source and receiver. The short-period Pn/Pg synthetic seismograms, for a suite of source sizes, generated at station ARCESS are displayed along with observations in Figure 5.3. Differences between the full description of the source with bubble pulses included, and the single pulse approximation, or simple decaying exponential, are also shown. The left column of Figure 5.3 is the complete source while the right column only contains the approximation. It is difficult to identify characteristics of the bubble pulse in the time domain, whereas it is relatively simple in the frequency domain.

As seen for both the synthetics and data shown in Figure 5.3, an extended coda is present for the Pn and Pg arrivals. The existence of these arrivals is due entirely to extended water reverberations and not the bubble pulse. A water layer, in relation to the solid earth, is a low velocity layer which can trap seismic energy. Multiple water reverberations are distinct arrivals and can be the most prominent arrivals on regional records, as seen in the data. The frequency of the water reverberations is defined by *Gitterman et al.* [1998] as

$$f_w = \frac{c}{4h_w}$$

where c is the wave velocity in water, and h_w is the water height. Using a wave velocity of $1.5km/sec$ and a h_w of $100m$ the frequency of reverberations becomes 3.75 Hz, similar to

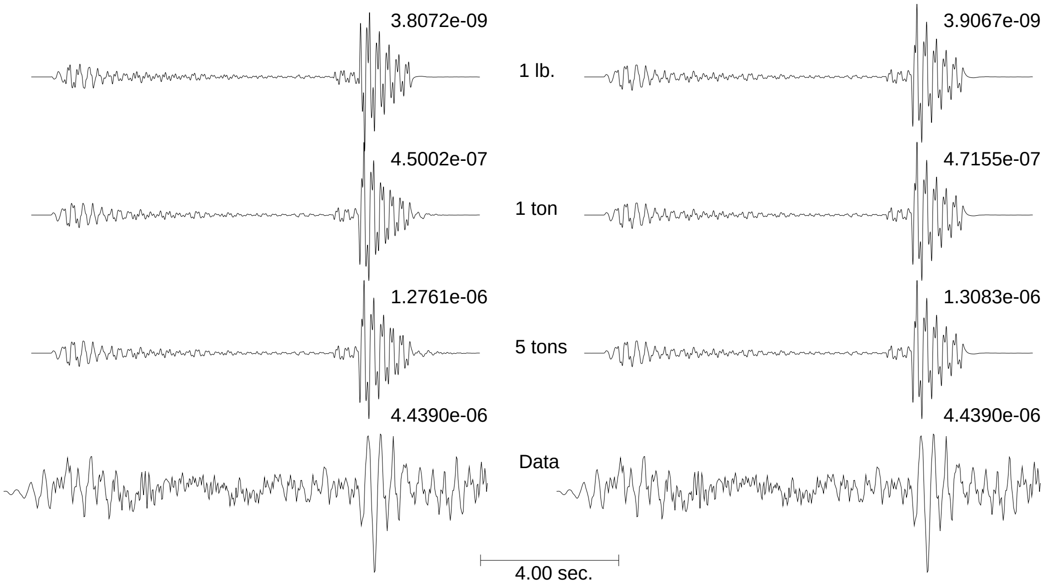

Figure 5.3: Pn/Pg Synthetics created for the full description of the source, first column, and the first pulse approximation, second column. The first three rows are synthetics for explosive sizes of 1 lb., 1 tons, and 5 tons, with amplitudes in cm. The last row is the data recorded at station ARCESS. Waveform shape differences in the final synthetics are only seen for small yields, while larger yields differ only in amplitude.

the data. This extended coda is present throughout the entire record, including P and S waves, as seen in Figure 5.2.

Examining the entire record further, the P arrival strengths exhibit a signal comparable to those for S. Since the S-waves contain water reverberations and the source derived bubble pulses they can be used in the whole record spectral analysis discussed above as a discriminant. Another discriminant utilizes the amplitude ratio of particular phases, namely Pn, Pg, Sn and Sg, commonly known as Lg. Identification of the phase Sn is difficult in Figure 5.2, although a relatively strong complex Sg is evident. This phenomenon of weak Sn, when compared to Sg, or Pn, is common in oceanic exploration with soft bottom sediments [*Helmberger and G.B.*, 1970]. A ratio of the larger amplitude phases, Pn and Sg, for this event is slightly smaller than those reported in *Baumgardt and Younf* [1990] for underwater explosions, although this difference is again, likely due to amount of mud and silt on the seafloor beneath the explosion. Another comparison of the Pn/Sg ratio for this event, ~ 1.0, with earthquakes in this region, ~ 0.5, is similar to those reported by *Baumgardt and Younf* [1990] and *Dysart and Pulli* [1990]. Again, while the water layer affects the character and amplitude of the P and S arrivals in the time domain, the bubble pulse signal will dominate in the frequency domain but identification in waveforms is difficult.

Turning back to Figure 5.3, the largest differences between waveforms with and without the bubble pulse is easily seen at small yields. While large yields only differ in amplitude, the smaller yields have a modified waveform shape. In this example, the Pg arrivals are of opposite polarity compared to larger shots. This is entirely due to the interference produced between the initial explosion and the bubble pulse. Shown in Figure 5.4 are pressure time series computed for a ranges of sizes. The pressure series have been convolved with a double-sided instrument response that accentuates their impact. As shown by Weston [1960], the timing of the bubble pulse shifts towards the initial pulse as the explosion size decreases. Therefore, for smaller sized sources, detonated at a constant depth, the bubble pulse interferes with the initial pulse to create complicated waveforms.

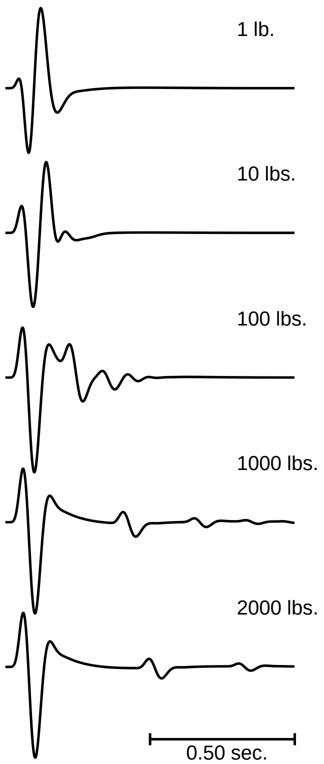

Figure 5.4: Pressure time series convolved with an instrument response for a series of explosive sizes. Note how the later pulses for the larger shots interfere with the initial pulse as the shot size decreases.

Waveform data used in this study have amplitudes comparable to to those from an explosion greater than 1 ton. Knowing this, we can only use the amplitude of the waveform to determine the size, because at large yields the waveform shape does not change. A comparison of synthetics at 1 ton for the two models against all the observations are given in Figure 5.5. For comparison, the synthetics are convolved with the same instrument that recorded the data. Each model fits the arrival time and energy envelopes at distances greater than 650 km, but the K8 model explains the arrival times and relative Pn/Pg amplitudes at APA and ARCESS better than the Baltic model. Both models show characteristics not seen in the data for larger distances. Around 700 km, the Baltic model's upper mantle produces a critically reflected arrival resulting in larger than expected amplitudes. While the K8 model, has a large secondary arrival, coming from the top of the low velocity zone, 5 seconds following the initial arrival.

Although we would expect to see an impulsive compressional first motion, positive on the vertical component, most observations appear to be either weak or negative. At smaller distances the synthetics from both models are positive, but as the distance increases the first arrival becomes weak or negative. More distant recordings sample a greater extent of the lid structure. To accurately model this set of data, with a large percentage of energy centered around $3Hz$, we need to know the very fine structure of the lid, to within a few kilometers. These models in Table 5.1, derived from travel time data, do not have the resolution required to model at the required frequencies.

Synthetics for the K8 and Baltic models are computed for a range of different yields from 1 lb. to 50 tons. From these synthetics, the maximum P wave amplitudes are plotted against those from the data in Figure 5.6. This data shows the larger explosion had a yield of slightly over 4 tons, in mean and median using the K8 model. The Baltic model, on the other hand, predicts a smaller yield between 2 and 3 tons. Unfortunately, the smaller explosion's signal to noise is too small to determine a yield using this method. Other classical methods of explosion size determination, employed by *Koper et al.* [2001] for the same explosion show a range similar yields of approximately 4 tons.

If we then assume the Kursk was carrying missiles with a conventional explosive yield of 750 kg and the explosion was slightly more than 3628 kg, then about 5 missiles exploded in the large explosion. Knowing the size of the nuclear warheads, we can conclude the no nuclear warheads were detonated in the explosion. Knowing the size of the first and smaller

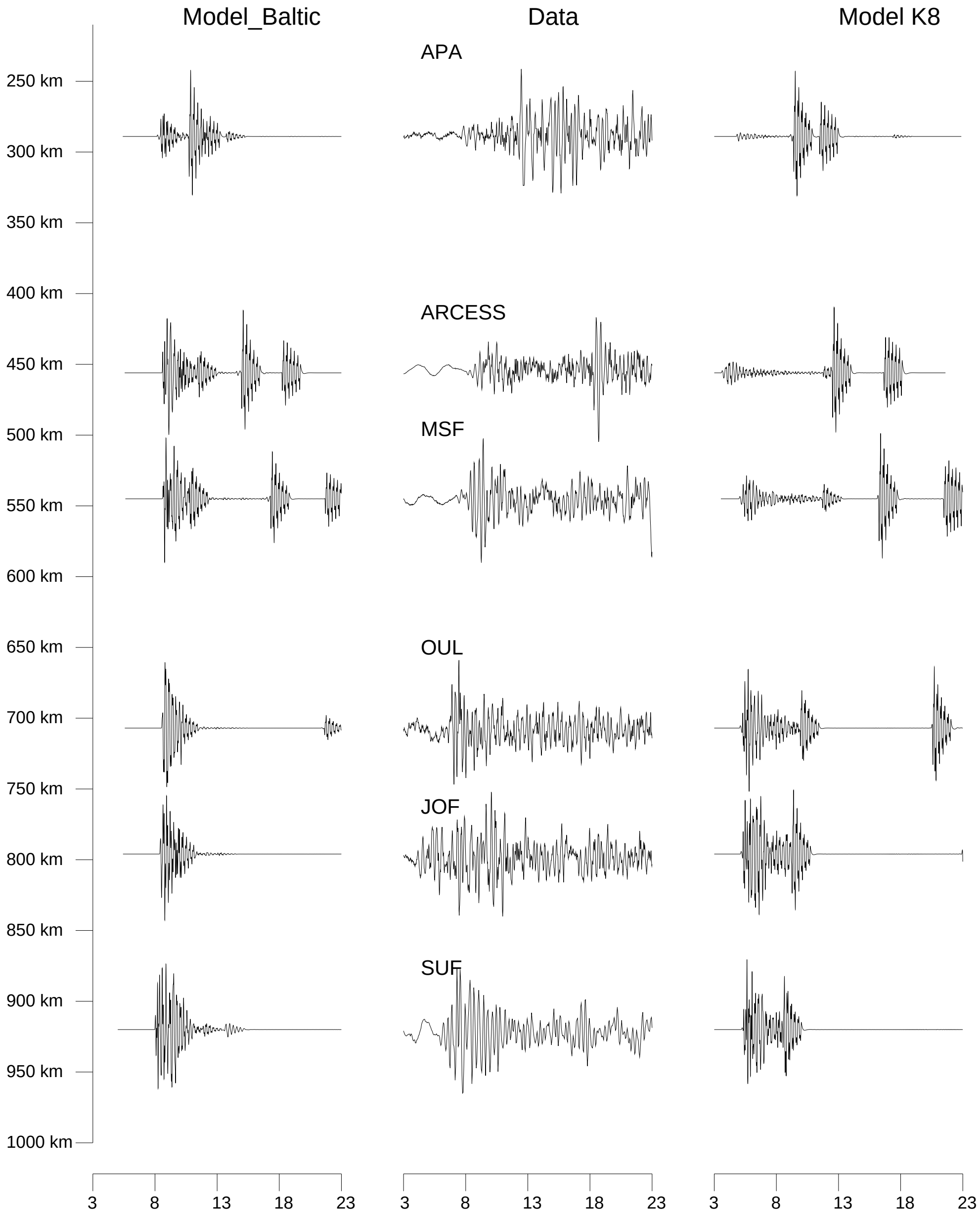

Figure 5.5: Record section of data, in the center column, and synthetics for the two velocity models used in this study. The peak amplitude considerations are give in Figure 6.

explosion would give us a better insight into what the original cause of the incident was.

5.4 Conclusion

We have estimated the size of the second larger explosion on board the Russian submarine, the Kursk. Our new method obtains a yield of slightly larger than 4 tons (3628 kg),

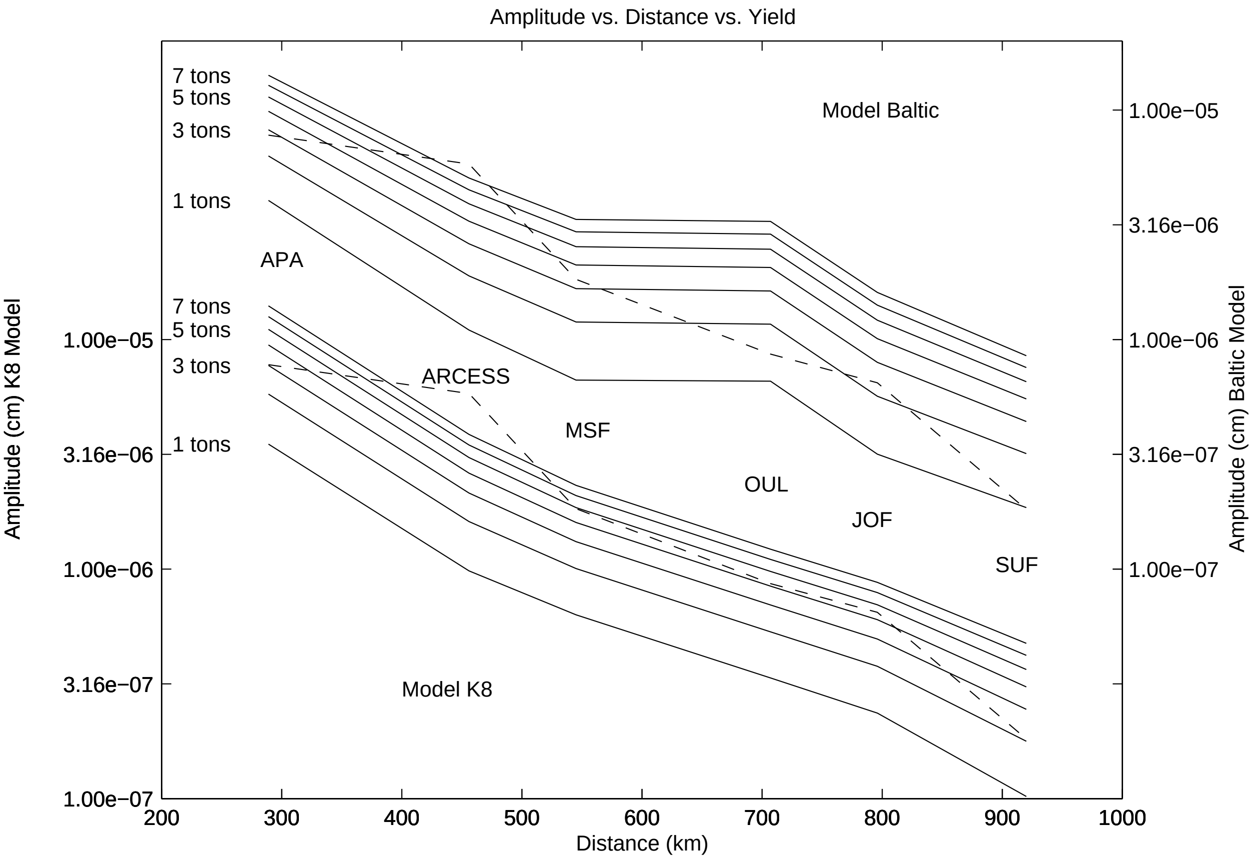

Figure 5.6: Maximum P amplitude (cm) plotted versus distance and yield. The top set of curves are for the Baltic model and have their axis on the right. While the bottom set correspond to the K8 model and have their axis on the left. The data for each is the dotted line and the solid lines are maximum amplitudes from 1 to 7 ton shots increasing by 1 ton for each line.

equaling about five 750 kg missiles. By employing this new method of matching amplitudes of synthetics to those of seismic waveform data, we can recover the size which agrees with other methods. By using this method and time domain records, more information about underwater explosions can be extracted. First, the recorded waveforms show that the largest amplitudes arrivals are due to successive water reverberations and not the bubble pulse. Secondly, the secondary sources become unimportant in the time domain, when the yield exceeds a threshold. Next, the relative amplitude of P to S can be used as a discriminant for explosions in water. Along with the P to S ratio, identification of bubble pulses in the frequency domain and water reverberations in the time domain can act in concert to discriminate and underwater explosion from an earthquake. Finally, we have developed a method of creating synthetics for underwater explosions describing the source and how the seismic waves propagate within a water layer.

Acknowledgements

We would like to thank Brad Woods, Hong-Kie Thio, Chandan Saikia, Jascha Polet and two anonymous reviewers for their reviews, Ralph Alewine for his suggestion to attempt this work numerically, Terry Wallace and Keith Koper for their discussions and data from the University of Arizona, Tucson and finally Hans Israelsson and Ulf Baadshaug for waveform data. This research was supported by the Defense Threat Reduction Agency under contract DSWA01-98-1-0010. Contribution No. 8745, Division of Geological and Planetary Sciences, California Institute of Technology, Pasadena, California.

Appendix A

Sierra Nevada Auxiliary Data

More data were collected and examined following the investigation of the southern Sierra Nevada, Chapter 1. This data includes Pn arrival times and waveform data from local earthquakes and waveform data from regional earthquakes. This data confirms out previous assertion of a substantial slowing of the mantle velocity. Upon further examination, the data also show interesting features, such as the northern and western boundaries, which were not identified in the previous data set.

A.1 Pn arrival times

Shown in Figures A.1 and A.2 are hand-picked Pn arrival times for two earthquakes in northern California. Pn times are plotted in color after applying a reduction velocity of 7.8 km/s. Blue colors indicate faster than average arrivals while red colors are slower than average. Time picks were made on a heterogeneous set of instruments from broadband (TriNet and BDSN) to short-period instruments(NCSN and SCSN). Topography is used for background shading and the black dots are recording stations. A circle is drawn at 150 km distance from the earthquake epicenter. Inside this circle, time picks are reduced with a crustal velocity of 6.8 km/s as the first arrivals did not refract along the base of the crust.

Figure A.1 shows the arrival time data from the San Simeon, CA earthquake.(2003/12/22 19:15:56) Notice the abrupt change in color from red to green across the Garlock Fault at the southern-most point of the Sierra Nevada. Further, the late arrivals extend further north than Mammoth Lakes, CA. Our previous results had no constraints north of Mammoth Lake, CA. The southern-most points in California conversely show early arrival times. This is most likely due to thinning of the crust towards the Gulf of California. Finally, most of

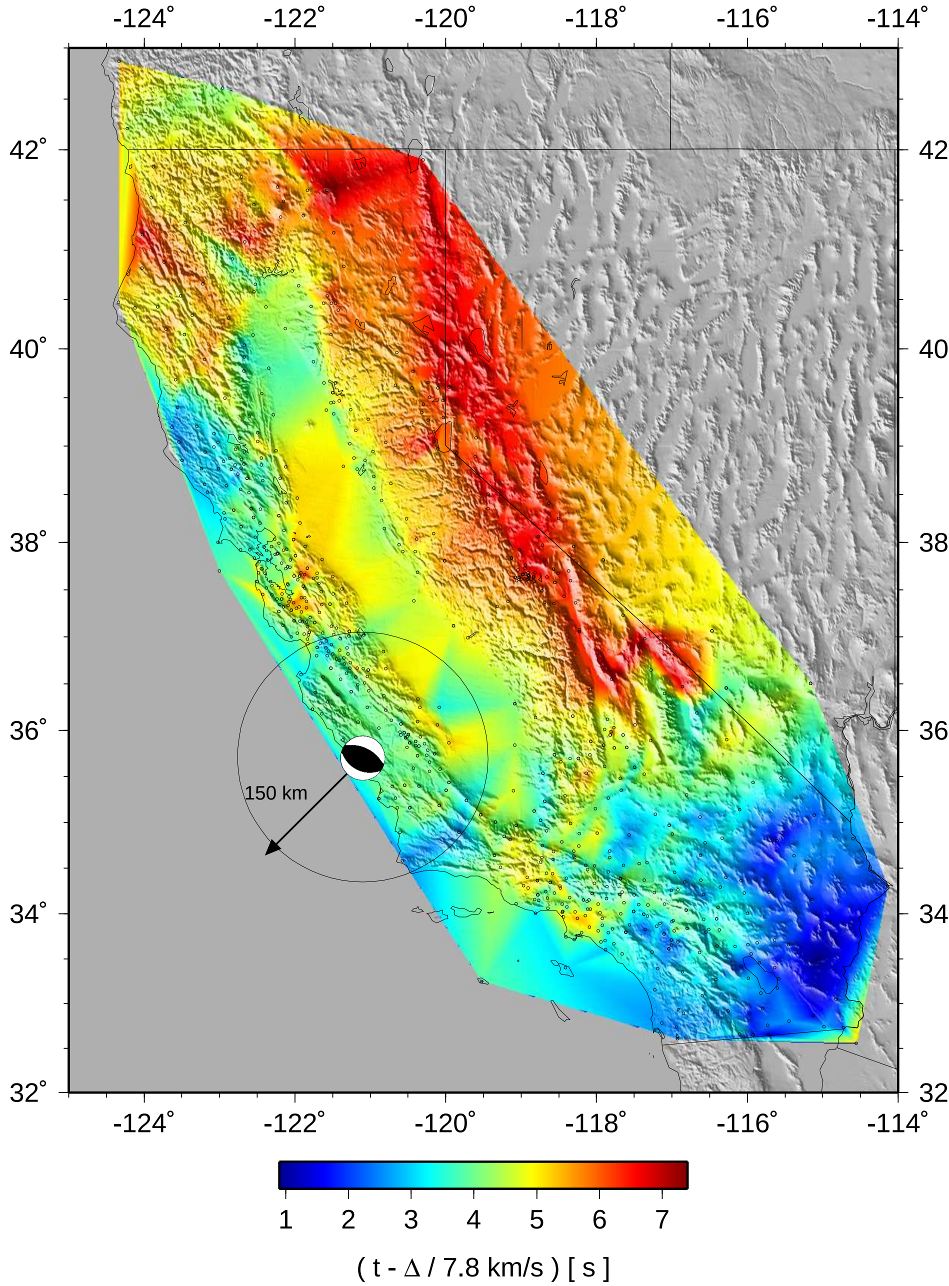

Figure A.1: P wave arrival times from the San Simeon earthquake

the Central Valley, Coast Ranges, and Los Angeles regions are intermediate in arrival times.

Figure A.2 displays arrival time data for an earthquake near Portola, CA.(2001/8/10 10:19:26) The data from this event have a similar pattern to the data from the San Simeon event. Again, the Central Valley and Coast Ranges are intermediate in arrival time. All data that traverses the Sierra Nevada are delayed in time. A large region of delayed arrival

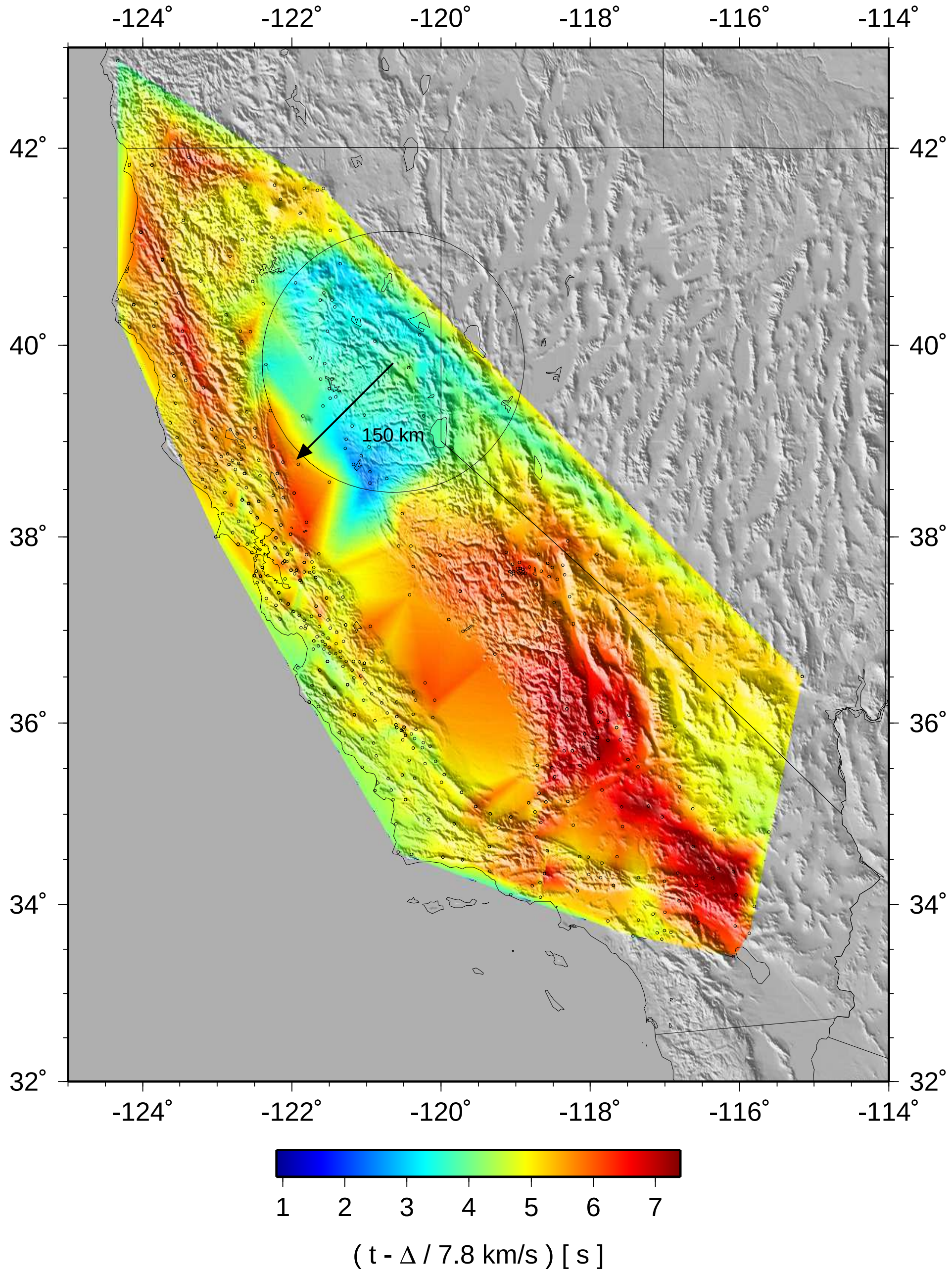

Figure A.2: P wave arrival times from the Portola earthquake

times is aligned along the axis of the Sierra Nevada. This region extends into the Mojave Desert and San Bernardino Mountains. This data may appear slow because the wavefield has not interacted with a velocity faster than 7.8 km/s to reduce the magnitude of delay. This also may indicate that the slower velocities underlying the Sierra Nevada may extend to great depths.

A.2 Pn Waveforms

To obtain a reverse profile that complements our previous results, we examined data from two earthquakes in the Gulf of California. Data from these events were also used in our study of complex phenomena of Rayleigh Waves, Chapter 4. Figures A.3 and A.4 show record sections for two events where the data are plotted with a reduction velocity of 7.8 km/s and are shifted with distance to align individual stations.

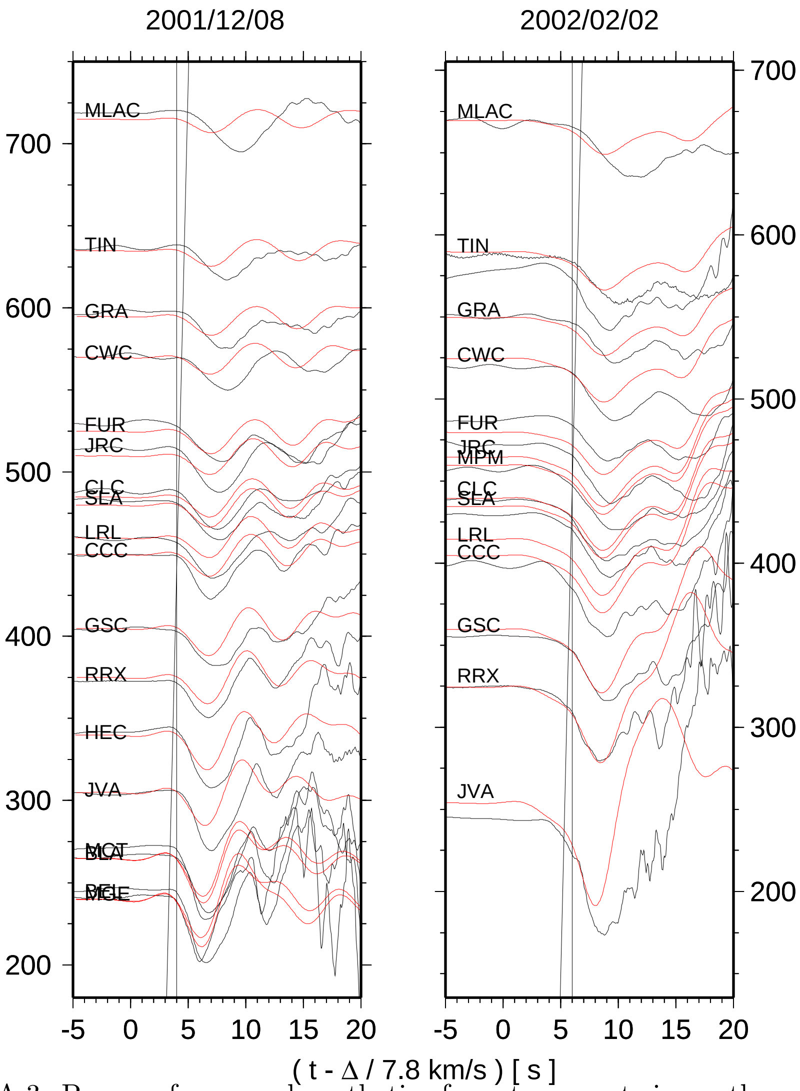

Figure A.3: Pn waveforms and synthetics from two events in northern Mexico.

Included in the record sections are 1-D frequency wavenumber synthetics with a mantle velocity of 7.8 km/s (red). We use the synthetics as a metric to compare the data from west to east. Data for both events show similar characteristics. Each data set indicates velocities slower than 7.8 km/s at western stations (TIN and MLAC) and faster than 7.8 km/s for western stations (PHL and SMM). Note that station RCT in Figure A.4 is the easternmost station of the western swath. Station RCT shows little deviation from a velocity of 7.8 km/s.

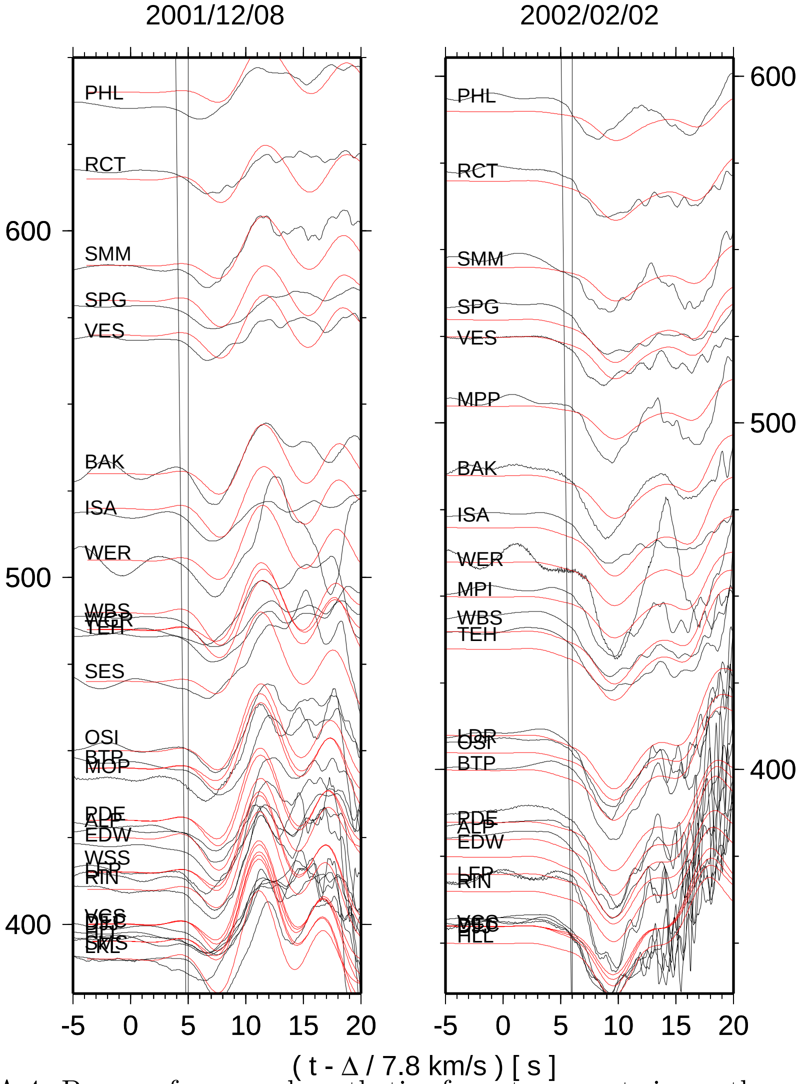

Figure A.4: Pn waveforms and synthetics from two events in northern Mexico.

Neither of these earthquakes created the dramatic waveforms including Pn’ that were witnessed in our previous study, Chapter 1. Synthetics created for this profile using our preferred model of the mantle shows Pn’ begins to appear at a distance greater than the northern most station, MLAC.

A.3 Regional Waveforms

The final set of auxiliary data is from an earthquake in the central Gulf of California.(2003/03/12 23:41:30) P and S waves from 7 to 20 degrees were recorded by the TriNet and BDSN broadband arrays. At these distances, the arrivals are transitioning from refracted Pn and Sn to turning P and S. For this region and these distances, we assume the P arrival turns below the lithosphere and encounters the low velocity zone.

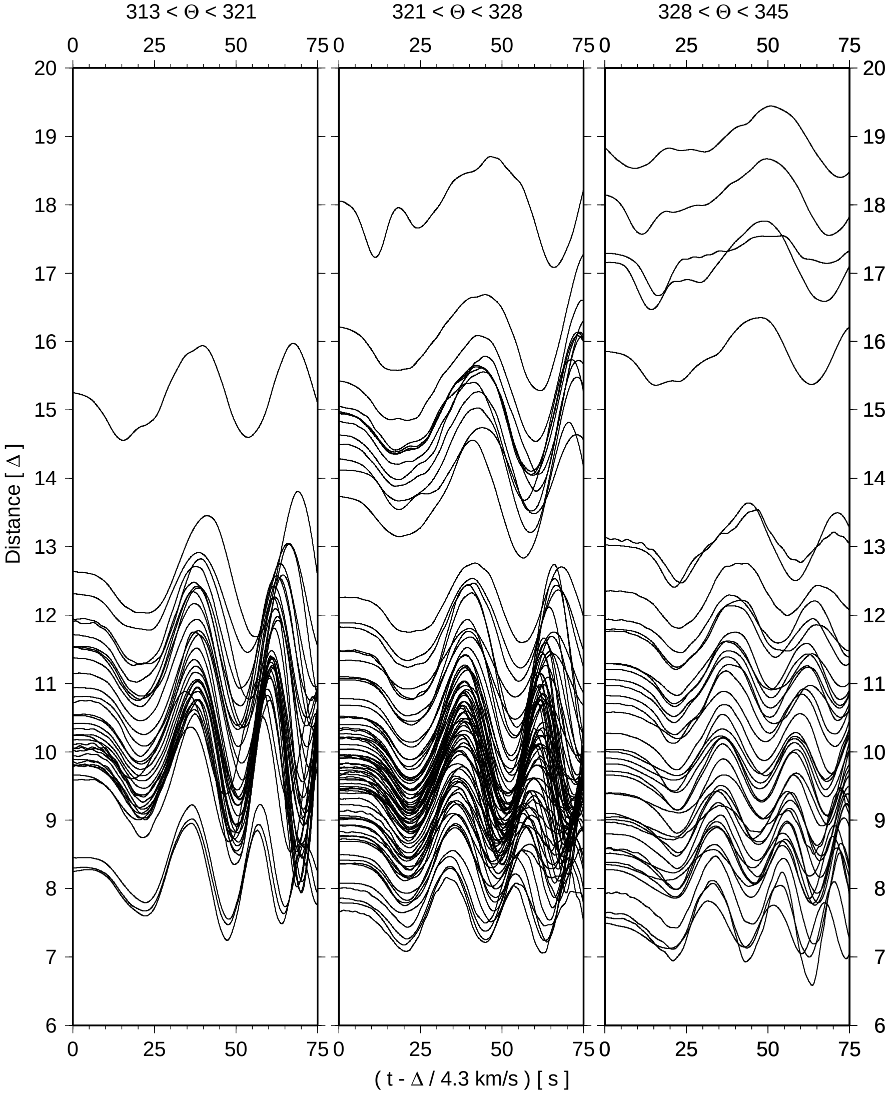

Figure A.5: Sn waveforms from one event in the Gulf of California.

Figure A.5 shows three azimuthal swaths of tangential data. The data are reduced by 4.3 km/s and are not filtered, only deconvolved to displacement. At distances of < 10 degrees, Sn has a distinct inverted triangle shape and is of high frequency (8 degrees, all columns). As the distance grows, the first arrival broader in time and appears to reduce in frequency (13 degrees, columns 1 and 2). The broadening of the first arrival is the from the interaction of the turning arrival with the low velocity zone. Beyond 14 degrees, an increase in velocity is apparent on all columns. This increase in velocity is due to the first arrival starting to interact with faster velocities (faster than the lithosphere) below the low velocity zone. The expected triplication from the 410 km discontinuity is difficult to pick in these data, but should occur around 17-19 degrees.

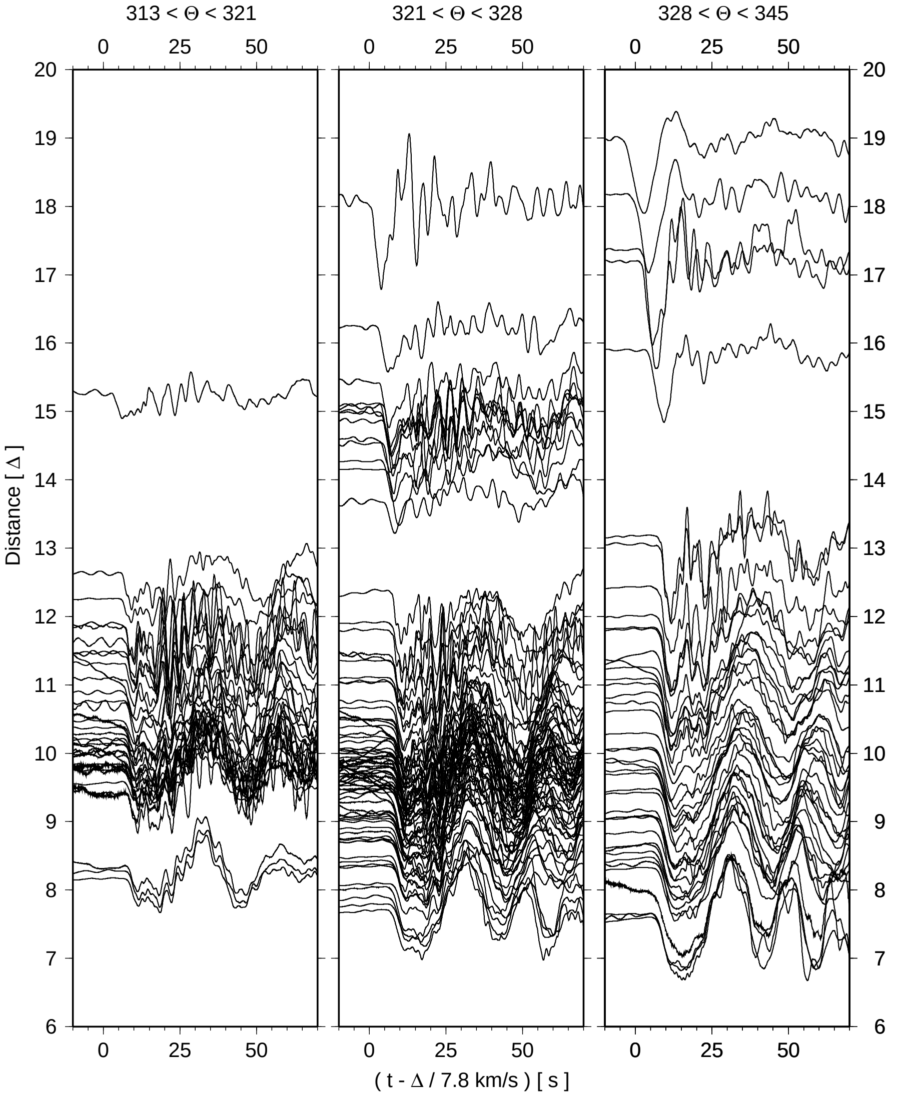

Figure A.6: Pn waveforms from one event in the Gulf of California.

The last item to notice is the differences in waveshape of the first arrival of columns 1 and 2 versus column 3. Data in column 3 traverses the southern Sierra Nevada and would propagate through the low velocity zone we proposed earlier. The data at 13 degrees in column 3 are delayed in time and are higher in frequency content than similar data in columns 1 and 2. The increase in velocity seen in columns 1 and 2 beyond 12 degrees is absent in columns 3. This suggests a thicker lithosphere or a reduced low velocity zone beneath the data presented in column 3.

Similar features are present for the vertical displacement data from the same event (Figure A.6). The vertical data are reduced with a velocity of 7.8 km/s. From west to east (columns 1 to 3) the data grow in amplitude. This is due to the faulting mechanism. However, we still see a lack in velocity increase in column 3 near 12 degrees, as expected in columns 1 and 2. The first arrivals in column 3 also appear higher in frequency from 11 to 13 degrees.

Appendix B

San Bernardino Mountains

In order to carry out the sensitivity tests for our investigation of the San Bernardino Mountain crustal root (Chapter 2), a variety of finite difference models were run. First arrivals time picks were made on these synthetics from the finite difference runs. The first arrival times are displayed in Figure B.1. The top panel shows the initial break, first arrival times while the bottom panel shows the picks of maximum amplitude of Pn.

The models used in Figure B.1 include the Basic model (black) from SCECV2 and [*Zhu and Kanamori*, 2000], a flat crust model (yellow), a model with the crustal root shifted towards (red) and away (blue) from the source, and a thicker crust than the basic. The basic and thicker crust are those which have synthetics in Figure 2.3.

The differences between the flat crust and basic crustal root are dramatic. A delay of almost 1.0 second is easily seen between the two models. By shifting the crustal root towards and away from the source correspondingly modifies the position of the delay. Making the crust thicker increases the magnitude of the delay, but not the position.

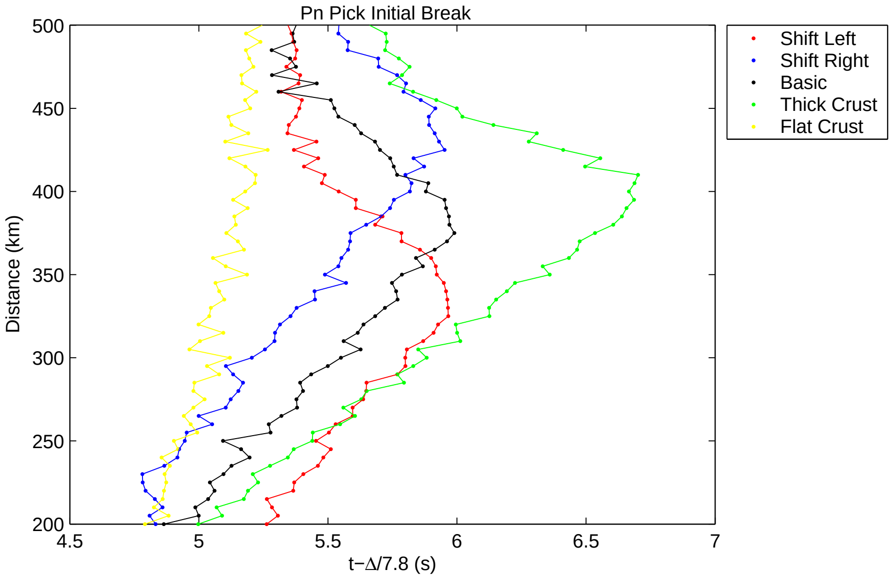

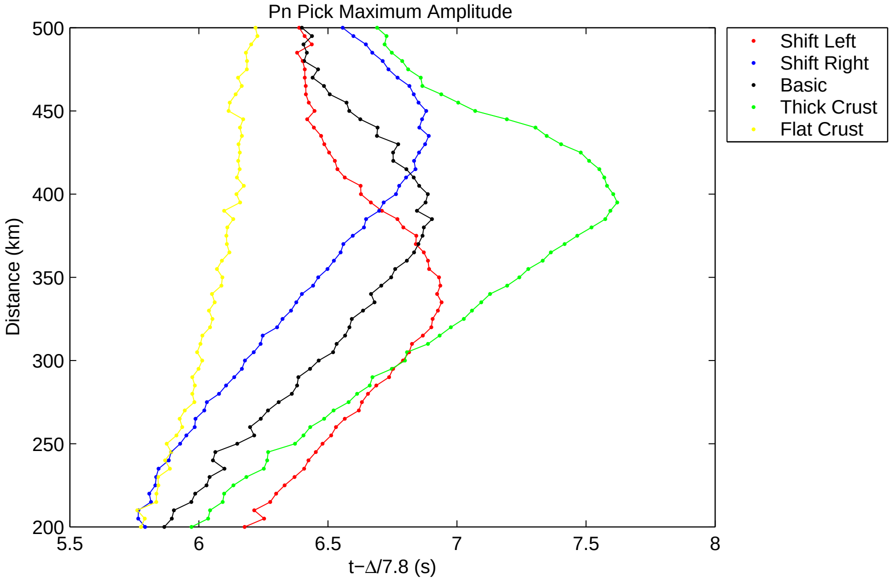

Figure B.1: Pn travel times from numerous finite difference models showing the effect on the waveforms due to changing the position and thickness of the crustal root.

Bibliography

Arons, A., Underwater explosion shock wave parameters at large distances from the charge, *J. Acoust. Soc. Am*, *25*, 343–346, 1954.

Atwater, T., and J. Stock, Pacific North America plate tectonics of the Neogene southwestern United States: An update, *International Geology Review*, *40*, 375–402, 1998.

Bailey, R. A., G. B. Dalrymple, and M. A. Lanphere, Volcanism, structure, and geochronology of Long Valley Caldera, Mono County, California, *Jour. Geophys. Res.*, *81*, 725–744, 1976.

Bateman, P. C., and J. P. Eaton, Sierra Nevada Batholith, *Science*, *158*, 1407–1417, 1967.

Baumgardt, D., and Z. Der, Identification of presumed shallow underwater chemical explosions using land-based arrays, *Bull. Seismo. Soc. Am.*, *88*, 581–595, 1998.

Baumgardt, D., and G. Younf, Regional Seismic Waveform Discriminants and Case-Based Event Identification using Regional Arrays, *Bull. Seismo. Soc. Am.*, *80*, 1874–1892, 1990.

Bellona Foundation, P., Bellona foundation, http://www.bellona.no, 2000.

Biasi, G., and E. Humphreys, P-wave image of the upper mantle structure of central California and southern Nevada, *Geophys. Res. Lett*, *19*, 1161–1164, 1992.

Bondar, I., and V. Ryaboy, Regional travel-times tables for the baltic shield region, *CMR Technical Report*, *24*, 1997.

Burchfiel, B. C., D. S. Cowan, and G. A. Davis, *The Geology of North America: Chapter 8 - Tectonic overview for the Cordilleran orogen in the western United States*, vol. G-3 The Cordilleran Orogen: Conterminous U.S., Geol. Soc. Am., 1992a.

Burchfiel, B. C., P. W. Lipman, and M. L. Zoback, *The Geology of North America: Chapter 1 - Introduction*, vol. G-3 The Cordilleran Orogen: Conterminous U.S., Geol. Soc. Am., 1992b.

Byerly, P., Comment on "The Sierra Nevada in the light of isostasy", *Bull. Geol. Soc. Am.*, *48*, 2025–2031, 1937.

Carder, D. S., Trans-California seismic profile, Death Valley to Monterey Bay, *Bull. Seismo. Soc. Am.*, *63*, 571–586, 1973.

Carder, D. S., A. Qamar, and T. V. McEvilly, Trans-California seismic profile-Pahute Mesa to San Francisco Bay, *Bull. Seismo. Soc. Am.*, *60*, 1829–1846, 1970.

Chase, C. G., and T. C. Wallace, Flexural isostasy and uplift of the Sierra Nevada of California, *Jour. Geophys. Res.*, *93*, 2795–2802, 1988.

Cole, R., *Underwater Explosions*, Princeton University Press, Princeton, New Jersey, 1948.

Crough, S. T., and G. A. Thompson, Upper mantle origin of Sierra Nevada uplift, *Geology*, *5*, 396–399, 1977.

Ding, X., and D. V. Helmberger, Modelling D" structure beneath Central America with broadband seismic data, *Phys. of Earth and Planetary Interiors*, *101*, 245–270, 1997.

Ducea, M. N., and J. B. Saleeby, Buoyancy sources for a large, unrooted mountain range, the Sierra Nevada, California: Evidence from xenolith thermobarometry, *Jour. Geophys. Res.*, *101*, 8229–8244, 1996.

Ducea, M. N., and J. B. Saleeby, Crustal recycling beneath continental arcs: silica-rich glass inclusions in ultramafic xenoliths from the Sierra Nevada, California, *Earth Plan. Sci. Lett.*, *156*, 101–116, 1998a.

Ducea, M. N., and J. B. Saleeby, The age and origin of a thick mafic-ultramafic keel from beneath the Sierra Nevada batholith, *Contrib. Mineral Petrol.*, *133*, 169–185, 1998b.

Ducea, M. N., and J. B. Saleeby, *Integrated earth and enviornment evolution of the southwestern United States: the Clarence A. Hall, Jr. volume*, chap. A Case for Delamination of the Deep Batholithic Crust beneath the Sierra Nevada, California, pp. 273–288, Papers from a symposim help Sept. 13-15, 1997 at the Crooked Creek Conference Center (Calif.), Bellwether Pub Ltd. for the Geological Society of America, Columbia, Md., 1998c.

Dumitru, T. A., P. B. Gans, D. A. Foster, and E. L. Miller, Refrigeration of the western Cordilleran lithosphere during, *Geology*, *19*, 1145–1148, 1991.

Dysart, P., and J. Pulli, Regional Seismic Event Classification at the NORESS Array: Seismological Measurements and the use of Trained Neural Networks, *Bull. Seismo. Soc. Am.*, *80*, 1874–1982, 1990.

Eaton, J. P., Crustal structure in northern and central California from seismic evidence, *Bull. Calif. Civ. Mines Geol.*, *190*, 419–426, 1966.

Field, E., Accounting for site effects in probabilistic seismic hazard analyses of southern California: Overview of the SCEC phase III report, *Bull. Seismo. Soc. Am.*, *90*, S1–S31, 2000.

Fliedner, M., S. Klemperer, and N. Christensen, Three-dimensional seismic model of the Sierra Nevada arc, California, and its implications for crustal and upper mantle composition, *Jour. Geophys. Res.*, *105*, 10,899–10,921, 2000.

Fliedner, M. M., and S. Ruppert, Three-dimensional crustal structure of the southern Sierra Nevada from seismic fan profiles and gravity modeling, *Geology*, *24*, 367–370, 1996.

Fuis, G., W. Mooney, J. Healy, G. McMechan, and W. Lutter, A Seismic Refraction survey of the Imperial-Valley region, California, *Jour. Geophys. Res.*, *89*, 1165–1189, 1984.

Gitterman, A. S., Y., Spectral characteristics of seismic events off the coast of levant, *Geophs. Jour. Int.*, *116*, 485–497, 1994.

Gitterman, Y., Z. Ben-Avraham, and A. A. Ginzburg, Spectral analysis of underwater explosions in the dead sea, *Geophs. Jour. Int.*, *134*, 460–472, 1998.

Given, J., and D. Helmberger, Upper mantle structure of norhtwestern eurasia, *Jour. Geophys. Res.*, *85*, 7193–7194, 1980.

Grand, S. P., and D. V. Helmberger, Upper mantle shear structure of North America, *Geophys. J. R. astr. Soc.*, *76*, 399–438, 1984.

Hadley, D., and H. Kanamori, Seismic Structure of Transverse Ranges, California, *Geol. Soc. Am. Bull.*, *88*, 1469–1478, 1977.

Hartzell, S., S. Harmsen, A. Frankel, D. Carver, E. Cranswick, M. Meremonte, and J. Michael, First-generation site-response maps for the Los Angeles region based on earthquake ground motions, *Bull. Seismo. Soc. Am.*, *88*, 463–472, 1998.

Helmberger, D., The Crust Mantle Transition in the Bering Sea, *Bull. Seismo. Soc. Am.*, *58*, 179–214, 1968.

Helmberger, D., Theory and application of synthetics seismograms, in *Earthqaukes: Observation, Theory and Interpretation*, edited by H. Kanamori and E. Boschi, pp. 174–222, North-Holland, Amsterdam, 1983.

Helmberger, D., and M. G.B., A Travel Time and Amplitude Interpertation of a Marine Refraction Profile: Transformed Shear Waves, *Bull. Seismo. Soc. Am.*, *60*, 593–600, 1970.

Helmberger, D., and D. Hadley, Seismic source functions and attenuation from local and teleseismic observations of the nts events jourm and handley, *Bull. Seismo. Soc. Am.*, *71*, 51–67, 1981.

Helmberger, D. V., and G. R. Engen, Modeling the long-period body waves from shallow earthquakes at regional ranges, *Bull. Seismo. Soc. Am.*, *70*, 1699–1714, 1980.

Helmberger, D. V., and J. E. Vidale, Modeling strong motions produced by earthquakes with two-dimensional numerical codes, *Bull. Seismo. Soc. Am.*, *78*, 109–121, 1988.

Ho-Liu, P., and D. Helmberger, Modeling Regional Love waves - Imperial-Valley to Pasadena, *Bull. Seismo. Soc. Am.*, *79*, 1194–1209, 1989.

Hough, S., J. Tinsley, A. Youg, H. Kanamori, E. Yu, V. Appel, and C. Wills, Geotechnical characterization of TriNet sites, *in preperation*, 2003.

Houseman, G., E. Neil, and M. Kohler, Lithospheric instability beneath the Transverse Ranges of California, *Jour. Geophys. Res.*, *105*, 16,237–16,250, 2000.

Ichinose, G., S. Day, H. Magistrale, T. Prush, F. Vernon, and A. Edelman, Crustal thickness variations beneath the Peninsular Ranges, southern California, *Geophys. Res. Lett*, *23*, 3095–3098, 1996.

Jones, C. H., and R. A. Phinney, Seismic structure of the lithosphere from teleseismic converted arrivals observed at small arrays in the southern Sierra Nevada and vicinity, California, *Jour. Geophys. Res.*, *103*, 10,065–10,090, 1998.

Jones, C. H., H. Kanamori, and S. W. Roecker, Missing roots and mantle "drips": Regional Pn and teleseismic arrival times in the southern Sierra Nevada and vicinity, California, *Jour. Geophys. Res.*, *Vol 99*, 4567–4601, 1994.

Jones, L. E., and D. V. Helmberger, Earthquake source parameters and fault kinematics in the eastern California shear zone, *Bull. Seismo. Soc. Am.*, *88*, 1337–1352, 1998.

Kawase, H., and K. Aki, A study on the response of a soft basin for incident S-waves, P-waves and Rayleigh-waves with special reference to the long duration observed in Mexico-city, *Bull. Seismo. Soc. Am.*, *79*, 1361–1382, 1989.

Kohler, M., Lithospheric deformation beneath the San Gabriel Mountains in the southern California Transverse Ranges, *Jour. Geophys. Res.*, *104*, 15,025–15,041, 1999.

Komatitsch, D., and J. Tromp, Introduction to the spectral-element method for 3-D seismic wave propagation, *Geophs. Jour. Int.*, *139*, 806–822, 1999.

Koper, K., T. Wallace, T. S.R., and H. H., Forensic seismology and the sinking of the kursk, *EOS*, 2001.

Langston, C., Corvallis, Oregon, Crustal and upper mantle receiver structure from teleseismic P-waves and S-waves, *Bull. Seismo. Soc. Am.*, *67*, 713–724, 1977.

Lawson, A. C., The Sierra Nevada in the light of isostasy, *Bull. Geol. Soc. Am.*, *47*, 1691–1712, 1936.

Lermo, J., and F. Chavezgarcia, Site effect evaluation using spectral ratios with only one station, *Bull. Seismo. Soc. Am.*, *83*, 1574–1594, 1993.

Lewis, J., S. Day, H. Magistrale, J. Eakins, and F. Vernon, Regional crustal thickness variations of the peninsular ranges, southern california, *Geology*, *28*, 303–306, 2000.

Lewis, J., S. Day, H. Magistrale, R. Castro, L. Astiz, C. Rebollar, J. Eakins, F. Vernon, and J. Brune, Crustal thickness of the peninsular ranges and gulf extensional province in the californias, *Jour. Geophys. Res.*, *106*, 13,599–13,611, 2001.

Liu, M., and G. Zandt, Convective thermal instabilities in the wake of the migrating Mendocino triple junction, California, *Geophys. Res. Lett*, *23*, 1573–1576, 1996.

Magistrale, H., S. Day, R. Clayton, and R. Graves, The SCEC southern California reference three- dimensional seismic velocity model Version 2, *Bull. Seismo. Soc. Am.*, *90*, S65–S76, 2000.

Melbourne, T., and D. V. Helmberger, Mantle control of the plate boundary deformation, *Geophys. Res. Lett*, *28*, 4003–4006, 2001.

Nakamura, Y., A method for dynamic characteristics estimation of subsurface using microtremor on the ground surface, *QT RTRI*, *30*, 25–33, 1989.

Ni, S., X. Ding, and D. Helmberger, Constructing synthetics from deep earth tomographic model, *Geophs. Jour. Int.*, *140*, 71–82, 2000.

Pakiser, L. C., and J. N. Brune, Seismic models of the root of the Sierra Nevada, *Science*, *210*, 1088–1094, 1980.

Pasyanos, M., D. Dreger, and B. Romanowicz, Toward real-time estimation of regional moment tensors, *Bull. Seismo. Soc. Am.*, *86*, 1255–1269, 1996.

Pollitz, F., Regional velocity structure in northern California from inversion of scattered seismic surface waves, *Jour. Geophys. Res.*, *104*, 15,043–15,072, 1999.

Richards-Dinger, K., and P. Shearer, Estimating crustal thickness in southern California by stacking PmP arrivals, *Jour. Geophys. Res.*, *102*, 15,211–15,224, 1997.

Saikia, C., Modified frequency-wave-number algorithm for regional seismograms using filons quadrature - modeling of L(g) waves in eastern North-America, *Geophs. Jour. Int.*, *118*, 142–158, 1994.

Saikia, C., D. Dreger, and D. Helmberger, Modeling of energy amplification recorded within greater Los-Angeles using irregular structure, *Bull. Seismo. Soc. Am.*, *84*, 47–61, 1994.

Saltus, R., and A. Lachenbruch, Thermal evolution of the Sierra-Nevada - Tectonic implications of new heat-flow data, *Tectonics*, *10*, 325–344, 1991.

Savage, B., and D. V. Helmberger, Kursk explosion, *Bull. Seismo. Soc. Am.*, *91*, 753–759, 2001.

Savage, B., and D. V. Helmberger, Site response from incident PnL waves, *Bull. Seismo. Soc. Am.*, *94*, 357–362, 2004a.

Savage, B., and D. V. Herlmberger, Complex Rayleigh waves resulting from deep sedimentary basins, *218*, 229–239, 2004b.

Savage, B., C. Ji, and D. V. Helmberger, Velocity variations in the uppermost mantle benearth the southern Sierra Nevada and Walker Lane, *Jour. Geophys. Res.*, *108 (B7)*, ESE 2, 2003.

Savage, M. K., L. Li, J. P. Eaton, C. H. Jones, and J. N. Brune, Earthquake refraction profiles of the root of the Sierra Nevada, *Tectonics*, *13*, 803–817, 1994.

Schmitz, M., W. Heinsohn, and F. Schilling, Seismic, gravity and petrological evidence for partial melt beneath the thickened central Andean crust (21-23 degrees s), *Tectonophysics*, *270*, 313–326, 1997.

Scrivner, C., and D. Helmberger, Seismic wave-form modeling in the Los-Angeles basin, *Bull. Seismo. Soc. Am.*, *84*, 1310–1326, 1994.

Siddiqqi, J., and G. Atkinson, Ground-motion amplification at rock sites across Canada as determined from the horizontal-to-vertical component ratio, *Bull. Seismo. Soc. Am.*, *92*, 877–884, 2002.

Snow, J. K., and B. P. Wernicke, Cenozoic tectonism in the central Basin and Range: Magnitude, rate, and distribution of the upper crustal structure, *Am. Jour. Sci.*, *300*, 659–719, 2000.

Sonder, L. J., and C. H. Jones, Western United States extension: How the west was widened, *Annu. Rev. Earth Planet Sci.*, *27*, 417–462, 1999.

Weiland, C. M., L. K. Steck, P. B. Dawson, and V. A. Korneev, Nonlinear teleseismic tomography at Long Valley Caldera, using three-dimensional minimum travel time ray tracing, *Jour. Geophys. Res.*, *100*, 20,379–20,390, 1995.

Wernicke, B., *The Geology of North America: Chapter 12 - Cenozoic extensional tectonics of the U.S. Cordillera*, vol. G-3 The Cordilleran Orogen: Conterminous U.S., Geol. Soc. Am., 1992.

Wernicke, B., and J. K. Snow, Cenozoic tectonism in the central Great Basin and Range: Motion of the Sierran-Great Valley Block, *Int. Geol. Rev.*, *40*, 403–410, 1998.

Wernicke, B., et al., Origin of high mountains in the continents: The southern Sierra Nevada, *Science*, *271*, 190–193, 1996.

Weston, D., Underwater explosions as acosutic sources, *Proc. Phys. Soc*, *76*, 233–249, 1960.

York, J. E., and D. V. Helmberger, Low-velocity zone variations in the southwestern United States, *Jour. Geophys. Res.*, *78*, 1883–1886, 1973.

Zandt, G., and C. Carrigan, Small-scale convective instability and upper-mantle viscosity under California, *Science*, *261*, 460–463, 1993.

Zhao, L. S., Lateral variations and azimuthal isotropy on Pn velocities beneath Basin and Range Province, *Jour. Geophys. Res.*, *98*, 22,109–22,122, 1993.

Zhu, L., and H. Kanamori, Moho depth variation in southern California from teleseismic receiver functions, *Jour. Geophys. Res.*, *105*, 2969–2980, 2000.